

Nuclear Magnetic Resonance
—
Advanced Concepts and Applications
to Quantum Materials

Der Fakultät für Physik und Geowissenschaften
der Universität Leipzig

eingereichte

DISSERTATION

zur Erlangung des akademischen Grades

Doktor rerum naturalium

Dr. rer. nat.

vorgelegt

von Dipl.-Phys. Jonas Kohlrautz
geboren am 29.12.1985 in Göttingen

Gutachter: Prof. Dr. Jürgen Haase
Prof. Dr. Geert Rikken

Tag der Verleihung 22. Mai 2017

Bibliographische Beschreibung

Kohlrautz, Jonas

Nuclear Magnetic Resonance – Advanced Concepts and Applications
to Quantum Materials

Universität Leipzig, Dissertation

131 S.*, 134 Lit.*, 64 Abb., 5 Anlagen

Referat

Diese Arbeit behandelt verschiedene Themen im Bereich der kernmagnetischen Resonanz (NMR) an Festkörpern. Der umfangreichste Themenkomplex sind hierbei Untersuchungen in gepulsten Magnetfeldern. Diese ermöglichen Experimente bei Feldstärken, die sich auf keine andere Weise nicht-destruktiv erreichen lassen, bedeuten aber Schwierigkeiten für NMR Experimente aufgrund ihrer inherenten Zeitabhängigkeit.

Es wird eine angepasste Datenanalyse vorgestellt, die Korrekturen für Intensitätsverfälschungen enthält und die Zeitabhängigkeit des Magnetfeldes bei der Berechnung einer Fouriertransformation mit zeitabhängigen Basisfunktionen berücksichtigt. Hiermit werden Testmessungen an elementaren Metallen durchgeführt um die Knight-Verschiebung K_S und die Kern-Gitter-Relaxationszeit T_1 zu messen. Anschließende Messungen an $\text{SrCu}_2(\text{BO}_3)_2$ zeigen desweiteren eindrucksvoll die Detektion einer feld- und temperaturabhängigen Überstruktur der Elektronenspins.

In einem weiteren Themenbereich werden Ergebnisse von Untersuchungen an dem Hochtemperatursupraleitersystem $\text{HgBa}_2\text{CuO}_{4+\delta}$ präsentiert. Bei der Auswertung von temperatur- und orientierungsabhängigen NMR-Verschiebungsmessungen wird ein Widerspruch zu dem im Allgemeinen angenommenen Model mit einer einzigen Spin-Flüssigkeit gefunden. Stattdessen wird eine Analyse mit drei verschiedenen additiven Komponenten entwickelt. Bei der Anwendung dieser Zerlegung wird eine universelle Pseudolückenkomponente gefunden, eine Fermiflüssigkeitskomponente, die nur bei höheren Dotierungsstufen existiert, und eine dritte, die ihr Vorzeichen in Abhängigkeit von der Dotierung ändert. In einem letzten kürzeren Thema werden vorläufige Ergebnisse von Untersuchungen zu der Dynamik von großen, dipolar gekoppelten, Kernspinsystemen behandelt. Hierbei soll eine Vorhersage über die Existenz von zusätzlichen, nicht magnetisierungserhaltenden, Resonanzen überprüft werden.

* ... S. (Seitenzahl insgesamt)

... Lit. (Anzahl der im Literaturverzeichnis ausgewiesenen Literaturangaben)

Contents

1	Introduction	1
2	Concepts of NMR	5
2.1	Nuclear magnetism	5
2.2	Quadrupolar splitting	7
2.3	Dipolar coupling	9
2.4	Hyperfine coupling	10
2.5	Adiabatic inversion in a time-dependent magnetic field	11
2.6	NMR electronics	12
2.6.1	NMR spectrometer	12
2.6.2	Resonance circuits	13
3	NMR at the highest magnetic fields	15
3.1	Pulsed magnetic fields	15
3.2	State of the art of NMR in pulsed magnetic fields	17
4	A new approach: field and intensity corrected spectra in pulsed magnetic fields	21
4.1	Nuclear spins in a changing magnetic field	22
4.1.1	Field-dependent contributions	23
4.1.2	Field-independent contributions	23
4.1.3	Larmor precession	24
4.2	Spectral artifacts	25
4.3	Frequency-dependent intensity modifications	27
4.3.1	Off-resonance excitation	27
4.3.2	Off-resonance detection	31
4.4	Field determination	32

4.5	Fourier transform with time-dependent base functions	34
	Aliasing	36
	Excitation bandwidth and reconstruction of broad spectra	36
	Assembling broad spectra	37
	Linear phase correction	38
4.6	Longitudinal magnetization (T_1)	39
5	Shift and spin-lattice relaxation measurements in pulsed magnetic fields	41
5.1	Shift measurement	41
	5.1.1 Experimental	41
	5.1.2 Results	42
	Field fit	43
	Fourier transform with time-dependent base functions	44
5.2	Measurement of nuclear spin-lattice relaxation	47
	5.2.1 Experimental	47
	5.2.2 Results aluminum	49
	5.2.3 Results gallium	51
6	Pulsed field NMR of strontium copper borate	53
6.1	$\text{SrCu}_2(\text{BO}_3)_2$	53
6.2	Prior high field NMR	58
6.3	Experimental	59
6.4	Results	60
	6.4.1 High-temperature paramagnetic phase (119 K)	61
	6.4.2 Low-temperature paramagnetic phase with a superstructure (2 K)	63
	6.4.3 Comparison with DC field measurements	68
	6.4.4 Spectra at 46 T and 42 T	69
7	Electronic spin susceptibilities in cuprates	73
7.1	High-temperature superconductivity in the cuprates	73
7.2	$\text{HgBa}_2\text{CuO}_{4+\delta}$	74
7.3	NMR of cuprates and electronic spin susceptibility	75
7.4	Experimental	78
7.5	Results and discussion	78
	7.5.1 Temperature-dependent shifts	79
	7.5.2 Decomposition into shift components	82

7.6 Summary	89
8 Conclusion	91
Bibliography	93
A Dynamics of interacting spin systems	107
A.1 Non-secular resonances in dipolar coupled spin systems	107
A.2 Experimental	110
A.3 Results and discussion	112
A.4 Conclusion	114
B Simulation of an adiabatic inversion in the rotating frame	115
C Radio frequency circuits	119
C.1 Experimental	119
C.2 Results and discussions	119
D Modification of pulse field spectrometer for T_1 measurements	121
E Source code for pulsed field analysis	125

CHAPTER 1

Introduction

Over the last half-century, nuclear magnetic resonance (NMR) has become an indispensable probe in a number of different fields, e.g., chemistry, physics, and medicine [9, 10, 16, 49, 64, 66, 90]. While NMR is often used for imaging or structure determination, hyperfine interactions [115] offer a unique local insight into the electronic properties of quantum materials [38, 51, 128].

In this thesis, multiple topics will be addressed. These include the development of novel experimental NMR techniques and data analysis, as well as their application for condensed matter research. First and foremost, the capabilities of NMR at the highest magnetic fields, i.e., in pulsed high-field magnets [55], were further advanced. A field-driven phase transition in a magnetic material was observed in a first application [56]. The second topic concerns the understanding of new NMR data of cuprate high-temperature superconductors. Here, proof for the failure of the prevalent single-fluid description of those materials was established [95]. The shorter third part deals with experiments aimed at the understanding of the dynamics of large interacting (nuclear) spin systems [60].

While only pulsed high-field magnets offer access to the highest magnetic fields available, performing NMR measurements becomes challenging. In the early days of NMR research, resistive magnets based on conventional metallic conductors were used. A steady increase of the available fields set in with advances in superconducting materials that made highly stable, homogeneous magnets with high field strength possible. The resulting gain in sensitivity and resolution was the main driving force for these developments. However, in order to study the field dependence of electronic properties of quantum materials, it is of great interest to have even higher magnetic fields available. Here, depending on the

system under investigation, fields on the order of 100 T are needed to induce changes in the electronic structure [39, 105]. Due to the limited critical fields and currents, the superconductivity can break down in superconducting materials. This limits the achievable field strength to about 25 T currently. To go beyond, one again has to resort to conventional conducting materials, where resistive heating and mechanical stability introduce new limits. While continuous magnetic fields of about 45 T have been created with hybrid magnets (superconducting and resistive), only pulsed magnets are capable of delivering the highest fields possible. Using only the heat capacity of the conducting material to absorb the thermal energy dissipated during the pulse, non-destructive fields of up to 100 T come into reach, but only for fractions of a second [81]. This transient nature of the magnetic field complicates NMR measurements tremendously: Firstly, the normally omnipresent signal averaging cannot be used anymore with the changing field that is only present during short periods of time. Secondly, a careful manipulation of spin systems with sophisticated pulse sequences becomes next to impossible due to off-resonance effects and limited reproducibility of the field.

Despite the challenges, first NMR signals in a pulsed high magnetic field were observed in 2003 by Haase et al. (Dresden, Germany) [31] and similar endeavors were started elsewhere [1, 134]. Later, the modulation of NMR signals due to the time dependence of the magnetic field was discussed carefully and a time-domain demodulation technique for a single-component signal was demonstrated by Meier et al. [72].

A new approach to NMR spectroscopy in pulsed magnetic fields will be presented in Chapter 4. The Fourier transform is modified to incorporate the time dependence of the magnetic field using time-dependent base functions. With this, demodulated and signal averaged spectra with multiple NMR signals can be obtained together with intensity corrections that take off-resonance effects into account. A detailed and technical discussion aimed at an interested reader introduces possible solutions using time and frequency domain signal processing. Based on field-stepped free induction decays a road map to obtain broad spectra in pulsed magnetic fields is given.

As a proof of concept, this approach is applied to measurements of a NMR Knight shift, as well as to the longitudinal relaxation time T_1 (Chapter 5). In these experiments at the *Dresden High Magnetic Field Laboratory*, signal averaging for a weak signal over multiple field pulses is shown and an adiabatic inversion using a weak radio frequency field is employed for the T_1 experiments.

Finally, the spin-dimer antiferromagnet $\text{SrCu}_2(\text{BO}_3)_2$ is investigated using ^{11}B NMR (Chapter 6). These experiments showcase that the inherent time dependence of the

magnetic field can even be beneficial. The field-stepped measurements sample different regions of a broad frequency spectrum at different times during the pulse. As a function of field and temperature, very different spectra are found, consistent with a change of the ground state of the material resulting in the presence of a magnetic superlattice at high fields and low temperatures [51]. This marks the first compelling observation of field-induced electronic phenomena using pulsed field NMR.

Cuprate high-temperature superconductors remain an unsolved topic of modern solid state physics despite being discovered more than 25 years ago. The nature of the pseudogap [118], the presence of stripe or charge order [128], and the existence of a quantum critical point [21, 122] are examples for topics still under debate. Results on the cuprate superconductor $\text{HgBa}_2\text{CuO}_{4+\delta}$ from conventional static field NMR carried out in Leipzig are shown in Chapter 7. By analyzing the temperature-dependent shifts of four samples with different doping levels, a discrepancy with predictions from the prevalent single-fluid model is found. This forces an interpretation of the shifts in terms of multiple distinct components. A decomposition procedure is presented and used to separate three distinct contributions. One of them is present in all samples and appears to be related to the pseudogap. Upon doping, the shifts develop a characteristic drop below the critical temperature for superconductivity, marking the emergence of a Fermi liquid-like contribution. While these two components had previously been detected in $\text{La}_{2-x}\text{Sr}_x\text{CuO}_4$ and $\text{YBa}_2\text{Cu}_4\text{O}_8$ [33, 34, 73, 85], an additional third one with a different ratio of hyperfine coefficients for the studied sample orientations is found in $\text{HgBa}_2\text{CuO}_{4+\delta}$.

The dynamics of large interacting spin systems are important for the understanding of many quantum materials. Solid state NMR can be used to test theories on model systems with more than six orders of magnitude difference in time scales of internal interactions compared to thermal coupling to the environment. In continuation of my diploma thesis [53, 70], Appendix A discusses experiments concerning a nuclear spin system in the presence of a strong radio frequency field. Under such conditions, the existence of non-secular resonances was predicted [59].

Publications

- Jurkutat, M., Kohlrautz, J., Reichardt, S., Erb, A., Williams, G. V. M., and Haase, J. ‘NMR of Cuprates - Recent Developments’. In: *High T_c copper oxide superconductors and related materials*. Ed. by Bussmann-Holder, A., Keller, H., and Bianconi, A. Springer Verlag, forthcoming 2017.
- Kohlrautz, J., Reichardt, S., Green, E. L., Kühne, H., Wosnitza, J., and Haase, J. ‘NMR shift and relaxation measurements in pulsed high-field magnets up to 58 T’. In: *J. Magn. Reson.* 263 (2016), p. 1. DOI: 10.1016/j.jmr.2015.12.009.
- Kohlrautz, J., Haase, J., Green, E., Zhang, Z., Wosnitza, J., Herrmannsdörfer, T., Dabkowska, H., Gaulin, B., Stern, R., and Kühne, H. ‘Field-stepped broadband NMR in pulsed magnets and application to $\text{SrCu}_2(\text{BO}_3)_2$ at 54 T’. In: *J. Magn. Reson.* 271 (2016), p. 52. DOI: 10.1016/j.jmr.2016.08.005.
- Kropf, C. M., Kohlrautz, J., Haase, J., and Fine, B. V. ‘Anomalous longitudinal relaxation of nuclear spins in CaF_2 ’. In: *Fortschr. Phys.* (2016). DOI: 10.1002/prop.201600023.
- Meier, B., Kohlrautz, J., and Haase, J. ‘Eigenmodes in the Long-Time Behavior of a Coupled Spin System Measured with Nuclear Magnetic Resonance’. In: *Phys. Rev. Lett.* 108 (2012), p. 1. DOI: 10.1103/PhysRevLett.108.177602.
- Meier, B., Kohlrautz, J., Haase, J., Braun, M., Wolff-Fabris, F., Kampert, E., Herrmannsdörfer, T., and Wosnitza, J. ‘Nuclear magnetic resonance apparatus for pulsed high magnetic fields’. In: *Rev. Sci. Instrum.* 83 (2012), p. 083113. DOI: 10.1063/1.4746988.
- Rybicki, D., Kohlrautz, J., Haase, J., Greven, M., Zhao, X., Chan, M. K., Dorow, C. J., and Veit, M. J. ‘Electronic spin susceptibilities and superconductivity in $\text{HgBa}_2\text{CuO}_{4+\delta}$ from nuclear magnetic resonance’. In: *Phys. Rev. B* 92 (2015), p. 081115. DOI: 10.1103/PhysRevB.92.081115.

CHAPTER 2

Concepts of NMR

Applications of Nuclear magnetic resonance (NMR) can be found in many fields, e.g., chemistry, medicine, and physics, each with specialized methods and associated theory. In this chapter, some NMR topics of interest for this thesis will be discussed. We will start with the quantum mechanical description of a nuclear spin including quadrupolar coupling and continue with a brief overview on NMR spectrometers. The content is mostly based on Refs. [2, 27, 64, 101].

2.1 Nuclear magnetism

We consider the quantum mechanical description of a NMR experiment in a magnetic field. Only nuclear spins with $I \geq 1/2$ can be used to study the respective magnetic environment. In addition, nuclei with $I \geq 1$ can provide insight into the electric environment through electric quadrupole interactions.

In a static, high magnetic field \mathbf{B}_0 along the z -direction, the Hamiltonian \mathcal{H} of the spin can be subdivided into the Zeeman term $\mathcal{H}_{\text{Zeeman}}$ and the remainder \mathcal{H}' . We write,

$$\mathcal{H} = \mathcal{H}_{\text{Zeeman}} + \mathcal{H}', \quad (2.1)$$

$$\mathcal{H}_{\text{Zeeman}} = -\hbar\gamma\mathbf{B}_0 \cdot \hat{\mathbf{I}} = -\hbar\gamma B_0 \hat{I}_z = \hbar\omega_{\text{Larmor}} \hat{I}_z. \quad (2.2)$$

Here, $\hat{\mathbf{I}}$ and \hat{I}_z are the spin operator and the respective z -component. In case of a sufficiently high magnetic field, the Zeeman term dominates, and \mathcal{H}' can be treated as a perturbation.

The spin eigenstates $|Im\rangle$ are given in terms of spin quantum numbers I and m ,

$$\hat{\mathbf{I}}^2 |Im\rangle = I(I+1) |Im\rangle, \quad (2.3)$$

$$\hat{\mathbf{I}}_z |Im\rangle = m |Im\rangle. \quad (2.4)$$

Here, $-I, -I+1, \dots, I$ are the allowed values for m . In the absence of other interactions, the Zeeman energy levels E_m are

$$E_m = -\hbar\gamma B_0 m. \quad (2.5)$$

While the energy levels are non-degenerate, the experimentally detectable energy difference ΔE between two adjacent levels is constant with $\Delta E = \hbar\gamma B_0$, see Fig. 2.1. This energy splitting of a few mK, however, is very small compared to the thermal energy at typical temperatures.

In thermal equilibrium at temperature T , the population probability p_m follows a Boltzmann distribution. The ratio of population probabilities of two adjacent levels is therefore given by

$$\frac{p_{m+1}}{p_m} = \exp\left(\frac{\Delta E}{k_B T}\right) = \exp\left(\frac{\hbar\gamma B_0}{k_B T}\right). \quad (2.6)$$

Even at a temperature of $T = 4.2$ K and a magnetic field of $B_0 = 60$ T, the difference of both population probabilities for ^1H nuclei is less than 3 %.

Albeit small, this distribution of p_m gives rise to a macroscopic sample magnetization M_z that can either be parallel or anti-parallel to the applied magnetic field, depending on the sign of γ . Since the energy differences ΔE are very small compared to the thermal energy

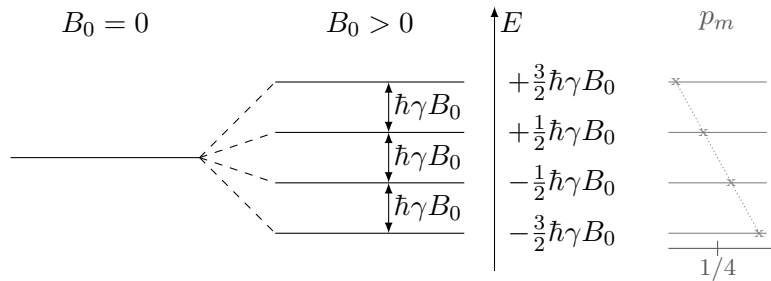


Figure 2.1: Energy levels for a spin $I = 3/2$ without magnetic field ($B_0 = 0$) and with a magnetic field ($B_0 > 0$) and the associated population probabilities p_m in absence of a quadrupolar splitting.

$k_B T$, the so-called high-temperature approximation is valid and yields the Curie formula. With N/V as the density of spins, the result is proportional to the applied magnetic field and inversely proportional to the temperature,

$$M_z = \frac{N}{V} \frac{\hbar^2 \gamma^2 B_0 I (I + 1)}{3 k_B T}. \quad (2.7)$$

Therefore, for a fixed volume, M_z is proportional to the number of spins, the magnetic field B_0 and the inverse temperature $1/T$.

2.2 Quadrupolar splitting

Nuclei with a spin $I \geq 1$ have an electric quadrupolar moment eQ in addition to the magnetic dipolar moment, however the following discussion will be focussed on half-integer spins due to the relevance for the presented topics. This electric quadrupolar moment interacts with the electric field gradient (EFG) eq present at the position of the nucleus. The corresponding Hamiltonian \mathcal{H}_Q in terms of spin operators is given by

$$\mathcal{H}_Q = \frac{e^2 q Q}{4I(2I-1)} \left[3\hat{I}_Z^2 - I(I+1) + \frac{1}{2}\eta (\hat{I}_+^2 + \hat{I}_-^2) \right], \quad (2.8)$$

with $\eta = (V_{XX} - V_{YY})/V_{ZZ}$ and $eQ = V_{ZZ}$. Here, V is a traceless tensor describing the EFG in its principle axis system (PAS) X, Y, Z with $|V_{ZZ}| \geq |V_{YY}| \geq |V_{XX}|$. The ladder operators are given by

$$\hat{I}_\pm = \hat{I}_X \pm i\hat{I}_Y. \quad (2.9)$$

In a large magnetic field, this Hamiltonian \mathcal{H}_Q can be treated as a perturbation to the Zeeman Hamiltonian and the quadrupole frequency ω_Q is introduced as

$$\omega_Q = \frac{3e^2 q Q}{2I(2I-1)\hbar}. \quad (2.10)$$

With the angles α and β describing the rotation from the laboratory coordinate system to the PAS, the orientation-dependent quadrupole frequency ω'_Q is given by

$$\omega'_Q = \omega_Q \left[\frac{3 \cos^2 \beta - 1}{2} + \frac{\eta}{2} \sin^2 \beta \cos 2\alpha \right] \quad (2.11)$$

and the transition $m - 1 \leftrightarrow m$ is shifted in first order by

$$\Delta\omega_{m-1 \leftrightarrow m}^{(1)} = \left(m - \frac{1}{2}\right) \omega'_Q \quad (2.12)$$

$$= \left(m - \frac{1}{2}\right) \frac{3e^2qQ}{2I(2I-1)\hbar} \left[\frac{3\cos^2\beta - 1}{2} + \frac{\eta}{2} \sin^2\beta \cos 2\alpha \right]. \quad (2.13)$$

Therefore, the central transition (CT) $-1/2 \leftrightarrow 1/2$ is not affected since the m -dependent prefactor vanishes. The others, so-called satellite transitions (ST), however become shifted.

In the case of a significant quadrupolar splitting, the second order correction also has to be taken into account. The CT $-1/2 \leftrightarrow 1/2$ of a half-integer spin is then shifted by

$$\Delta\omega_{-1/2 \leftrightarrow 1/2}^{(2)} = -\frac{\omega_Q^2}{6\omega_L} \left[I(I+1) - \frac{3}{4} \right] \cdot \left[A(\alpha, \eta) \cos^4\beta + B(\alpha, \eta) \cos^2\beta + C(\alpha, \eta) \right], \quad (2.14)$$

with the angular-dependent terms

$$A(\alpha, \eta) = -\frac{27}{8} - \frac{9}{4}\eta \cos 2\alpha - \frac{3}{8}\eta^2 \cos^2 2\alpha, \quad (2.15)$$

$$B(\alpha, \eta) = \frac{15}{4} - \frac{1}{2}\eta^2 + 2\eta \cos 2\alpha + \frac{3}{4}\eta^2 \cos^2 2\alpha, \quad (2.16)$$

$$C(\alpha, \eta) = -\frac{3}{8} + \frac{1}{3}\eta^2 + \frac{1}{4}\eta \cos 2\alpha - \frac{3}{8}\eta^2 \cos^2 2\alpha. \quad (2.17)$$

Fig. 2.2 shows the resulting energy diagram as well as the associated spectra for a small anisotropy η . In this case, the second order effects of the STs can be neglected, otherwise the STs are shifted as well [125].

In the case of a distribution of the EFGs, e.g., from material inhomogeneities, a broadening of the satellites is to be expected since different spins in the materials at quasi-identical sites will see different EFGs and thus different quadrupole frequencies.

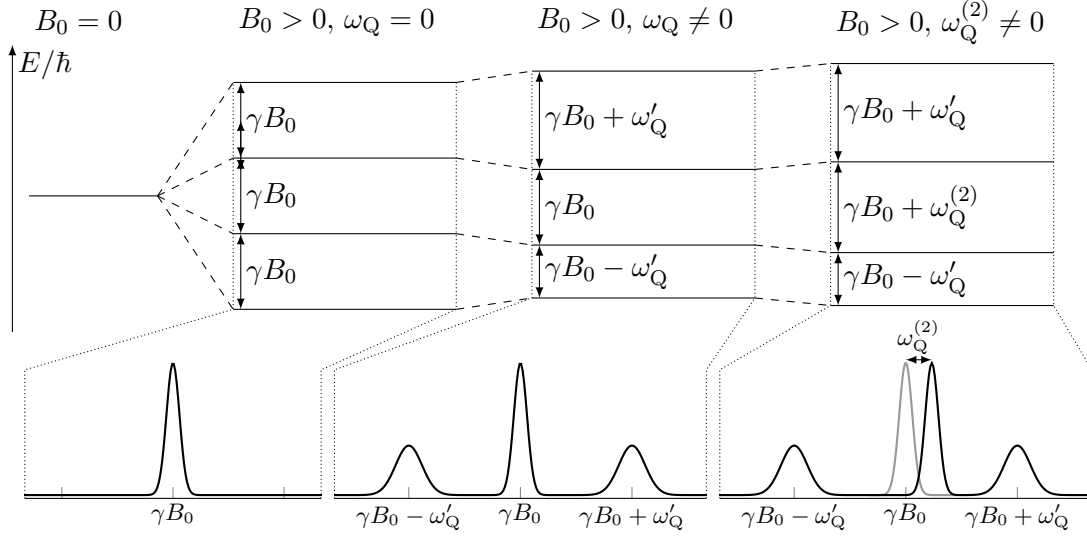


Figure 2.2: Zeeman energy levels for a spin $I = 3/2$ in presence of a quadrupolar interaction and the associated spectra in case of vanishing anisotropy η with $\omega_Q^{(2)} = \Delta\omega_{-1/2 \leftrightarrow 1/2}^{(2)}$.

2.3 Dipolar coupling

The coupling of the dipolar moments of different spins j and k is described by the Hamiltonian \mathcal{H}_{DD} that sums over all pairs of spins in the material. It is given by

$$\mathcal{H}_{\text{DD}} = \sum_{j,k} \frac{\hbar^2 \gamma_j \gamma_k}{2} \left[\frac{\hat{\mathbf{I}}_j \cdot \hat{\mathbf{I}}_k}{r_{jk}^3} + 3 \frac{(\hat{\mathbf{I}}_j \cdot \mathbf{r}_{jk})(\hat{\mathbf{I}}_k \cdot \mathbf{r}_{jk})}{r_{jk}^5} \right]. \quad (2.18)$$

Here, \mathbf{r}_{jk} is the vector connecting both spins. Using θ_{jk} for the angle inbetween the \mathbf{r}_{jk} and the z axis of the spin operators \hat{I}_{jz} and \hat{I}_{kz} , this expression can be rewritten into a sum of six different terms, each with a characteristic combination of spin operators,

$$\mathcal{H}_{\text{DD}} = \sum_{j,k} \frac{\hbar^2 \gamma_j \gamma_k}{2r_{jk}^3} [A_{jk} + B_{jk} + C_{jk} + D_{jk} + E_{jk} + F_{jk}], \quad (2.19)$$

$$A_{jk} = \hat{I}_{jz} \hat{I}_{kz} (1 - 3 \cos^2 \theta_{jk}), \quad (2.20)$$

$$B_{jk} = -\frac{1}{4} [\hat{I}_j^+ \hat{I}_k^- + \hat{I}_j^- \hat{I}_k^+] (1 - 3 \cos^2 \theta_{jk}), \quad (2.21)$$

$$C_{jk} = -\frac{3}{2} \left[\hat{I}_j^+ \hat{I}_{kz} + \hat{I}_{jz} \hat{I}_k^+ \right] \sin \theta_{jk} \cos \theta_{jk} e^{-i\phi_{jk}}, \quad (2.22)$$

$$D_{jk} = -\frac{3}{2} \left[\hat{I}_j^- \hat{I}_{kz} + \hat{I}_{jz} \hat{I}_k^- \right] \sin \theta_{jk} \cos \theta_{jk} e^{-i\phi_{jk}}, \quad (2.23)$$

$$E_{jk} = -\frac{3}{4} \hat{I}_j^+ \hat{I}_k^+ \sin^2 \theta_{jk} e^{-2i\phi_{jk}}, \quad (2.24)$$

$$F_{jk} = -\frac{3}{4} \hat{I}_j^- \hat{I}_k^- \sin^2 \theta_{jk} e^{2i\phi_{jk}}. \quad (2.25)$$

Within the secular approximation, only those terms that conserve the total Zeeman energy are of relevance. This is clearly the case for A since the involved operators do not change the state of the spins. For B , however, this is only valid for a common type of spin, i.e., $\gamma_j = \gamma_k$. All other contributions lead to a change in the Zeeman energy and therefore are not part of the truncated dipolar Hamiltonian.

For nuclear spins in a strong magnetic field, the energies of the dipolar coupling are orders of magnitude smaller compared with the Zeeman term as well as the thermal energy $k_B T$. As a consequence, no shift arises, and only a broadening occurs depending on the gyromagnetic ratios of all constituents and crystal structure. Furthermore, a fine structure of the resonance line can emerge [88]. In liquids, however, this interaction is often averaged out by the molecular motion.

2.4 Hyperfine coupling

In a conducting material, the spin of the conduction electrons gives rise to the Knight shift K_{Knight} [115]. It originates for example from the Fermi contact interaction that is described by

$$\mathcal{H}_{\text{Fermi}} = -\gamma\gamma_e\hbar^2 \hat{I} \cdot \hat{S} \delta(r_e - R_n). \quad (2.26)$$

Here, γ and γ_e are the gyromagnetic ratios of the nucleus and the electron, \hat{I} and \hat{S} the spin operators, and $\delta(r_e - R_n)$ a Dirac delta function describing the spatial overlap.

Considering all electrons in the material, this gives rise to an additional local field that is felt by the nucleus. This can be expressed within the momentum space with the electron wave vector \mathbf{k} , the eigenvalue $m_{\mathbf{k}}$ of the electron spin operator $\hat{S}_{\mathbf{k}z}$, the periodic part of the Bloch wave function $u_{\mathbf{k}}(0)$ at the nucleus, and the Fermi function f as

$$\Delta B_{0e} = \frac{8\pi}{3} \gamma_e \hbar \sum_{\mathbf{k}, m} |u_{\mathbf{k}}(0)|^2 m_{\mathbf{k}} f(E_{\mathbf{k}} - m_{\mathbf{k}} \gamma_e \hbar B_0). \quad (2.27)$$

Evaluating this expression, one finds it to be proportional to the applied magnetic field B_0 , such that it produces a shift of

$$K_{\text{Knight}} = \frac{\Delta B_{0e}}{B} = \frac{8\pi}{3} \gamma_e^2 \hbar^2 \sum_{m_{\mathbf{k}}} \int m_{\mathbf{k}}^2 |u_{\mathbf{k}}(0)|^2 \rho(E_{\mathbf{k}}) \frac{\partial f(E_{\mathbf{k}})}{\partial E_{\mathbf{k}}} dE_{\mathbf{k}} \quad (2.28)$$

$$= \frac{8\pi}{3} \gamma_e^2 \hbar^2 \left\langle |u_{\mathbf{k}}(0)|^2 \right\rangle_{E_F} \frac{\rho(E_F)}{2} \quad (2.29)$$

$$= \frac{\Delta B_{0e}}{B} = \frac{8\pi}{3} \left\langle |u_{\mathbf{k}}(0)|^2 \right\rangle_{E_F} \chi_S \quad (2.30)$$

that is proportional to the electron-spin susceptibility χ_S of the conduction electrons and the average over $|u_{\mathbf{k}}(0)|^2$ at the Fermi surface.

Therefore, NMR can be used to investigate the temperature-dependence of χ_S as long as no other temperature-dependent contributions exist or can be subtracted (e.g., field shielding due to a partial Meissner effect). In case of multiple conduction bands however, this expression might need to be replaced by a sum with independent prefactors $\left\langle |u_{\mathbf{k}}(0)|^2 \right\rangle_{E_F}$, cf. Ref. [13].

2.5 Adiabatic inversion in a time-dependent magnetic field

The concept of using a weak RF field with a frequency ω_{RF} that starts away from the resonance condition (with a Larmor frequency ω_L) and then crosses it using a time-dependent external magnetic field $B_0(t)$ was already well-known in the early days of NMR [2, 10]. The usefulness of such sweeps in pulsed Fourier transform NMR was rediscovered more recently [7, 29, 62], now, utilizing modulated RF fields and leaving the strong external magnetic field B_0 constant, as a broadband alternative to hard RF pulses. Detailed discussions on the subject as well as validating measurements can be found in literature, e.g., Refs. [7, 29], and only a brief description will be given here.

Convenient for a pulsed field experiment, a sweep that starts with $\omega_L < \omega_{\text{RF}}$, crosses $\omega_L = \omega_{\text{RF}}$, and ends at $\omega_L < \omega_{\text{RF}}$, can invert the population densities of a spin system as a replacement for a π pulse. The degree of inversion depends on the amplitude B_{RF} of the RF field, as well as the time-derivative of $B_0(t)$ (and thus ω_L). In general, a faster change of $B_0(t)$ also requires a larger B_{RF} to fulfill the condition for adiabaticity given by

$$\frac{d}{dt} B_0(t) \ll \gamma B_{\text{RF}}^2. \quad (2.31)$$

The difference of $\omega_L = \gamma B_0(t)$ and ω_{RF} at the end of the sweep is limited by the time that is available for the inversion process (e.g., it has to be small compared with T_1). And, depending on this difference, a larger B_{RF} can decrease the degree of inversion in case of a rectangular pulse shape [62]. Note that by modulating the amplitude of the RF field, this effect can be canceled. While the finite quality factor of the RF resonator modifies the actual shape of the RF field (smoothing at the beginning and end), the involved time constant is typically less than 100 ns and can thus be neglected.

A simple numeric density matrix simulation of the inversion process with similar conditions to the pulsed field experiments from Sect. 5.2 (shape limited to a rectangular pulse), can be found in App. B.

2.6 NMR electronics

Most NMR experiments are performed in magnetic fields of several T giving Larmor frequencies in the radio frequency regime. To excite and detect these signals, appropriate spectrometers and probe heads are needed.

2.6.1 NMR spectrometer

In the early days of NMR, measurements were usually done with *continuous wave* (CW) setups. Here, the system under investigation is put in a resonator and irradiated with a weak RF field while modulating the quasi-static external B_0 field. Absorption then leads to a detuning of the resonator in the case that a resonance is detected. First pulsed NMR experiments were performed by E. Hahn in 1949 [37], but only became popular in the 1970s [25] and are used almost exclusively today. Here, strong RF excitation pulses are applied for short time spans, and signals are only detected afterward (however this is not always the case in certain special applications, e.g., certain decoupling schemes).

From an electronics point of view, a pulsed NMR spectrometer is a high power RF transmitter for the excitation combined with an RF receiver, cf. Fig. 2.3. For signal averaging, these two components need to have a coherent phase [104]. This can be accomplished by using a single frequency source for both of them or by using phase-locked loops.

Modern spectrometers often employ *IQ*-modulation techniques to produce pulses with arbitrary phase evolution and shape. Here, the output of a two-channel digital-to-analog converter (DAC) is mixed with the output of a local oscillator, once in-phase and once shifted by $\pi/2$, see Fig. 2.3. The sum of these two signals can then be within the frequency range from $\omega - \omega_{\text{out}}/2$ to $\omega + \omega_{\text{out}}/2$ with ω being the frequency of the oscillator and

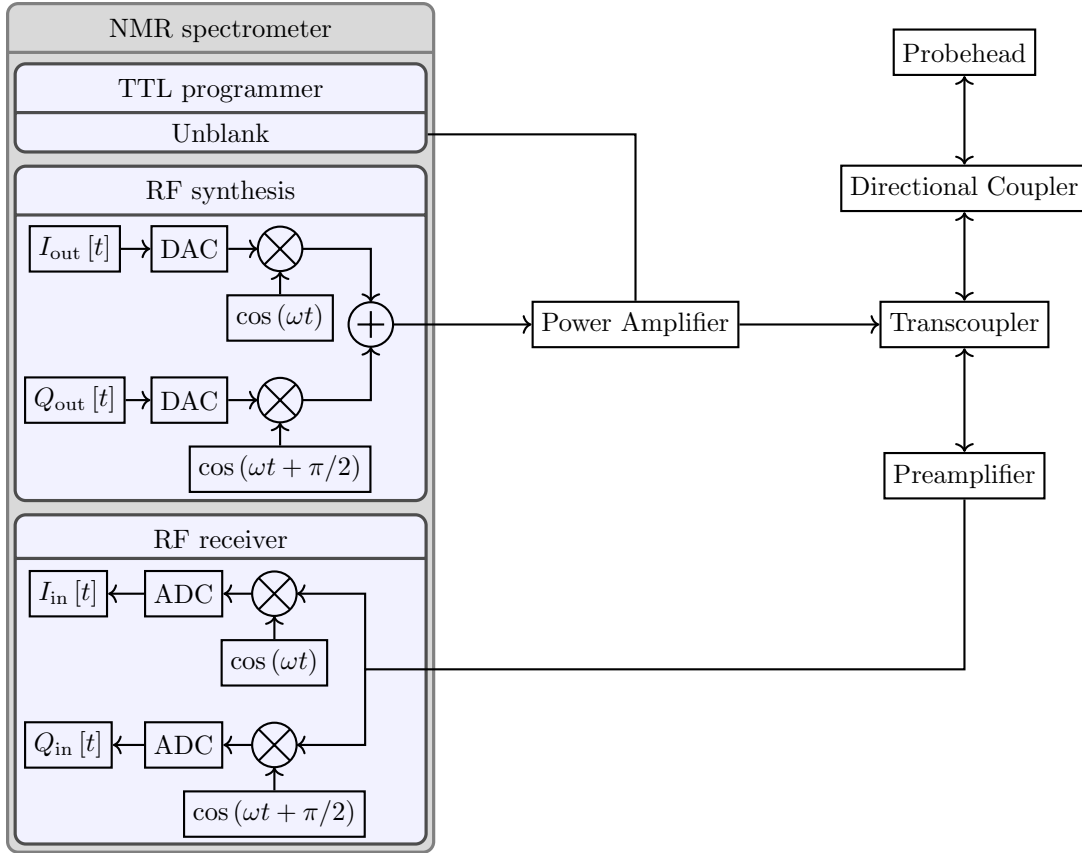


Figure 2.3: Schematic NMR spectrometer. Neccessary frequency filters to remove unwanted mixer products are not shown.

$\omega_{\text{out}}/2\pi$ the sampling rate of the DAC.

A similar approach is then used in the receiver in an *IQ*-demodulation scheme. Often, the signals are left at an intermediate frequency in the analog stage of the receiver and only fully demodulated to the baseband in later digital processing.

2.6.2 Resonance circuits

Radio frequency resonance circuits (also called tank circuits) are used in most NMR experiments. Around their resonance frequency, they increase the RF field during the excitation of the spin system and amplify the signal from the induced voltage during detection. Depending on the experimental conditions and necessities, e.g., available space, stability, number of resonance frequencies, temperature, and frequency range, different circuits can be employed [76], see for example Fig. 2.4.

The behavior of such resonators can be described in good approximation using a driven

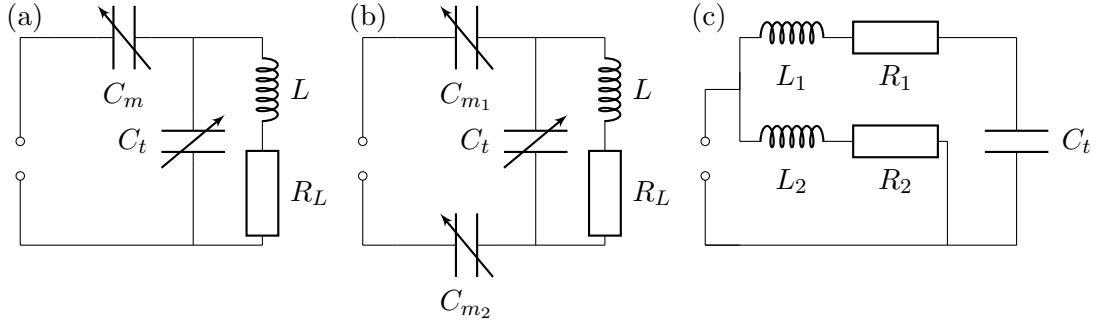


Figure 2.4: Equivalent circuits of different RF resonators for single frequency NMR excitation and detection. (a) and (b) are capacitively coupled tank circuits that can be matched to 50Ω at different frequencies, (c) is a *tapped coil* resonator.

harmonic oscillator with losses that originate primarily from the coil wire. For the excitation of a spin system, only the circular polarized component B_1 of the RF field is relevant. It depends on the applied RF power level P , the resonance frequency ω_0 (equal to the RF carrier frequency), the quality factor Q (given by the ratio of the inductivity and resistivity as well as the resonance frequency), and the coil volume V . With the vacuum susceptibility μ_0 , it can be estimated as

$$B_1 = \sqrt{\frac{\mu_0 Q P}{2\omega_0 V}}. \quad (2.32)$$

During detection, the signal intensity $g(\omega)$ and phase $\alpha(\omega)$ depend on the frequency and the quality factor according to

$$g(\omega) = \frac{\omega_0}{\omega} \frac{1}{\sqrt{Q^2 \varepsilon^2 + 1}}, \quad (2.33)$$

$$\Delta\alpha(\omega) = \arctan\left(\frac{1}{Q\varepsilon}\right). \quad (2.34)$$

Note that Q is the quality factor of the loaded tank circuit ($Q_{\text{loaded}} = Q_{\text{receive}}/2$). An experimental test of the relationship for the intensity is described in App. C.

CHAPTER 3

NMR at the highest magnetic fields

The state of the art of NMR pulsed high-field magnets prior to the works presented in this thesis will be introduced in this chapter starting with a brief summary on pulsed magnetic fields. Then, the previous NMR efforts of the last 15 years are discussed. While these pioneering efforts did not produce much insight into materials science yet, they proved that NMR can indeed be performed in a pulsed magnetic field despite all challenges.

3.1 Pulsed magnetic fields

The most fundamental way to generate a magnetic field is by producing an electric current I in a wire. According to the Biot-Savart law, the resulting field \mathbf{B} is proportional to I . And, in the case of multiple conductor segments, \mathbf{B} is the linear superposition of all their fields. Therefore, to obtain a higher magnetic field, only I has to be increased, or additional segments (producing parallel fields) have to be added. In practice, however, electrical losses, mechanical forces, and space determine the maximum field and the required cooling effort.

While superconducting materials offer a way around electrical losses, they need to be kept at cryogenic temperatures and, most importantly, can only withstand certain magnetic field strengths and currents before superconductivity is suppressed. While certain ceramic high-temperature superconductors promise the potential for higher fields up to about 25 T, the task of producing a usable magnet with them is complicated and mechanical stability becomes problematic [68]. Therefore, to access the highest magnetic fields possible, superconducting materials can not be used and one has to resort to resistive conductors where two different modes of operation are used: DC magnetic fields and pulsed magnetic fields. While the former require large amounts of power (in the order of

up to 30 MW [18, 81, 89]) for quasi-static operation, only the latter give access to fields above 45 T, however only for fractions of a second using high peak power.

The concept of producing a pulsed magnetic field with a high-power energy storage unit (e.g., batteries, capacitors or a flywheel [19, 126, 129, 130]) that is slowly charged in a first step and then discharged across a field coil, cf. Fig. 3.1, was developed almost a century ago [24, 47]. However, facilities that give access to pulsed magnetic fields with field duration suitable for NMR experiments only went into operation some years ago with efforts in USA, Germany, France, Japan, and China. An exhaustive overview of the available fields can be found in Ref. [81].

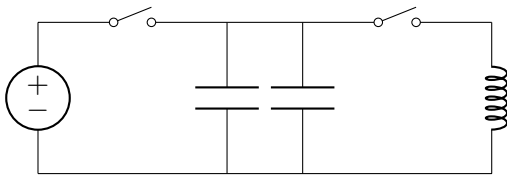


Fig. 3.1: Basic principle of a pulsed magnetic field driven by a capacitor bank.

The first experiments with pulsed magnetic fields in Dresden (Germany) were performed at the *Leibniz-Institut für Festkörper- und Werkstoffforschung* (IFW) in 1999 [61]. This setup served as a test bed for the later built *Dresden High Magnetic Field Laboratory* (HLD).

In both cases, high voltage capacitor modules were chosen as energy storage and the field coils were cooled by a liquid nitrogen bath.

The energy density of the magnetic field produces a pressure on the conducting wires to increase the volume over which the magnetic flux is distributed. As a consequence, the maximum field is ultimately limited by the mechanical strength of the magnet coil. On top of thermal constraints, the available voltages and capacities further limit the field strength and the duration depending on the coil geometry and inductance, forcing a trade-off between the highest field and the time that is available for experiments. As an example, Fig. 3.2 shows the $B(t)$ for two different coils *KS3* and *LP* that were used in the experiments that will be discussed in the following chapters.

- *KS3* is a fast-cooling magnet with fields up to 63 T (designed for fields up to 70 T) and an NMR window of about 4 ms [71] was used for most measurements
- *LP* is a larger long pulse magnet with fields up to 40 T (designed up to 60 T) and an NMR window of about 25 ms [124] was used for the aluminum metal relaxation measurements

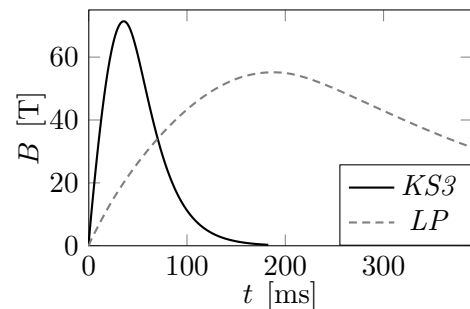


Fig. 3.2: Time-dependence of the magnetic field in the *KS3* and *LP* coil (data reproduced from Ref. [71]).

Common to all currently available pulsed field magnets is the rather low field homogeneity

$\gtrsim 20$ ppm even over small sample sizes in the order of 1 mm^3 [87].

3.2 State of the art of NMR in pulsed magnetic fields

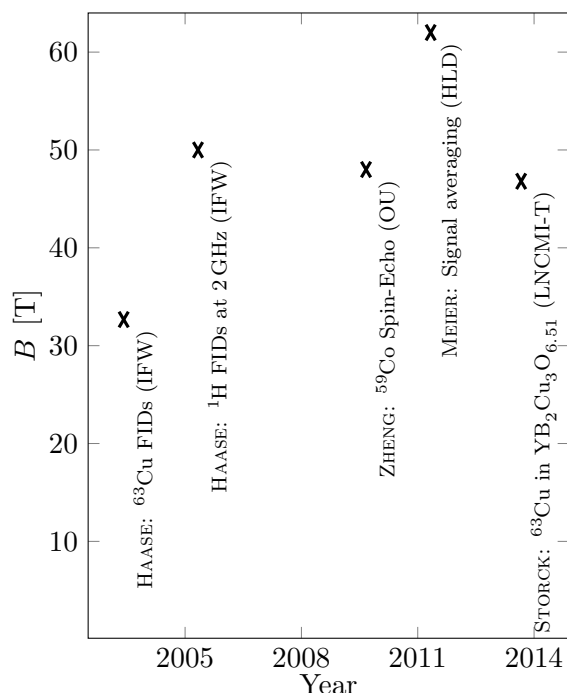


Fig. 3.3: Milestones of NMR in pulsed magnetic fields with reported maximum fields and date of publication as axes.

A little later, efforts at the *KYOKUGEN* (Osaka University, Japan, OU), the *Laboratoire National des Champs Magnétiques Intenses* (Toulouse, France, LNCMI-T), and the *Wuhan High Magnetic Field Center* (Wuhan, China, WHMFC) commenced and reported successful experiments on other nuclei and the first observation of spin-echoes [1, 134].

A typical $B(t)$ is shown in Fig. 3.4a together with the resulting NMR frequencies for metallic aluminum: Around its maximum, the field is described by a parabolic curve, and the observed NMR signals follow the changing field. The obtained field decreases in successive field pulses which has to be taken into account, cf. Fig. 3.4b.

It was evident from the beginning, that the most favorable conditions for NMR are around the maximum of magnetic field B_{max} . Here, the weaker time-dependence gives the most consistent excitation conditions and vanishing forces on the probe head due to induced voltages [87]. In order to stay within the bandwidth of the experiment, B_{max} needs to be produced with high precision.

As shown in Fig. 3.3, NMR in pulsed magnetic fields was pioneered in Dresden at the IFW in 2003 with publications on the first observed FIDs in metallic copper at fields of up to 33 T [31]. This showed that the achievable signal-to-noise ratio is sufficient despite the need to use small sample volumes in order to allow high bandwidth measurements [35]. Later on, higher fields and other nuclei at higher Larmor frequencies were observed, notably ^1H at 2 GHz [32]. With the opening of the HLD, larger magnets with longer lasting fields became available, pushing the time window for NMR experiments to several ms using several MJ of stored energy [126].

A little later, efforts at the *KYOKUGEN* (Osaka University, Japan, OU), the *Lab-*

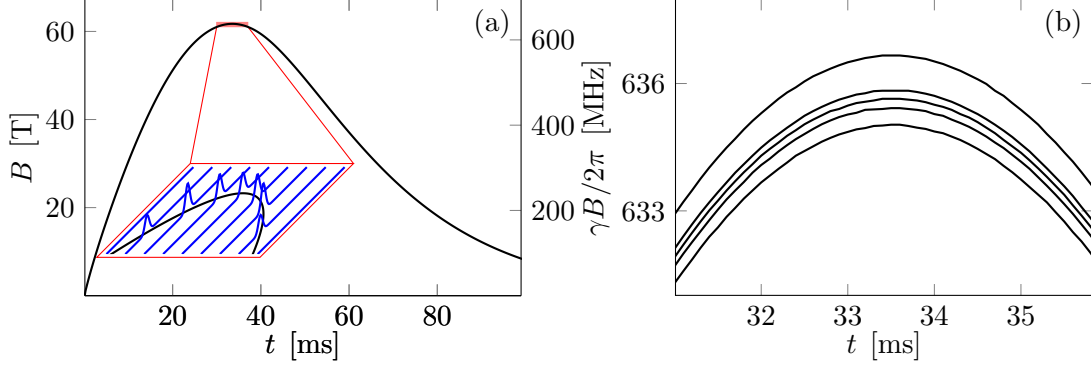


Figure 3.4: (a) Typical time dependence of a pulsed magnetic field at the HZDR estimated from shunt resistor (frequency values $\gamma B/2\pi$ are for metallic aluminum). Only a very short time frame is available for NMR measurements and the Larmor precession becomes time-dependent (red box). (b) Typical decay of obtained field maxima for multiple pulses during a day (curve scaled according to NMR field fit).

The unique experimental conditions require a spectrometer that can record multiple traces in quick succession (without immediate averaging) and has a large bandwidth compared with static field counterparts, cf. Fig. 3.4b. Details on the home-built setups, used at the HLD, the LNCMI-T, and the WHMFL can be found in literature [12, 71, 107].

Early on, it was noticed that the frequency modulation due to the inherent time dependence of the magnetic field produces artifacts when transforming into the frequency-domain using a conventional Fourier transform [30, 58]. Methods that take the time dependence of the magnetic field into account to perform a demodulation were developed by Meier and Haase [72]. Based on the derivative of phase of the complex NMR signal [72], the magnetic field can be described by a polynomial fit,

$$B_{\text{fit}}(t) = B_{\text{max}} \left\{ 1 - \alpha (t - t_{\text{max}})^2 + \beta (t - t_{\text{max}})^3 \right\}. \quad (3.1)$$

This description was then used to demodulate a digitized FID $y_j[t]$ starting at t_j into $\tilde{y}_j[t]$ according to

$$\tilde{y}_j[t] = y_j[t] \exp \left(-i\phi_j(t_j) - i\gamma \int_{t_j}^t \{B_{\text{fit}}(t') - B_{\text{fit}}(t_j)\} dt' \right). \quad (3.2)$$

The multiplication with the complex exponential function is equivalent to a shift of the

frequency scale in the spectral domain. The sum $\tilde{y}[t]$ over N FIDs was then defined as

$$\tilde{y}[t] = \frac{1}{N} \sum_{j=1}^N \tilde{y}_j[t]. \quad (3.3)$$

Using this framework, Meier et al. demonstrated signal averaging in experiments with a single resonance line from ^1H in water at 7.77 T and from ^2D in D_2O at 62 T (in both cases GdCl_3 was added as a relaxation agent) [72]. Giving almost the expected gain in signal-to-noise ratio, these experiments showed that the nuclear spins were not subjected to a detrimental amount of field noise.

A similar method was also proposed for use in quasi-static DC fields [28, 41] to compensate for small field fluctuations.

In an experiment with multiple signals, however, this approach fails to take the time-dependence of frequency differences (shift multiplied by field difference) into account and the field can not as easily be obtained from the acquired traces but prior filtering is required. A detailed discussion will be given in the next chapter.

The first materials science driven publication showed the successful recording of quadrupolar split ^{63}Cu satellite signals in $\text{YBa}_2\text{Cu}_3\text{O}_{6.51}$ [107]. However, the obtained SNR in the measurements was low, and no new insights into the physics of the material were revealed.

CHAPTER 4

A new approach: field and intensity corrected spectra in pulsed magnetic fields

Within this chapter, the challenges to obtaining NMR spectra in pulsed high-field magnets will be discussed, and a method to produce signal averaged broad frequency spectra using field-stepped FIDs will be introduced. Several additional steps are required compared with the static and quasi-static field counterparts since the time-dependent magnetic field introduces variations of spectral intensities as well as modulations of the NMR signal, effectively shifting the resonances.

Data acquired during a field pulse typically contain multiple traces j with NMR signals in them, all excited by different RF pulses. Each trace provides information about different, most likely overlapping, parts of the entire spectrum since they were acquired at a different field, but with the same carrier frequency.

In order to combine these, systematic intensity corrections need to be implemented. Furthermore, the time dependence of the relative magnetic field $B(t)/B_{\max}$ needs to be determined and used in a Fourier transform that utilizes time-dependent base functions to obtain one segment of the spectrum from each trace j . Finally, after a phase adjustment, a signal averaged broad frequency spectrum can be assembled. The sequence of steps is shown in Fig. 4.1 and comprises

a: manual selection of traces that contain FIDs

b - e: determination of the relative magnetic field (i.e., $B(t)/B_{\max}$)

b: manual estimation of the time dependence of the magnetic field by identifying a single spectral maximum in the raw FTs

c: application of a different frequency-domain filter for each FID j

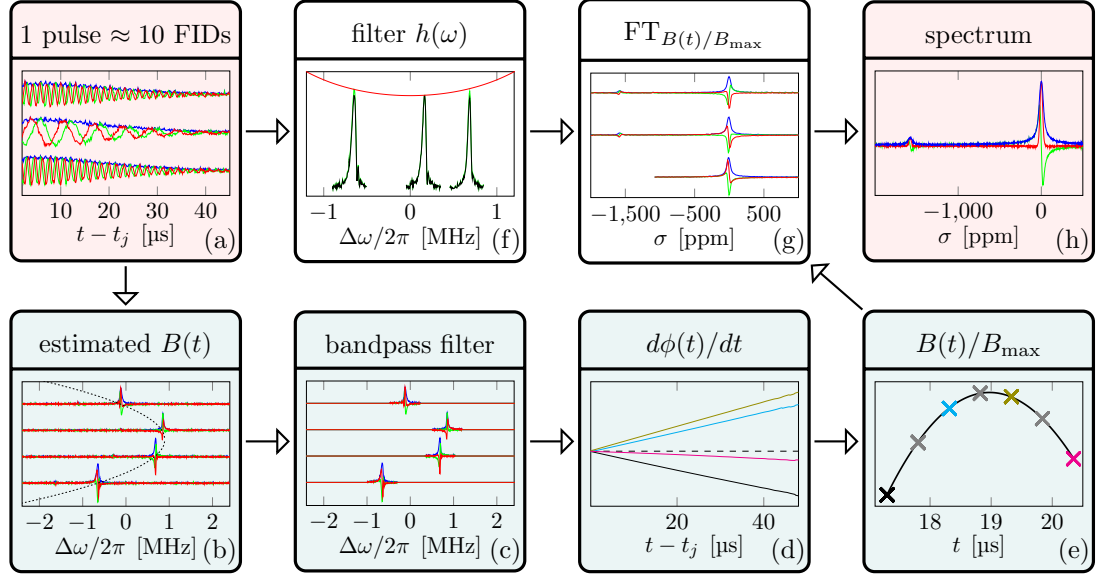


Figure 4.1: Sequence of data analysis steps to obtain NMR spectra in a pulsed field (details are in the main text).

d, e: fit of the time-derivative of the complex phase of each filtered trace to a single polynomial function that describes the magnetic field in terms of the time-dependent Larmor frequency $\Omega(t)$, and, after normalization, gives $B(t)/B_{\max}$

e: intensity correction for off-resonance excitation

f: Fourier transform with time-dependent base functions according to $B(t)/B_{\max}$

g: adjustment of the phase of each spectrum and combination all segments to a single spectrum

For the discussion, after considering the Larmor precession in terms of field-dependent and field-independent interactions in Sect. 4.1, spectra modulated by a $B(t)$ will be shown in Sect. 4.2.

Aimed at an interested reader, detailed and rather technical discussions on intensity corrections, field determination, corrections to the Fourier transform, and analysis of T_1 relaxation will be given in Sect. 4.3 - 4.6.

4.1 Nuclear spins in a changing magnetic field

In order to understand the consequences of a changing magnetic field for NMR, we describe a nuclear spin in a time-dependent magnetic field $B(t)$ with a model Hamiltonian \mathcal{H} .

We include a part \hat{H}_B that is proportional to the applied field B (e.g., Zeeman interaction and chemical shifts) and a part \hat{H}_{in} that is independent of it (e.g., quadrupolar interaction in first order or nuclear dipole interaction),

$$\mathcal{H}(t) = \mathcal{H}_B(t) + \mathcal{H}_{\text{in}}. \quad (4.1)$$

4.1.1 Field-dependent contributions

Here, due to the large magnetic field, the Zeeman term and thus \mathcal{H}_B is the most significant one. Introducing an effective gyromagnetic ratio $\tilde{\gamma}$ that includes any shift δ_α (either isotropic or for a single orientation), it is given by

$$\mathcal{H}_B(t) = \tilde{\gamma} \hbar B(t) \hat{I}_z, \quad (4.2)$$

$$\tilde{\gamma} = \gamma(1 + \delta_\alpha), \quad (4.3)$$

with \hat{I}_z being the spin operator in z direction. Here, \mathcal{H}_B introduces a time dependence to the Larmor precession that does not exist in a static magnetic field.

In many materials, the hyperfine interaction of the nuclei with conduction electrons also yields a contribution that is proportional to the applied field provided that the magnetization is a linear response, e.g., in common metals. In this case, we include the resulting Knight shift in the effective gyromagnetic ratio $\tilde{\gamma}$.

4.1.2 Field-independent contributions

The nuclear magnetic dipole-dipole interaction is relevant in most NMR investigations and does not depend on the applied magnetic field. While broadening the spectrum, i.e., decreasing the spin-spin relaxation time T_2 , it does not produce any average frequency shift but modifies the decay envelope of the FID. However, in the context of the following pulsed field experiments, the additional broadening is small compared with the inhomogeneity of the applied magnetic field and therefore does not require special treatment in this analysis.

The most commonly encountered field-independent (and thus part of \mathcal{H}_{in}) contribution besides the nuclear dipole-dipole interaction originates from the nuclear electric quadrupole interaction of a spin I that is described by \mathcal{H}_Q in Sect. 2.2. In case of a half-integer spin $I > 1/2$, as most commonly encountered, and an electric field gradient (EFG), \mathcal{H}_Q produces a orientation dependent splitting into the central transition (CT) and $2I - 1$ satellite transitions (ST) that are offset by $(m - 1/2)\omega'_Q$ (with $m = -I + 1, \dots, I$ and ω'_Q being the orientation-dependent quadrupole frequency).

The hyperfine interaction of the nuclei with localized electronic spins in a material can also produce quite a complex relationship between the Larmor precession and the applied field. Here, we will only consider contributions from the time-average $\langle \hat{S}_z \rangle_k$ of the z component of the electronic spins k and use coupling constants A_k for the description of the Hamiltonian according to

$$\mathcal{H}_{\text{hf}} = \sum_k A_k \langle \hat{S}_z \rangle_k \hat{I}_z, \quad (4.4)$$

$$= \hbar \omega_{\text{hf}} \hat{I}_z, \quad (4.5)$$

$$\omega_{\text{hf}} = \sum_k A_k \langle \hat{S}_z \rangle_k \quad (4.6)$$

In Ch. 6, we will discuss measurements on a material that exhibits a constant magnetization within in a large field range, i.e., the values of $\langle \hat{S}_z \rangle_k$ do not depend on $B(t)$. In this special case, \mathcal{H}_{hf} becomes part of \mathcal{H}_{in} as well.

In presence of \mathcal{H}_Q and a field-independent \mathcal{H}_{hf} , the contribution to the Larmor frequency in z -direction of a single spin then is

$$\omega_{\text{in}} = s\omega'_Q + \omega_{\text{hf}} \quad (4.7)$$

with $s = -(I - 1/2), \dots, (I - 1/2)$ depending on the transition (CT and ST).

4.1.3 Larmor precession

According to the Hamiltonian from Eq. (4.1), we write the field-dependent Larmor frequency of the spin as

$$\omega_L(t) = -\tilde{\gamma} B_{\text{max}} \frac{B(t)}{B_{\text{max}}} + \omega_{\text{in}} \equiv \omega_B \frac{B(t)}{B_{\text{max}}} + \omega_{\text{in}}, \quad (4.8)$$

where ω_{in} contains the field-independent contributions from Eq. (4.7) and ω_B describes the maximum contribution due to the field-dependent part (equivalent to the contribution at maximum field B_{max}). Note the reduced dependence only on the relative magnetic field $B(t)/B_{\text{max}}$ instead of $B(t)$ in Eq. (4.8).

Similar to the velocity of an accelerated object in classical mechanics, the Larmor frequency $\omega_L(t)$ defined by Eq. (4.8) is a differential quantity and changes with time. As a consequence, the complex time-domain signal $y(t)$, i.e., the FID, from n different spin

species j (with species-dependent ω_B and ω_{in}) also depends on $B(t)/B_{\text{max}}$,

$$y(t) = \sum_j^n f_j(t) e^{i\phi_j(t)}, \quad (4.9)$$

$$\phi_j(t) = - \int_{t_0}^t \left[\omega_B \frac{B(t')}{B_{\text{max}}} + \omega_{\text{in}} \right] dt' + \phi_j(t_0), \quad (4.10)$$

with the initial phase $\phi_j(t_0)$ and $f_j(t)$ describing the intensity and decay of the signals. Usually, NMR signals are demodulated with a frequency ω_0 during the acquisition, see Sect. 2.6.1, which is equivalent to a description in a rotating frame with the same frequency. The associated phase $\varphi_j(t)$ is then given by

$$\varphi_j(t) = \phi_j(t) - \omega_0 \Delta t, \quad (4.11)$$

$$\Delta t = t - t_0. \quad (4.12)$$

4.2 Spectral artifacts

The consequences of a time-dependent field can best be seen using computer-simulated FIDs according to Eq. (4.9) and (4.10) as details are obscured by noise in a real measurement. As the signal decay is mostly caused by the field's inhomogeneity, it is reasonable to use a common decay function with different amplitudes c_j for all signals, i.e., $f_j(t) = c_j f(t)$. A difference in shift values $\Delta\delta$ will only lead to a minor change of the decay time constants by a factor of $1/(1 + \Delta\delta)$ and can thus be ignored.

The left hand side of Fig. 4.2 shows three different simulated FIDs $y(t)$ with $\omega_{\text{in}} = 0$ in the rotating frame with a magnetic field $B(t)$ that increases linearly with a rate of $\gamma dB/dt/2\pi = \beta = 250 \text{ MHz s}^{-1}$ and starts at $\gamma B(0)/2\pi = \alpha = 100 \text{ MHz}$ according to

$$\gamma B(t)/2\pi = \alpha + \beta t. \quad (4.13)$$

With an exponential decay (time constant $\tau = 50 \text{ }\mu\text{s}$) the superposition $y(t)$ of two signals

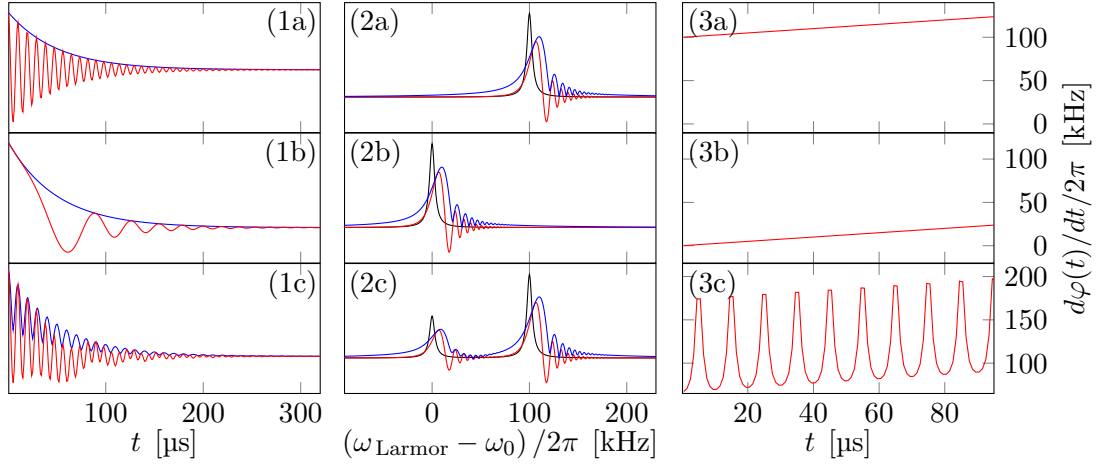


Figure 4.2: (1) Numerical simulated FIDs with a slowly changing magnetic field. The first one starts with a higher frequency than the rotating frame (a), the second one starts at the frequency of the rotating frame (b) and the last one is the superposition of both (c). (2) Real part (red) and absolute value (blue) of the Fourier transform and the corresponding static field spectra (real part, black). (3) The derivative of the argument φ in the rotating frame with $\omega_0 = 2\pi\alpha$ of all three FIDs.

with shifts of $\delta_1 = 1000$ ppm and $\delta_2 = 0$ ppm and amplitudes $A_2/A_1 = 2$ is then given by

$$y(t) = A_1 \exp[i\phi_1(t)] \exp(-t/\tau) + A_2 \exp[i\phi_2(t)] \exp(-t/\tau), \quad (4.14)$$

$$\phi_j(t) = \gamma(1 + \delta_j) \int_0^t B(t') dt' = 2\pi(1 + \delta_j) \left[\alpha t + \frac{\beta}{2} t^2 \right]. \quad (4.15)$$

The associated Fourier transform spectra (middle column in Fig. 4.2, red and blue curves, frequency scale shifted by $\omega_0/2\pi = -100$ MHz) are modulated towards higher frequencies and show artifacts that are not present in a static field counterpart (black curves). Therefore, it becomes evident that a demodulation is necessary to obtain useful spectra. However, to remove the effects of the changing magnetic field, first, its precise time-dependence has to be known. As mentioned previously, it was established in Ref. [72] that the derivative of the argument of the complex trace can be used for the determination, cf. Fig. 4.2.3a and Fig. 4.2.3b.

In case of a superposition of multiple signals with different frequencies however, this produces an oscillating curve, cf. Fig. 4.2.3c. In case of two constituents with amplitudes c_1 and c_2 , a modulation appears. This can be understood by switching to the rotating frame (red axes) of the stronger component (with $\phi_1(t)$ in Fig. 4.3). Note that this

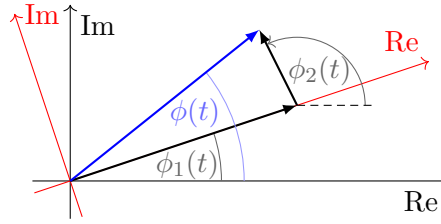


Figure 4.3: Origin of oscillations of the phase in case of two signals. The phase $\phi_2(t)$ of the weaker component modulates to the phase $\phi_1(t)$ of the stronger component.

rotating frame becomes weakly accelerated due to the increasing field which corresponds to the overall increase of the minima and maxima in Fig. 4.2.3c. Within this frame, only a small rotation caused by $\phi_2(t)$ is added with an effective angle of $\phi_2(t) - \phi_1(t)$. Therefore, the period of the modulation is given by the inverse of the frequency difference and the amplitude decreases if c_1/c_2 becomes larger.

4.3 Frequency-dependent intensity modifications

Due to the large frequency offsets in a pulsed field NMR experiment, the intensities of the observed signals get modified by the receiving tank circuit as well as the excitation pulse. Because typical resonance frequencies are rather large, the most prominent systematic modification of the observed signal amplitudes and phases is caused by the limited bandwidth of the excitation. On the other hand, the effect of the limited bandwidth of detection from the resonator is usually smaller due to the low quality factor Q .

4.3.1 Off-resonance excitation

In case of a spin $I = 1/2$ or a weak excitation in case of a system with a quadrupole splitting, the magnetization \mathbf{M} after a rectangular RF pulse of length τ and field strength B_{RF} can be calculated using rotation matrices that describe the offset-dependent rotation around an effective axis and angle [23]. The effective RF field B_{eff} is given by

$$B_{\text{eff}} = \sqrt{B_{\text{RF}}^2 + \frac{\Delta\omega^2}{\tilde{\gamma}^2}} \quad (4.16)$$

and tilted (relative to the z -axis) by an angle θ ¹

$$\theta = \arctan\left(\frac{\gamma B_{\text{RF}}}{\Delta\omega}\right). \quad (4.17)$$

The effective nutation angle β_{eff} increases with the offset and is given by

$$\beta_{\text{eff}} = -\gamma B_{\text{eff}} \tau. \quad (4.18)$$

Starting with a magnetization \mathbf{M}_0 along the z -axis, the relevant rotation matrices are given by

$$\mathcal{R}_x(\theta) = \begin{pmatrix} 1 & 0 & 0 \\ 0 & \cos \theta & -\sin \theta \\ 0 & \sin \theta & \cos \theta \end{pmatrix}, \quad (4.19)$$

$$\mathcal{R}_z(\beta_{\text{eff}}) = \begin{pmatrix} \cos \beta_{\text{eff}} & -\sin \beta_{\text{eff}} & 0 \\ \sin \beta_{\text{eff}} & \cos \beta_{\text{eff}} & 0 \\ 0 & 0 & 1 \end{pmatrix}, \quad (4.20)$$

and the magnetization after the RF pulse is

$$\mathbf{M} = \mathcal{R}_x^{-1}(\theta) \mathcal{R}_z(\beta_{\text{eff}}) \mathcal{R}_x(\theta) \mathbf{M}_0 \quad (4.21)$$

$$= M_0 \begin{pmatrix} \sin \beta_{\text{eff}} \sin \theta \\ (1 - \cos \beta_{\text{eff}}) \sin \theta \cos \theta \\ \cos^2 \theta + \cos \beta_{\text{eff}} \sin^2 \theta \end{pmatrix}. \quad (4.22)$$

The amplitude A of the induced voltage is proportional to the absolute value of transverse magnetization

$$A \propto \sqrt{M_x^2 + M_y^2} = \sin \theta \sqrt{\sin^2 \beta_{\text{eff}} + (1 - \cos \beta_{\text{eff}})^2 \cos^2 \theta} \quad (4.23)$$

and has a phase shift $\alpha = \arctan(M_y/M_x)$ relative to the on-resonance case.

¹ Within this section, \arctan denominates the arc tangent within the respective quadrant, commonly also referred to as atan2 or arctan2 function.

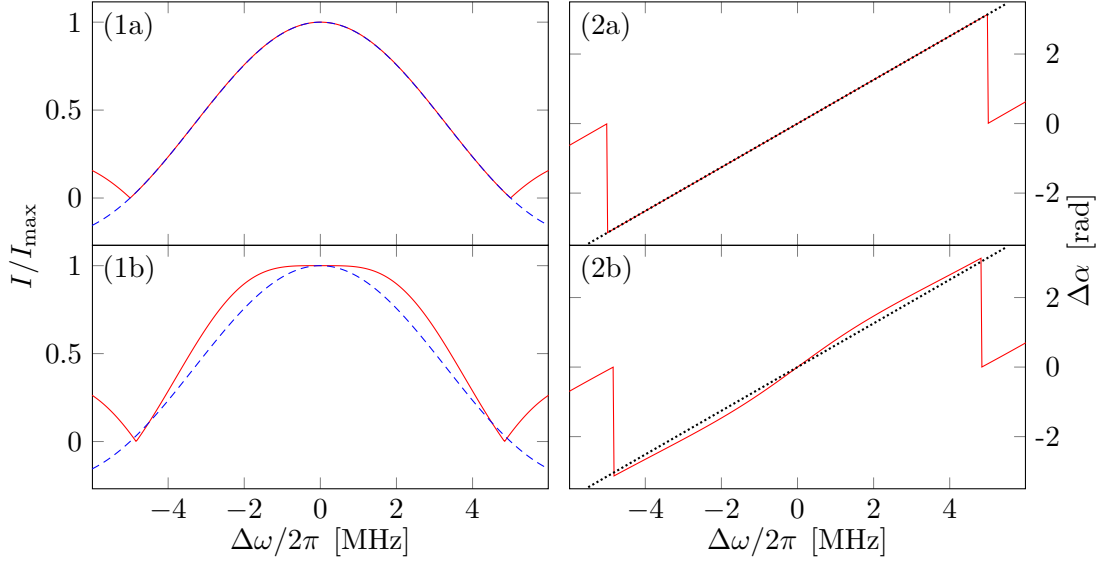


Figure 4.4: (1) Normalized intensity I/I_{\max} of the transverse magnetization (red) and a sinc function (blue, dashed) for a 10° (a) and a 90° pulse (b) as a function of the off-resonance frequency for a rectangular $\tau = 200$ ns pulse. (2) Phase shift $\Delta\alpha$ of the transverse magnetization relative to on-resonance excitation (red). Dotted line is a guide to the eye (linear with a slope of π/τ).

As can be seen in Fig. 4.4, the normalized intensity I/I_{\max} for a small excitation angle (at resonance) is well described by a normalized sinc function

$$\text{sinc}(x) = \sin(\pi x) / (\pi x), \quad (4.24)$$

but deviates for larger excitation angles. Furthermore, the phase $\Delta\alpha$ relative to the case of on-resonance excitation has linear dependence on the offset frequency.

Due to the required high bandwidth and thus short RF pulses, the excitation angles are typically small in a pulsed field experiment. Therefore, in most applications, a sinc function can be assumed, and knowledge of the RF field strength is not needed for analysis. The alterations to the intensity of off-resonant signals can most easily be corrected with a frequency domain filter $h(\Delta\omega)$. For this, the inverse of the sinc function can be used in the small excitation angle case. However, as the sinc function has nodes at $\Delta\omega = 2\pi/\tau$, a cutoff $\Delta\omega_{\text{cutoff}}$ needs to be introduced to circumvent the resulting divergence of the inverse as well as the increasing amplification that results in a decreased signal-to-noise ratio.

Since the time-dependence of the magnetic field, given by the change of Larmor frequency during one FID, typically is more than an order of magnitude smaller compared to the

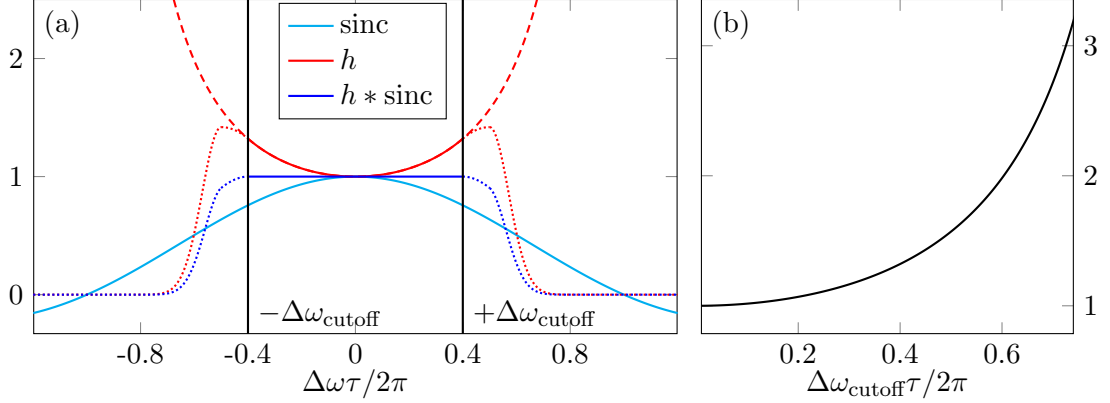


Figure 4.5: (a) Intensity correction filter $h(\Delta\omega)$ to compensate for off-resonance excitation. (b) Maximum value of $h(\Delta\omega)$ within the used frequency range as a function of the cutoff frequency.

bandwidth of $h(\Delta\omega)$, it does not need to be taken into account at this stage. Furthermore, it is advantageous to continue the filter smoothly beyond the cutoff frequency, but the precise shape of it is not critical.

In all following chapters, the filter $h(\Delta\omega)$ was chosen as

$$h(\Delta\omega) = \begin{cases} h_0(\Delta\omega) = \frac{1}{\text{sinc}(\frac{\Delta\omega\tau}{2\pi})}, & 0.0 \leq |\Delta\omega\tau/2\pi| \leq 0.4 \\ h_1(\Delta\omega) = a_2 \left(\left| \frac{\Delta\omega\tau}{2\pi} \right| - 0.5 \right)^2 + a_0, & 0.4 \leq |\Delta\omega\tau/2\pi| \leq 0.5 \\ h_2(\Delta\omega) = a_0 \exp\left(-\frac{(\omega\tau-1)^2}{0.04\pi^2}\right), & 0.5 \leq |\Delta\omega\tau/2\pi| \end{cases} \quad (4.25)$$

Here, $h_1(\Delta\omega)$ is a quadratic function with its maximum at $\Delta\omega\tau/2\pi = 0.5$ that has the same value and slope at $\Delta\omega\tau/2\pi = 0.4$. Its constant prefactors are then given by

$$a_2 = -5\pi\tau^2 \left\{ \sin(0.4\pi) - \frac{0.4\pi\tau \cos(0.4\pi)}{\sin^2(0.4\pi)} \right\}, \quad (4.26)$$

$$a_0 = \frac{1}{\text{sinc}(0.4\pi)} - \left(\frac{0.1}{\tau} \right)^2 a_2. \quad (4.27)$$

For higher frequencies, a Gaussian function continues the filter asymptotically to zero. The filter as a function of $\Delta\omega\tau/2\pi$, its product with the corresponding sinc function and its maximal value as a function of the chosen cutoff frequency are shown in Fig. 4.5.

Note that we choose not correct for the phase shift $\Delta\alpha$ at this point. Due to its almost linear dependence on the frequency offset, cf. Fig. 4.4, it will produce a linear phase

modulation in the spectra from one FID and a phase offset between spectra from two FIDs that are recorded at slightly different fields.

4.3.2 Off-resonance detection

Apart from the excitation pulse, the signal is also modified by the receiving tank circuit of the NMR probe that can be described as a driven harmonic oscillator with losses. As described in Sect. 2.6.2, an intensity variation $g(\omega)$ as well as a phase $\Delta\alpha$ are introduced as a function of the driving frequency ω .

For a tank circuit with a resonance frequency ω_0 and quality factor of Q , using $\varepsilon = (\omega_0^2 - \omega^2)/\omega\omega_0$ they are given by

$$g(\omega) = \frac{\omega_0}{\omega} \frac{1}{\sqrt{Q^2\varepsilon^2 + 1}}, \quad (4.28)$$

$$\Delta\alpha(\omega) = \arctan\left(\frac{1}{Q\varepsilon}\right). \quad (4.29)$$

Note that Q is the quality factor of the loaded tank circuit and differs from the quality factor Q_{tuning} that can be measured using a network analyzer,

$$Q = Q_{\text{loaded}} = Q_{\text{tuning}}/2. \quad (4.30)$$

The intensity variations according to Eq. (C.1) for a resonance frequency of 500 MHz and three different quality factors is shown in Fig. 4.6a. As expected, the effect becomes more

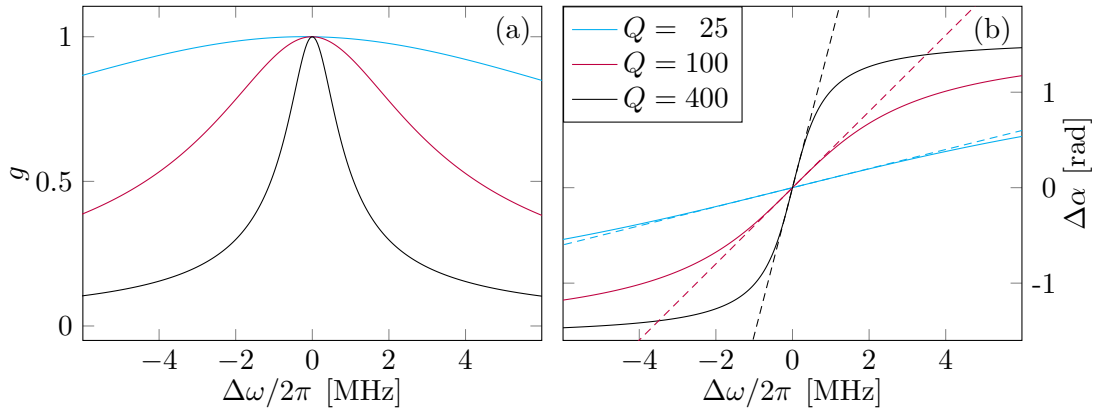


Figure 4.6: (a) Modified intensity (normalized) due to the receiving tank circuit as a function of the frequency offset $\Delta\omega = \omega - \omega_0$ with $\omega_0/2\pi = 500$ MHz for three different quality factors of the loaded tank circuit. (b) Phase $\Delta\alpha$ relative to the onresonance case with linear fits for small offsets (dashed).

important in the case of a low bandwidth (and high quality factor) resonator. Independent on the value of Q , the phase difference is always described by a linear function near the resonance frequency, cf. Fig. 4.6b. For higher quality factors, however, the frequency range where this is an accurate description becomes smaller, having significant deviations even for offsets of a few MHz. For larger frequency offsets, however, the phase difference approaches values of $\Delta\alpha \rightarrow \pm\pi/2$ asymptotically.

4.4 Field determination

As previously mentioned, cf. Eq. (4.10), the phase $\phi(t)$ (or $\varphi(t)$ in the rotating frame) of an NMR signal during the free induction decay is related to the applied magnetic field $B(t)$. Taking the time derivative, we find

$$\frac{d\phi(t)}{dt} = \omega_B \frac{B(t)}{B_{\max}} + \omega_{\text{in}}, \quad (4.31)$$

$$\frac{d\varphi(t)}{dt} = \omega_B \frac{B(t)}{B_{\max}} + \omega_{\text{in}} - \omega_0. \quad (4.32)$$

Therefore, the time dependence of the relative applied magnetic field $B_k(t)/B_{\max}$ during an FID k could be obtained as long as ω_B and ω_{in} were known,

$$\frac{B_k(t)}{B_{\max}} = \frac{d\phi_k(t)/dt - \omega_{\text{in}}}{\omega_B}, \quad (4.33)$$

$$= \frac{d\varphi_k(t)/dt - \omega_{\text{in}} + \omega_0}{\omega_B}, \quad (4.34)$$

$$= \frac{\omega_L(t) - \omega_{\text{in}}}{\omega_L(t_{\max}) - \omega_{\text{in}}}. \quad (4.35)$$

In case that the field-independent contribution to the Larmor frequency ω_L is much smaller than the field-dependent one ($\omega_{\text{in}} \ll \omega_B$), $B_k(t)/B_{\max}$ can be approximated as

$$\frac{B_k(t)}{B_{\max}} \approx \frac{d\phi(t)/dt}{\omega_B + \omega_{\text{in}}} = \frac{d\varphi(t)/dt + \omega_0}{\omega_B + \omega_{\text{in}}} = \frac{\omega_L(t)}{\omega_L(t_{\max})}. \quad (4.36)$$

In general, $\omega_B = \omega_L(t_{\max}) - \omega_{\text{in}}$ is not known a priori, but can be extrapolated by fitting the observed time-derivative to a polynomial function.

In practice, a NMR spectrometer records the signal of a FID k at discrete times¹ t_j

¹ Square brackets are used in the following for functions and quantities that are only defined for discrete times.

as a complex I/Q-demodulated trace $y_k[t_j]$ with the carrier frequency ω_0 . In order to recover $\varphi_k[t_j]$ from the measured data, the angle of the complex numbers $y_k[t_j]$ has to be calculated with the 2π discontinuities lifted. Within the Python programming language, for an array y of complex numbers (`numpy.ndarray` with a single/double precision data-type of `numpy.complex64` or `numpy.complex128`) this is implemented in NumPy/SciPy [45, 121] as

```
varphi=numpy.unwrap(numpy.angle(y)).
```

Based on this, the derivative for an intermediate time in between two data points is defined as

$$\frac{d\varphi_k}{dt} \left[\frac{t_{j+1} + t_j}{2} \right] \stackrel{\text{def}}{=} \frac{\varphi[t_{j+1}] - \varphi[t_j]}{t_{j+1} - t_j}, \quad (4.37)$$

for each FID k .

Due to the slow change of the magnetic field inbetween two data points, the values of $d\varphi_k/dt$ can be approximated as

$$\frac{d\varphi_k}{dt} [t_j] \approx \frac{d\varphi_k}{dt} \left[\frac{t_{j+1} + t_j}{2} \right]. \quad (4.38)$$

Within this approximation, all derivatives $d\varphi_k/dt + \omega_0$ and all discrete values of t_j where the SNR is sufficient are used for a single polynomial regression. Here, we use a continuously defined polynomial function $\Omega(t)$ of third order that describes the field in terms of the Larmor frequency of the signal that was used for the fit during the complete field pulse,

$$\Omega(t) = at^3 + bt^2 + ct + d. \quad (4.39)$$

Then, the time-dependence of the relative magnetic field is given by

$$\frac{B(t)}{B_{\max}} = \frac{\Omega(t) - \omega_{\text{in}}}{\Omega_{\max} - \omega_{\text{in}}}, \quad (4.40)$$

$$\Omega_{\max} = \max_t \{ \Omega(t) \}, \quad (4.41)$$

or in the previously discussed case of a small field-independent contribution ω_{in}

$$\frac{B(t)}{B_{\max}} = \frac{\Omega(t)}{\Omega_{\max}}. \quad (4.42)$$

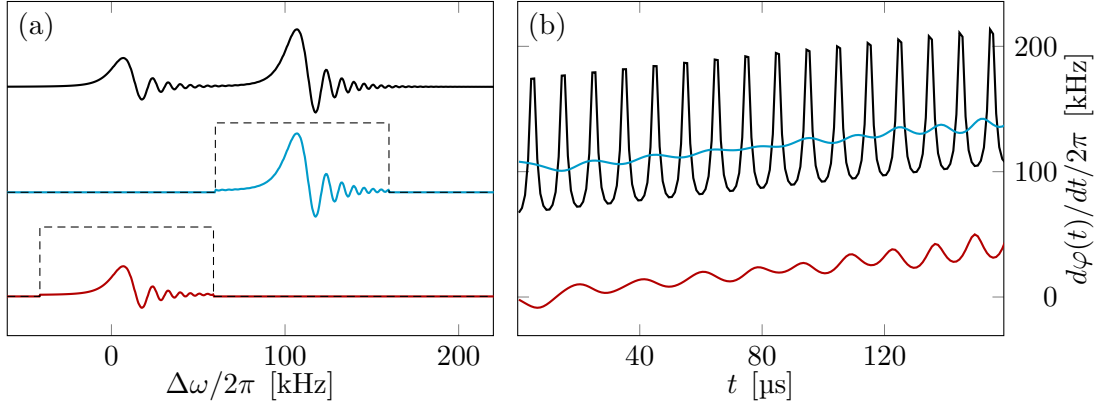


Figure 4.7: Superposition of the real part of two signals before (black, same data as in Fig. 4.2) and after (cyan, red) applying a rectangular frequency-domain filter f (dashed). (a) Real part of FT. (b) Derivatives of the argument φ of the complex trace in the rotating frame.

However, up to this point, it was assumed that the FID is produced by the signal of a single spin species. In the case of a superposition of multiple signals, filtering is needed to remove the other contributions, see Fig. 4.7.

This can be accomplished using a rectangular frequency domain filter $f_k(\Delta\omega)$ that is individual for each FID k and symmetric around a manually assigned center frequency ω_k^{center} with a bandwidth of $\Delta\omega_f$,

$$f_k(\Delta\omega) = \begin{cases} 1, & \Delta\omega + \omega_0 \in [\omega_k^{\text{center}} - \Delta\omega_f/2, \omega_k^{\text{center}} + \Delta\omega_f/2] \\ 0, & \Delta\omega + \omega_0 \notin [\omega_k^{\text{center}} - \Delta\omega_f/2, \omega_k^{\text{center}} + \Delta\omega_f/2] \end{cases}. \quad (4.43)$$

These filters are applied in the frequency-domain using the Fast Fourier Transform (FFT) and its inverse (IFFT) operation on the initial data $y_k[t_j]$ before calculating $\varphi_k[t_j]$.

4.5 Fourier transform with time-dependent base functions

Having a mathematical description of the time-dependent magnetic field, the Fourier transform (FT) needs to be modified to take this information into account.

In most modern NMR applications the fast Fourier transform (FFT) is used to obtain spectra based on the recorded time-domain data for a discrete set of frequencies. In a more general definition the conventional discrete-time Fourier transform (DTFT) of signal $y_k[t_j]$ sampled at times $t_j = 1, \dots, t_n$ assigns a complex coefficient $\tilde{Y}_k(\omega)$ to each

frequency ω according to

$$\tilde{Y}_k(\omega) = \sum_{j=1}^n y_k[t_j] \exp(-i\omega t_j). \quad (4.44)$$

The expression describes the summation over all samples after they have been rotated in the complex plane by an angle of $-\omega t_j$. More over, this is equivalent to the summation in a rotating frame that is rotated by an angle of $+\omega t_j$. For any sinusoidal signal $y_k[t_j]$, $Y_k(\omega)$ will have the largest absolute value if ω matches the signal's frequency.

In the case of a signal with a modulated phase due to a changing magnetic field, however, a similar transform that takes $B(t)/B_{\max}$ into account according to Eq. (4.10) can be defined as

$$Y_k(\omega_B, \omega_{\text{in}}) = \sum_{j=1}^n y_k[t_j] \exp\{(-i\phi(\omega_B, \omega_{\text{in}}, t_j))\} \quad (4.45)$$

$$= \sum_{j=1}^n y_k[t_j] \exp\left\{i \int_{t_1}^{t_j} \left[\omega_B \frac{B(t')}{B_{\max}} + \omega_{\text{in}}\right] dt' - i\phi(t_1)\right\}. \quad (4.46)$$

In many applications, the Zeeman interaction dominates the interactions ω_{in} that are field-independent by a few orders of magnitude due to the high magnetic field. In this case, ω_{in} one can be treated as being proportional to the magnetic field as well, only shifting the signals at lower field $B(t) < B_{\max}$ by ω_e that, at a time t , is given by

$$\omega_e = \omega_{\text{in}} \left(1 - \frac{B(t)}{B_{\max}}\right). \quad (4.47)$$

Here, the magnetic field range is typically small $B(t)/B_{\max} \approx 99\%, \dots, 100\%$. Then, the approximation is valid, if the systematic error ω_e is much smaller then the linewidth. In this case we introduce $\omega = \omega_B + \omega_{\text{in}}$ that takes the place of ω_B and drop the second, field-independent, parameter such that only one remains with

$$Y_k(\omega) = \sum_j y_k[t_j] \exp\left\{i \int_{t_1}^{t_j} \omega \frac{B(t')}{B_{\max}} dt' - i\phi(t_1)\right\}. \quad (4.48)$$

While the orthogonality of the base functions gives a canonical set of frequencies in case of the FFT, it is less clear in the case of the modified Fourier transform. Since the values

of ω can be chosen freely with sufficiently small steps between consecutive ones, this is not a problem and only produces additional computational costs (in the order a few seconds for a spectrum with 1024 data points).

However, there are two criteria, based on aliasing and the excitation bandwidth, that impose limits to the range of ω that will be discussed now.

Aliasing

Just like with the conventional discrete Fourier transform, aliasing appears, if the sampling rate is too low. In a constant field $B(t) = B_{\max}$, the sum in Eq. (4.48) does not change for a sampled sinusoidal signal $y_k[t_j]$ with a frequency of ω if the exponent increases by $2\pi i$ between two consecutive samples with a time difference of Δt . This is the case for $\omega_l = \omega + 2\pi l / \Delta t$ with $l \in \mathbb{Z}$.

In a time-dependent field, this condition depends on the particular $B(t)$. However, if the change is slow, meaning $B(t)$ only changes weakly during the FID starting at $t = t_k$, it can be approximated as

$$\omega_l = \omega + \frac{B_{\max}}{B(t_k)} \frac{l}{\Delta t}. \quad (4.49)$$

Note that ω_l and ω are the frequencies that the signal would have at B_{\max} .

As a consequence, the equivalent to the Nyquist frequency $\Delta\omega_{\text{Nyquist}}$ depends on $B(t_k)$ as well and is given by

$$\Delta\omega_{\text{Nyquist}} = \frac{B_{\max}}{B(t_k)} \frac{1}{2\Delta t}. \quad (4.50)$$

Excitation bandwidth and reconstruction of broad spectra

A filter $h(\Delta\omega)$ was previously discussed to compensate for the off-resonance excitation around the carrier frequency ω_0 of the excitation pulse. Here, a cutoff frequency $\Delta\omega_{\text{cutoff}}$ was introduced that, as a consequence, limits the accessible values of ω in a single FID. While $\Delta\omega$, ω_0 and $\Delta\omega_{\text{cutoff}}$ are genuine frequencies in the experiment, the parameter ω of the Fourier transform with time-dependent base functions is not. Again, assuming a slow change of the magnetic field ($B(t) \approx B(t_k)$), the respective cutoff values ω_k^{\pm} for ω are

$$\omega_k^{\pm} = (\omega_0 \pm \Delta\omega_{\text{cutoff}}) \frac{B_{\max}}{B(t_k)} \quad (4.51)$$

with $\omega_k \in [\omega_k^-, \omega_k^+]$.

In practice only this limitation is significant, as the sampling rate (inverse of the delay in between two consecutive samples) is only limited by the spectrometer hardware and can be chosen as high as 25 MHz in the case of the HZDR spectrometer. With a cutoff frequency of $\Delta\omega_{\text{cutoff}}/2\pi = 0.4/\tau$, this would require a pulse length of $\tau < 16$ ns for aliasing to become relevant.

Assembling broad spectra

In case of a broad frequency spectrum, it might never be fully captured within the excitation bandwidth $[\omega_k^-, \omega_k^+]$ from Eq. (4.51) that was introduced because of the intensity correction filter introduced in Sect. 4.3.1 of any $Y_k(\omega)$. Then, spectral data resulting from multiple FIDs k have to be combined. A correct description of $B(t)/B_{\text{max}}$ translates the genuine frequencies of the measurement to the associated values of ω in the combined spectrum, cf. shaded and non-shaded parts of the spectra in Fig. 4.8.

However, due to the changing excitation and detection conditions, the phase of different spectra will not be constant and needs to be adjusted first. While it is mostly possible to account for the different sources and their effects, it is not needed in case of spectral overlap between the spectra $Y_k(\omega)$ of consecutive FIDs such that $[\omega_{k-1}^-, \omega_{k-1}^+] \cap [\omega_k^-, \omega_k^+] \neq \emptyset$, cf. Fig. 4.8. In this case, the correct phase offset can be found using a numerical optimization procedure that can be continued iteratively for all k .

For this, the sum of the phase adjusted spectra, $Y_k^c(\omega)$, with k being the number of spectra already included, which equals the number of iteration steps, is defined as

$$Y_k^c(\omega) = \frac{\sum_{l=1}^k e^{-i\xi_l} Y_l(\omega)}{m_k(\omega)}. \quad (4.52)$$

In the denominator, $m_k(\omega)$ is the number of spectra that contributed to $Y_k^c(\omega)$ for given

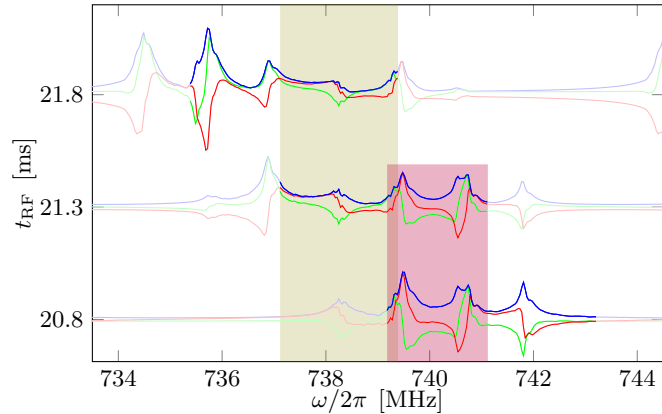


Fig. 4.8: Phase adjustment of consecutive spectra k excited at t_k (data from Ch. 6). Shaded parts of the spectra are outside of ω_k^\pm and are discarded. Only parts within $[\omega_l^-, \omega_l^+] \cap [\omega_k^-, \omega_k^+]$ with $l < k$ are relevant to iteratively adjust the phases (colored boxes).

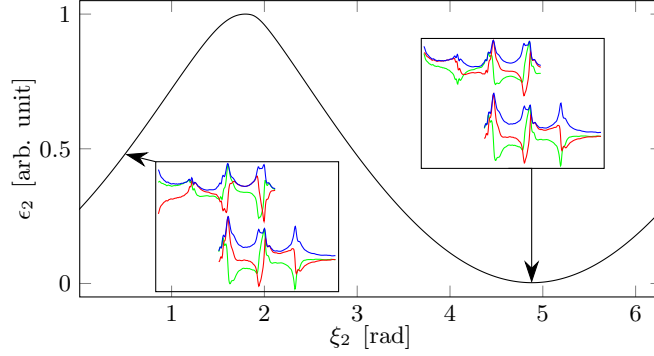


Figure 4.9: Normalized error ε_2 as a function of the correction angle ξ_2 (data from Ch. 6). Insets show magnitude (blue), real (red), and imaginary part (green) of $Y_1(\omega)$ (lower curves) and $e^{-i\xi_2}Y_2(\omega)$ (upper curves) for two values of ξ_2 .

value of ω and $Y_k^c(\omega)$ is only defined if $m_k(\omega) > 0$. Based on the previous iteration $k-1$, two functions $s_k^1(\omega)$ and $s_k^2(\omega)$ can be defined with

$$s_k^1(\omega) = |e^{-i\xi_k}Y_k(\omega)| + |Y_{k-1}^c(\omega)|, \quad (4.53)$$

$$s_k^2(\omega) = |e^{-i\xi_k}Y_k(\omega) + Y_{k-1}^c(\omega)|. \quad (4.54)$$

Starting with the first spectrum $Y_1(\omega)$, the phase ξ_1 is arbitrary ($Y_0^c(\omega)$ is empty), but all following phases ξ_k are chosen to minimize the difference ε_k with

$$\varepsilon_k = \sum_{\omega} s_k^1(\omega) - s_k^2(\omega). \quad (4.55)$$

Here, the summation covers all values of ω that are in $[\omega_k^-, \omega_k^+]$ and in $[\omega_l^-, \omega_l^+]$ of one of the previous spectra $l < k$. It reaches its minimum for the value of ξ_k that puts $e^{-i\xi_k}Y_k(\omega)$ in phase with $Y_{k-1}^c(\omega)$, cf. Fig. 4.9.

We use the *minimize* function implemented in the LMFIT package for Python [82] to find the proper value for ξ_k .

In the following, we use $Y^c(\omega)$ to denominate the final combined spectrum where all relevant $Y_k(\omega)$ are included.

Linear phase correction

While the discussed procedure corrects for phase differences of multiple spectra $Y_k(\omega)$ such that they become coherent, in general, there is still a phase modulation in the combined spectrum $Y^c(\omega)$ that is also common in static field experiments. Here, in addition to the excitation and detection conditions, the signal propagation delay through cables and

electronic components produces a linear contribution as a function of the frequency in good approximation.

In order to correct for this, we define the phase-corrected final spectrum $Y(\omega)$ with two parameters ζ_0 and ζ_1 as

$$Y(\omega) = Y^c(\omega) \exp[i(\zeta_0 + \zeta_1\omega)]. \quad (4.56)$$

4.6 Longitudinal magnetization (T_1)

The longitudinal magnetization is a more complex quantity in a pulsed magnetic field compared with the static counterpart. Due to the limited time that is available during the field pulse and the changing magnetic field, excitation rarely happens with a thermally equilibrated system. Furthermore, with the changing off-resonance excitation conditions, the effect of every RF pulse is different and the time in between two consecutive pulses is often too short for the system to return to equilibrium.

In experiments where the intensities are of particular importance, e.g., in relaxation measurements, these effects have to be taken into account.

According to Eq. (4.22), starting with an initial longitudinal magnetization M_z^0 the z -component M_z after a rectangular RF pulse of duration τ is given by

$$M_z = M_z^0 (\cos^2 \theta + \cos \beta \sin^2 \theta), \quad (4.57)$$

$$\beta = -\gamma \sqrt{B_{\text{RF}}^2 + \Delta\omega^2 / \gamma^2 \tau}, \quad (4.58)$$

$$\theta = \arctan(\gamma B_{\text{RF}} / \Delta\omega). \quad (4.59)$$

Here, the RF field strength of the circular polarized field is B_{RF} . Since β and θ depend on the frequency offset $\Delta\omega$ during excitation, they have an implicate time dependence.

In the experiment, the induced voltage in the RF coil is proportional to the projection of the magnetization vector perpendicular to the z -axis M_\perp . It also depends on M_z^0 and is given by

$$M_\perp = M_z^0 \sin \theta \sqrt{\sin^2 \beta + (1 - \cos \beta)^2 \cos^2 \theta}. \quad (4.60)$$

The relaxation process of the longitudinal magnetization $M_z(t_j)$ from a time t_j to a time $t_{j+1} = t_j + T$ towards equilibrium is usually described by

$$M_z(t_{j+1}) = M_z^{\text{eq}} - [M_z^{\text{eq}} - M_z(t_j)] e^{-T/T_1}. \quad (4.61)$$

The longitudinal magnetization, therefore, depends on the history of the applied RF pulses together with their offset frequencies. Thus, any model used to describe the intensities in a pulsed magnetic field experiment does not only need to include relaxation times and observed intensities but also the history of all applied RF pulses including the lengths, amplitudes, and frequency offsets. Such a model that also takes the finite bandwidth of the receiving tank circuit into account can be found in Lis. E.2 (implemented in Python).

Note that in presence of a quadrupole splitting a more complicated model becomes necessary since Eq. (4.61) is not a valid description for the relaxation dynamics anymore [108].

Similar to the *single-scan Fourier transform method* [48] which uses small angle excitation to monitor the relaxation process, the sequence of observed intensities can be used to extract the longitudinal relaxation time T_1 which we will demonstrate with measurements on metallic aluminum and metallic gallium in Sect. 5.2.

CHAPTER 5

Shift and spin-lattice relaxation measurements in pulsed magnetic fields

In the following, the methods that were introduced in the last chapter will be tested in a ^{27}Al Knight shift measurement and spin-lattice relaxation measurements (T_1) on metallic aluminum and gallium in a pulsed magnetic field. These results have been published in Ref. [55].

5.1 Shift measurement

In order to resolve the ^{27}Al NMR Knight shift K_S of metallic aluminum powder, another compound is used as a reference to calibrate the magnetic field B_{max} and thus the frequency scale of ω to a shift scale. Here, signal averaging is performed, showing the expected gain of signal-to-noise ratio even across three independent field pulses and a value of $K_S = 1640 \text{ ppm}$, consistent with literature, cf. Ref. [11], is found.

5.1.1 Experimental

The shift experiment was performed in a *KS3* type magnet at the HLD that can produce fields up to 63 T with typical NMR observation times of about 5 ms, cf. Fig. 3.2. A field of about 55.7 T was used in three consecutive pulses with charging voltages of about 19.6 kV. The charging voltage for each field pulse was slightly adjusted according to the field-per-voltage history of the previous ones and the pre-pulse coil resistance R_{coil} to obtain Larmor frequencies close to the carrier frequency of the spectrometer, cf. Tab. 5.1. The sample was a mixture of metallic aluminum powder (Alfa Aesar, 99.97 % purity, $T_1 \approx 7.4 \text{ ms}$) and standard Linde type A zeolite powder ($T_1 \approx 1.4 \text{ ms}$) in epoxy glue with a volume of several μL at a temperature of 257 K (measured with a *PT1000* temperature

Table 5.1: Experimental parameters in the aluminum shift measurements (temperature sensor resistance R_{PT1000} , pre-pulse coil resistance R_{coil} , and charging voltage $U_{\text{capacitors}}$).

experiment	R_{PT1000}	R_{coil}	$U_{\text{capacitors}}$
2014-01-23-01	938 Ω	100.6 m Ω	19.56 kV
2014-01-23-02	939 Ω	99.9 m Ω	19.55 kV
2014-01-23-03	939 Ω	100.9 m Ω	19.57 kV

sensor before and after the field pulses). The volume density of ^{27}Al nuclei from the zeolite in the mixture was about an order of magnitude smaller ($\approx 14\%$) compared with the metal. The expected shift values relative to the commonly used standard $\text{Al}(\text{H}_2\text{O})_6\text{Cl}_3$ are $\delta_1 = K_S = 1640$ ppm for the metallic aluminum [11] and $\delta_2 = 58.7$ ppm for the zeolite [26].

The sample was placed in a small RF coil (diameter $d = 1$ mm, length $l = 1.2$ mm) with a nearly optimal filling factor that was part of a home-built probe that fits the cryostat available at the facility (inner diameter 16 mm) and allows for precise adjustment of the height within the pulsed field magnet.

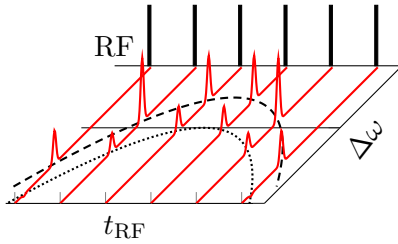


Fig. 5.1: Pulse sequence for shift measurement near the field maximum.

As sketched in Fig. 5.1, a sequence of about 100 rectangular RF pulses with a duration of $\tau = 300$ ns and a separation of about $500\ \mu\text{s}$ was applied at a fixed power level and carrier frequency equal to the resonance frequency of the tank circuit $\omega_0/2\pi = 617$ MHz (quality factor $Q = 23$).

During the field pulse, a complex I/Q-demodulated signal trace was recorded at a sampling rate of 10 MHz and later split into segments (one after each

of the RF pulses). The segments that contained FIDs were then subjected to left shifts and a baseline correction as in regular NMR experiments.

Based on the RF coil properties and the applied power level, the estimated on-resonance flip-angle is only about 17° , giving a decrease of the longitudinal magnetization by less than 5 %.

5.1.2 Results

The raw Fourier transform spectra from FIDs with sufficient signal from the three field pulses after a baseline correction and a left shift by $2\ \mu\text{s}$ are shown in Fig. 5.2. The strong, higher frequency, signal originates from the metallic aluminum.

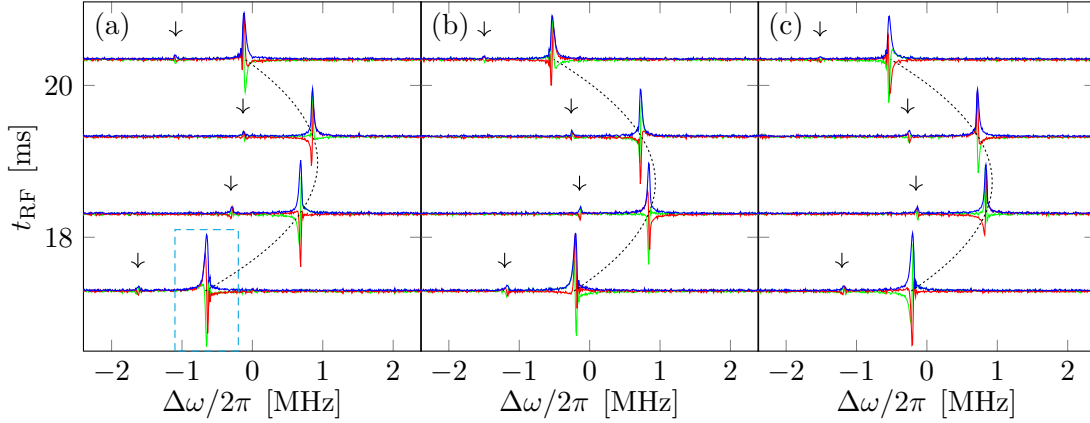


Figure 5.2: Magnitude (blue), real part (red), and imaginary part (green) of the Fourier transformed raw FIDs (only every other FID is shown) of a mixture of metallic aluminum (strong signal) and Linde type A zeolite (one order of magnitude weaker signal, indicated with black arrows), excited at different times t_{RF} near the field maximum of 55.7 T in three consecutive field pulses ((a) 2014-01-23-01, (b) 2014-01-23-02, (c) 2014-01-23-03) together with the fitted field profiles ($\Omega(t) - \omega_0$, dotted black curves). The frequency scale $\Delta\omega$ is relative to the carrier frequency of the spectrometer. The dashed teal box marks the window that is enlarged in Fig. 5.3.

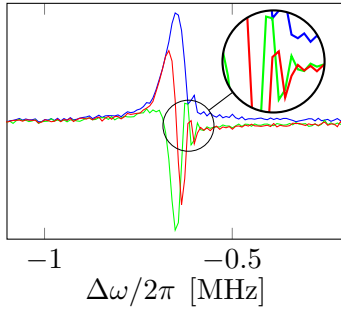


Fig. 5.3: Artifacts in raw FT spectra (enlarged from Fig. 5.2a).

At about 1 MHz lower frequency, the signal from the zeolite (marked by black arrows in Fig. 5.2a) is just barely visible.

Furthermore, modulation artifacts can be seen in the spectra from the metallic aluminum that were acquired further from the field maximum, cf. Fig. 5.3. They are only visible on one side, i.e., at higher frequencies in case of a rising field and at lower frequencies in case of a falling field.

Field fit

As first step, the time-dependence of the magnetic field in terms of the Larmor frequency $\Omega(t)$ of the metallic aluminum is determined. After applying the intensity correction filter $h(\Delta\omega)$ for the $\tau = 300$ ns pulses (with an increased bandwidth of $\omega_{\text{cutoff}}/2\pi = 0.6/\tau$), rectangular band-pass filters with a bandwidth of 700 kHz and a center frequency based on the signal from the metallic aluminum are applied in the frequency domain, see Fig. 5.4a. Then, the argument $\varphi_k[t_j]$ of the filtered trace can be calculated, see Fig. 5.4b. Finally, the derivative of $\varphi_k[t_j]$ (with ω_0 added) is fit to $\Omega(t)$ according to Eq. (4.39) to obtain the time dependence of the magnetic field in terms of the Larmor frequency of the

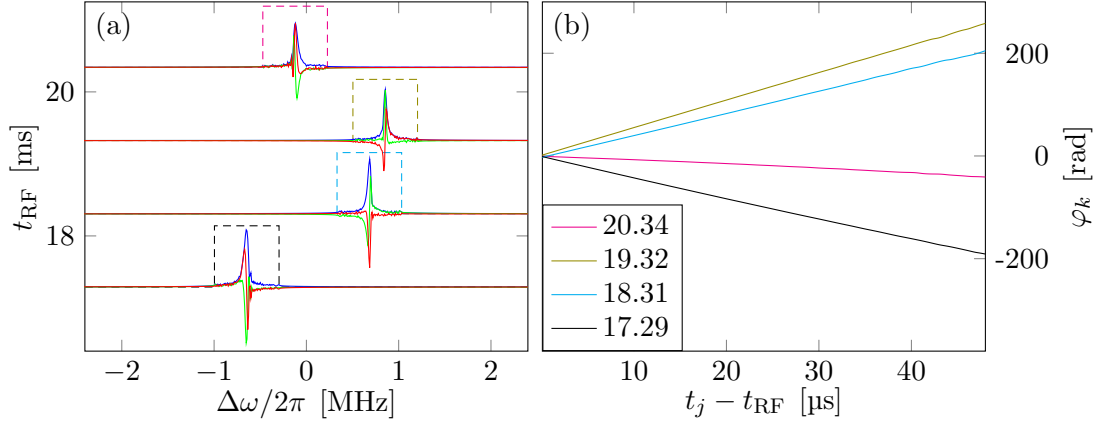


Figure 5.4: (a) Magnitude (blue), real part (red), and imaginary part (green) of the Fourier transformed filtered FIDs for field fit (data set is the same as in Fig. 5.2) only every other FID is shown). The applied frequency filters are shown as dashed curves. (b) The argument φ_k of the filtered FIDs in the rotating frame.

metallic aluminum NMR signal, see Fig. 5.5a.

The frequencies Ω_{max} at maximum fields of the three different field pulses only differ by 6.5 kHz. However, in one case, the maximum was only reached 0.3 ms later, see Fig. 5.5b, showing the limited reproducibility of the pulsed field.

Fourier transform with time-dependent base functions

The polynomial description of the magnetic field can now be used for the Fourier transform with time-dependent base functions according to Eq. (4.48). Note that in the

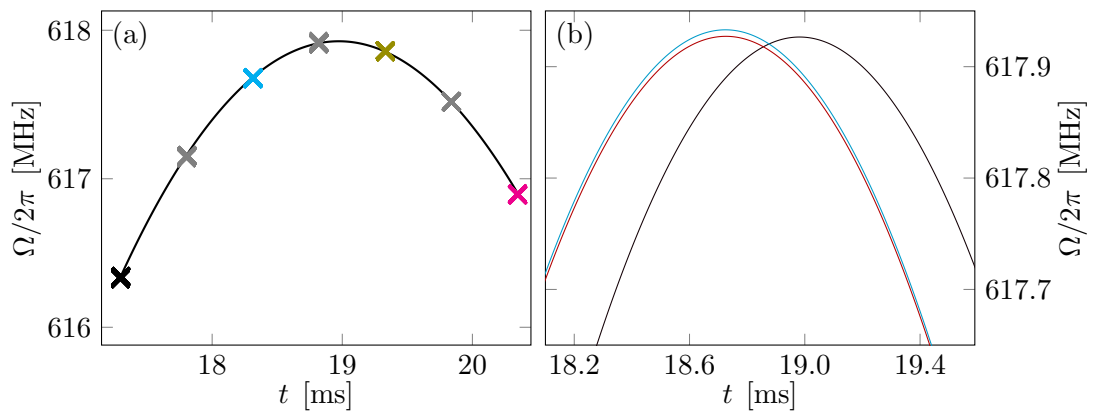


Figure 5.5: (a) Field fit for $\Omega(t)$ (data set is the same as Fig. 5.2a, grey symbols are from FIDs that were not shown in the other relevant figures). (b) The obtained polynomial function near the maximum for the three field pulses.

following, the plots are in a shift scale σ relative the maximum value Ω_{\max} of the fit for the metallic aluminum, cf. Eq. (4.41), with

$$\sigma(\omega) = \frac{\omega}{\Omega_{\max}} - 1. \quad (5.1)$$

The spectra $Y_k(\sigma)$ within the respective cutoff ranges are shown in Fig. 5.6 (same data sets as in Fig. 5.2). One can see that the FIDs that were acquired at the higher fields give access to more negative shifts. As a consequence, some FIDs were not taken at high enough field to cover the zeolite signal, e.g., at $t_{\text{RF}} = 17.29$ ms in the first field pulse (lowest curves in Fig. 5.6a).

While the intensities (magnitude) of the spectra are almost identical, they are clearly phase shifted. Therefore, a phase adjustment needs to be performed before signal averaging becomes possible. This is done with a simpler approach by minimizing the sum of the imaginary part of the spectrum from the metallic aluminum instead of the method that was introduced in Sect. 4.5.

Afterwards, the spectra can be summed up to $Y^c(\sigma)$ and a manual linear phase correction according to Eq. (4.56) (with ω replaced by σ) is performed to remove the frequency-dependent phase modulation and obtain $Y(\sigma)$.

In a last step, the shift axis is converted to a standard scale δ based on zeolite shift σ_2

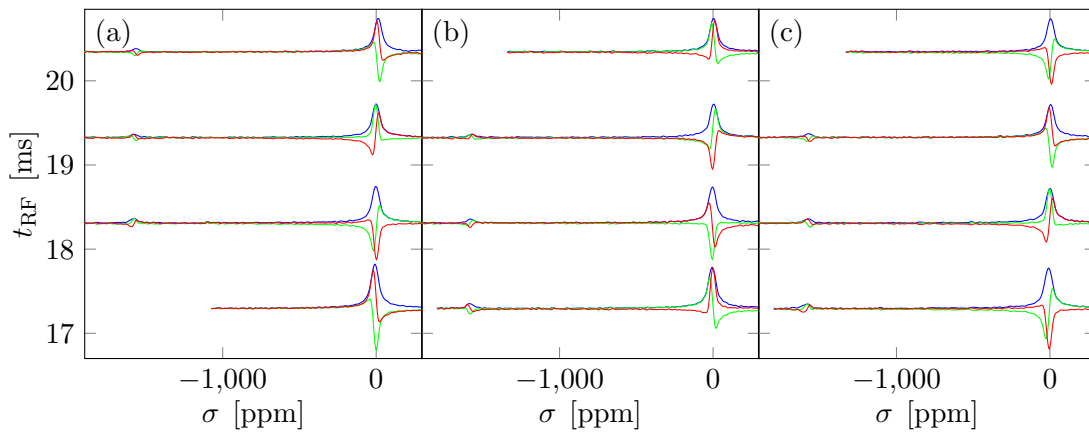


Figure 5.6: Fourier transform with time-dependent base functions according to field fits shown in Fig. 5.5 (blue: magnitude, red: real part, green: imaginary part). Bottom axis is shift relative to the metallic aluminum signal used for the fit.

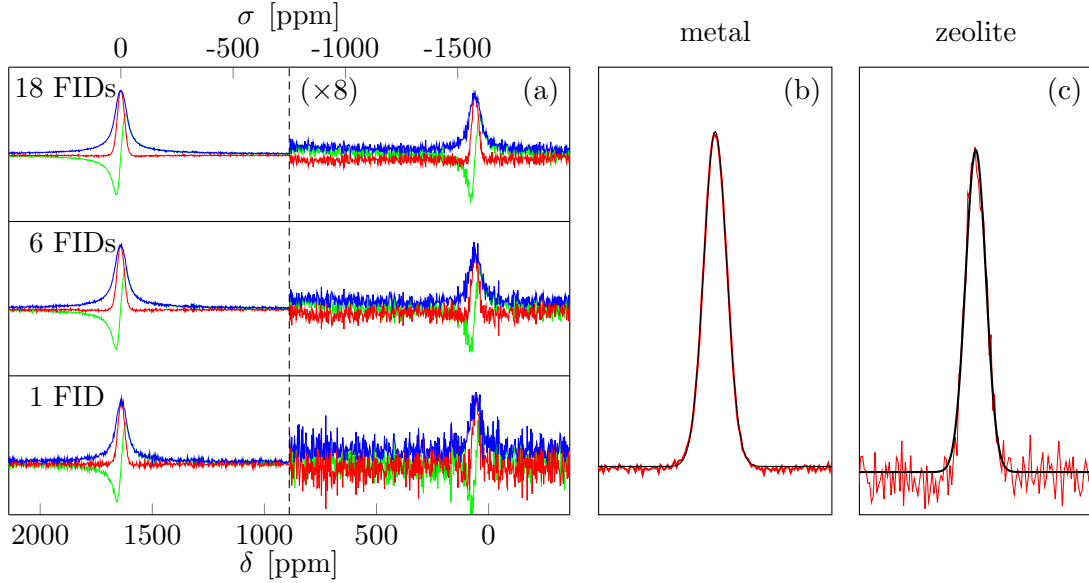


Figure 5.7: (a) Magnitude (blue), real part (red), and imaginary part (green) of the normalized ^{27}Al spectra of metallic aluminum (left) and Linde type A zeolite (right, scaled by a factor of 8) with data from different numbers of FIDs included. (b) Gaussian fit (black) to the real part of the signal from the metallic aluminum (red). (c) Gaussian fit (black) to the real part of the signal from the Linde type A zeolite (red).

from a Gaussian fit and the reference value $\delta_2 = 58.7$ ppm according to

$$\delta(\sigma) = \left[1 + \sigma - \frac{1 + \sigma_2}{1 + \delta_2} \right] / \left[\frac{1 + \sigma_2}{1 + \delta_2} \right]. \quad (5.2)$$

Fig. 5.7a shows the resulting spectra calculated from a single FID, six FIDs from a single field pulse, and 18 FIDs from three different field pulses. The increase in SNR due to the coherent averaging can clearly be seen and agrees with the expectations. Both signals show a Gaussian lineshape with a linewidth of ~ 36 ppm (FWHM) which causes the numeric uncertainty of the shift, see Fig. 5.7b and Fig. 5.7c.

The shift of the metallic aluminum is $\delta_1 = (1640 \pm 5)$ ppm in agreement with the expected value [11] and thus shows that pulsed magnetic fields can be used for the measurement of NMR shifts. While the intensities of the two components agree with the respective number of ^{27}Al nuclei in this measurement, other systems can show systematic intensity alterations, e.g., in case of a non-uniform distribution of T_1 .

5.2 Measurement of nuclear spin-lattice relaxation

The spin-lattice relaxation rate T_1 describes the return of the macroscopic longitudinal magnetization of the nuclear spin system towards its equilibrium. While it can easily be measured for most systems in a static field, obtaining it in a time-dependent magnetic field is far more difficult. The most basic concept of repeated preparation of a well-defined magnetization, either through inversion or saturation, waiting for a certain amount of time and performing a read-out measurement becomes challenging as the field pulses are only of limited reproducibility. Even more important, the need to repeat the whole experiment for a set of different delay times makes it costly time-wise.

Within this section, a method to measure T_1 in a pulsed magnetic field will be presented. By treating the time-dependent magnetic field as an asset rather than an obstacle, an adiabatic inversion caused by the changing field and a long-lasting and low-power RF pulse inverts the magnetization (as simulated in App. B). Afterward, small-angle pulses monitor the relaxation process within a single field pulse. Finally, a mathematical model that takes all relevant effects into account is used to fit the observed intensities, cf. Lis. E.2. However, the short duration of the magnetic field also limits applications of this method to systems with a short T_1 , e.g., metals.

5.2.1 Experimental

Relaxation experiments were performed at the HLD on metallic aluminum powder (Alfa Aesar, 99.97 % purity) in epoxy glue at a temperature of $T = 302$ K (measured with a *KTY81/220* temperature sensor) and a field of $B \approx 29$ T in the *LP* magnet, cf. Fig. 3.2. Experiments on metallic gallium (ESPI Metals, 5N purity) in epoxy glue were performed at a temperature of $T = 308$ K (measured with a *PT1000* temperature sensor) and a field of $B \approx 58$ T in a *KS3* type magnet, cf. Fig. 3.2. The center of both magnets was determined with preparatory low-field ^1H NMR measurements in which the line width was optimized by varying the z position of the sample.

The samples were placed in small RF coils with a high filling factor that were part of tank circuits with low quality factors. The dimensions, resonance frequencies, and quality factors are listed in Tab. 5.2.

Table 5.2: Parameters of the tank circuits for the relaxation measurements.

sample	diameter	length	resonance frequency	quality factor
aluminum	2 mm	3 mm	322.3 MHz	27
gallium	1 mm	1.5 mm	594.7 MHz	60

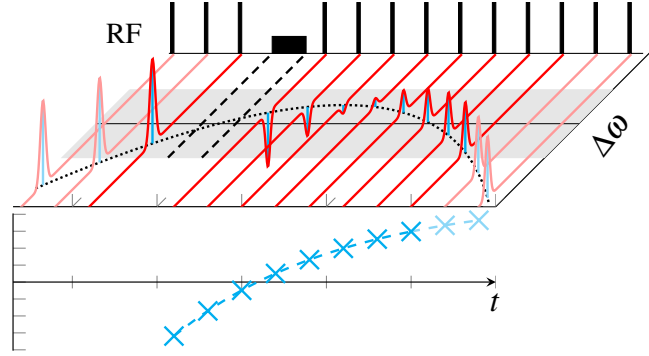


Figure 5.8: Top: Pulse sequence for a T_1 experiment with an adiabatic inversion in a pulsed magnetic field. A train of RF pulses with constant carrier frequency but two different pulse durations and power levels is used (black, on top). After the inversion by the long and weak pulse during the field upswing, short, high-bandwidth readout pulses monitor the relaxation process. Additional pulses monitor the field before the inversion pulse. Due to the time-dependent magnetic field, the Larmor frequency changes (dotted black curve) and escapes the bandwidth of excitation of the readout pulses (shaded area). Bottom: The measured intensities (cyan symbols) are used to fit a model describing the relaxation process (dashed cyan curve).

As sketched in Fig. 5.8, a sequence of rectangular RF pulses with two different durations and power levels was used. For this, a function to read pulse sequences from *XML* text files was added to the *LabVIEW* spectrometer software and a corresponding small *Python* script for the generation of such files was implemented to simplify usage and prevent human error (each read-out pulse consists of four steps, cf. App. D, each with a type and duration).

The low power levels were produced by introducing an additional signal path into the homebuilt spectrometer that included a passive attenuator, see Fig. D.1 in the appendix. The attenuation was optimized based on the degree of inversion achieved at different values since too high power levels produced a saturation instead of an inversion.

In case of the aluminum, the RF power level was $P = 40$ W for the read-out pulses and $P = 1.6$ W for the inversion field (applied for 2 ms). In case of the gallium the RF power level was set to $P = 145$ W for the read-out pulses and $P = 5$ W for the inversion field (applied for 350 μ s).

The geometrically spaced read-out pulses had a duration of $\tau = 100$ ns and an estimated RF field strength of $B_{\text{RF}} = 6$ mT, giving an estimated on-resonance tipping angle of only 1.5° for the aluminum. For the gallium, the respective values were $\tau = 200$ ns and $B_{\text{RF}} = 35$ mT, giving an estimated on-resonance tipping angle of 28° (likely lower due to limited penetration depth of the RF field).

5.2.2 Results aluminum

Fig. 5.9a shows the conventional FTs of the FIDs. The inversion field lasted from $t = 1.2$ ms until $t = 3.2$ ms and the Larmor frequency $\tilde{\gamma}B(t)$ crossed the RF field frequency around $t = 2$ ms. In addition to the inversion, the weak RF field also resulted in a loss of signal intensity that can be seen when comparing the spectra from $t_{\text{RF}} = 0.4$ ms and $t_{\text{RF}} = 3.2$ ms. The zero-crossing occurs around $t_{\text{RF}} = 6.5$ ms and the maximum frequency offset was 1.7 MHz. A total of 28 FIDs acquired in a time-window of 24.5 ms represent the relaxation process. Due to the lower SNR, several of the FIDs are excluded from the fit to $\Omega(t)$, see Fig. 5.9b. The quality of the fit, however, does not suffer from this exclusion since it remains well-determined because of the FIDs before the inversion field. By using $\Omega(t)$, the spectra for each FID are calculated in a shift scale relative to Ω_{max} without applying $h(\Delta\omega)$ to correct for the frequency offset during excitation (this correction is included in the fit model), cf. Fig. 5.10a. Each spectrum is phase-adjusted by minimizing the sum of the imaginary part individually to make them phase-coherent. The intensity I is obtained as the sum of the real part and shown in Fig. 5.10b. Here, the values for the first 10 FIDs ($t_{\text{RF}} < 6.5$ ms) are inverted manually. The fit (using the model in combination with the Levenberg-Marquart algorithm) to the relaxation model is shown

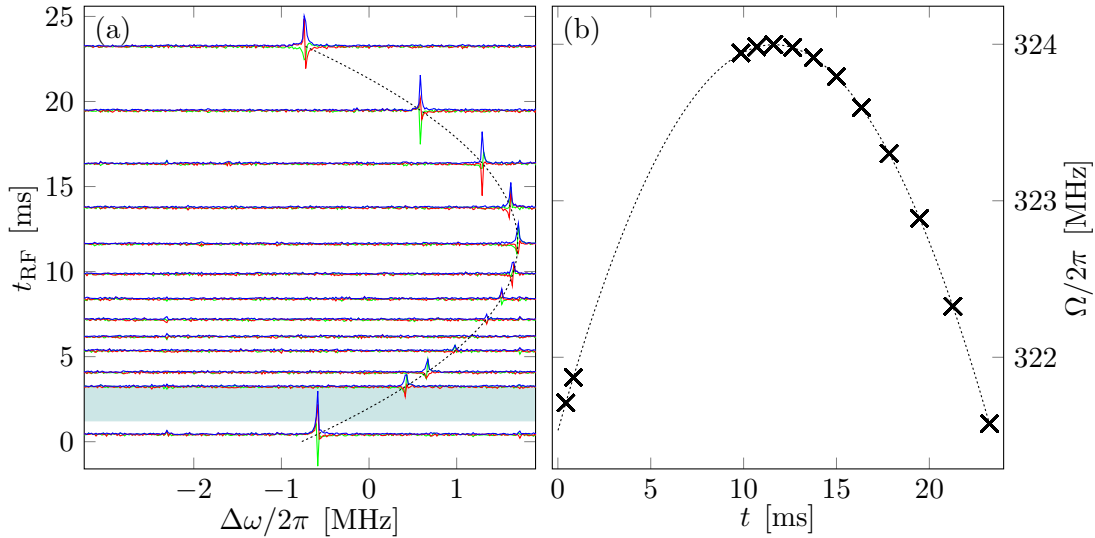


Figure 5.9: (a) Magnitude (blue), real part (red), and imaginary part (green) of the Fourier transformed raw FIDs (not all FIDs are shown) of metallic aluminum excited at different times t_{RF} near the field maximum at 29 T in the relaxation measurement with the fitted field profile (dotted black curves). The inversion field was applied from $t = 1.2$ ms to $t = 3.2$ ms (blue shaded area). (b) Field fit for $\Omega(t)$ (several FIDs were excluded for the fit because of their low intensity).

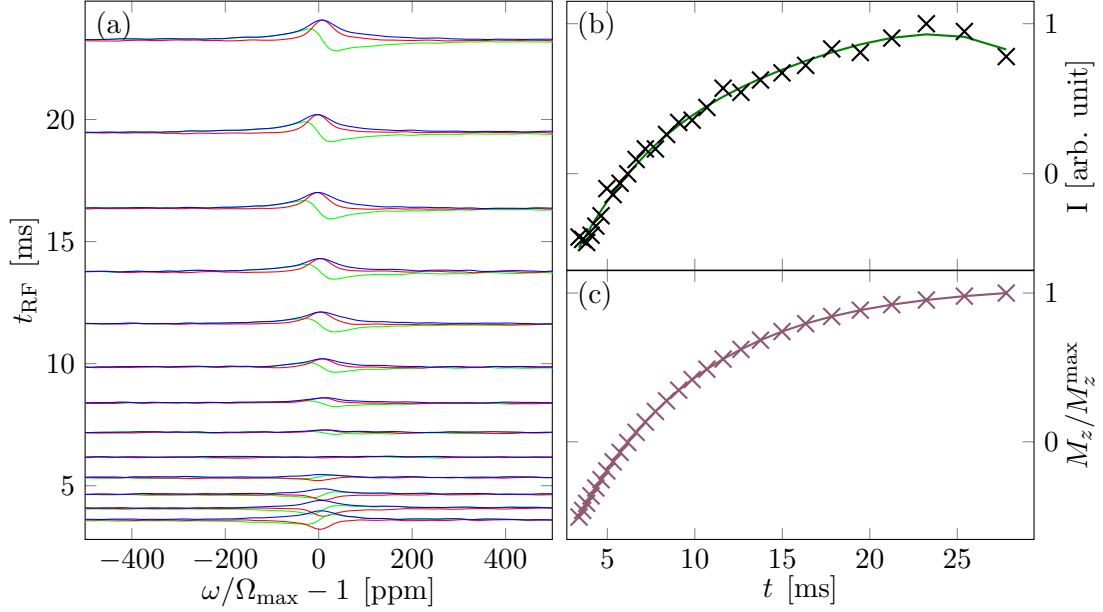


Figure 5.10: (a) Magnitude (blue), real part (red), and imaginary part (green) of the Fourier transform with time-dependent base functions after manual phase adjustment (only every second FID is shown) of metallic aluminum excited at different times t_{RF} near the field maximum at 29 T. (b) Observed intensities (black symbols) and fit to the model (green curve). (c) Normalized longitudinal magnetization from the fit model.

as the green curve in Fig. 5.10b and Fig. 5.10c shows the longitudinal magnetization of the model. The parameters, as well as error estimates, can be found in Tab. 5.3. Note that the fit value for T_1 only changes far below the margin of error if the RF field strength is assumed to be an order of magnitude smaller. We therefore find $T_1 = (7.4 \pm 0.9) \text{ ms}$ (with a 2σ confidence interval) which is larger than expected (6.13 ms [11]).

Table 5.3: Fit parameters for relaxation measurements on metallic aluminum at a temperature of $T = 302 \text{ K}$ and a field of $B \approx 29 \text{ T}$. Parameter names refer to the Python implementation in Lis. E.2.

parameter	value	error estimate σ
Brf	6 mT	fixed
tau	0.1 μs	fixed
gamma	$6.97 \times 10^7 \text{ rad s}^{-1} \text{ T}$	fixed
Q	13.5	fixed
fcenter	322.3 MHz	fixed
Mstart	-64.8	3.5
Meq	47.5	1.5
T1	7.4 ms	0.5 ms

5.2.3 Results gallium

Again, Fig. 5.11a we shows the conventional FTs. Here, the inversion field lasted from $t = 1.00$ ms until $t = 1.35$ ms and the Larmor frequency $\tilde{\gamma}B(t)$ crossed the RF field frequency only at around $t = 1.30$ ms.

The intensity after the inversion field is similar to the one before, cf. spectra at $t_{\text{RF}} = 0.81$ ms and $t_{\text{RF}} = 1.36$ ms. The zero-crossing occurs around $t_{\text{RF}} = 1.6$ ms and the maximum frequency offset during excitation was 2.5 MHz. Within the time-window of 4 ms after the inversion, the relaxation process is represented in 21 FIDs. Similar to the aluminum, several of the FIDs are excluded for the fit of $\Omega(t)$ because of their low SNR, cf. Fig. 5.11b and the spectra are calculated accordingly.

Once more, after an individual phase-adjustement (by minimizing the sum of the imaginary part) the intensity I is obtained as the sum of the real part and the values for the first 6 FIDs ($t_{\text{RF}} < 1.6$ ms) are inverted manually. The fit of I to the relaxation model is shown in Fig. 5.12b and the time-dependent M_z of the fit in Fig. 5.12c.

Using the model in combination with the Levenberg-Marquart algorithm a fit is performed. The parameters, as well as error estimates can be found in Tab. 5.4.

Here, the value for T_1 also does not change substantially compared with the margin of

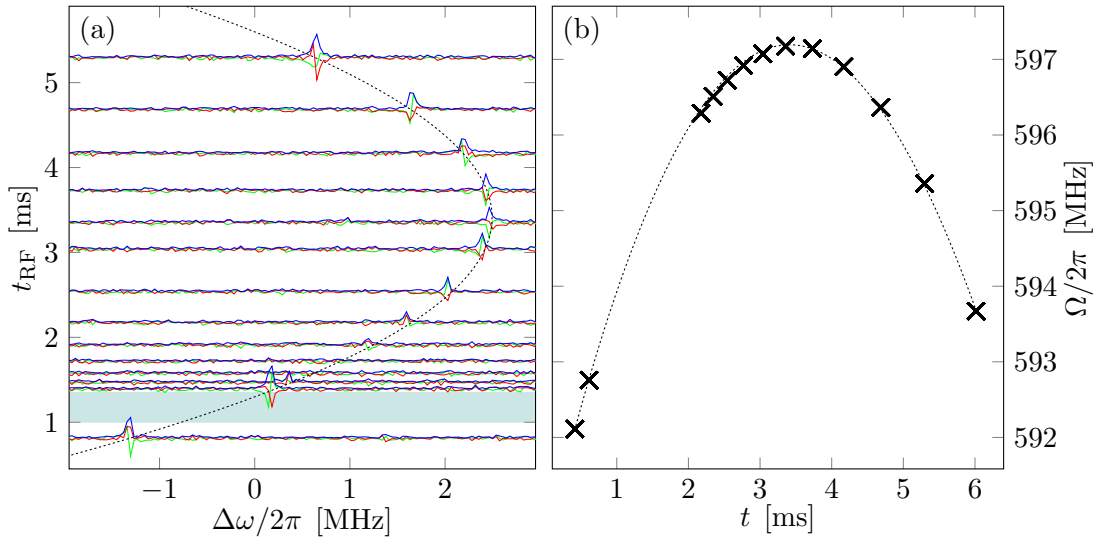


Figure 5.11: (a) Magnitude (blue), real part (red), and imaginary part (green) of the Fourier transformed raw FIDs (only every second FID is shown before $t_{\text{RF}} < 3$ ms) of metallic gallium excited at different times t_{RF} near the field maximum of 58 T in the relaxation measurement with the fitted field profile (dotted black curves). The inversion field was applied from $t = 1.00$ ms to $t = 1.35$ ms (blue shaded area). (b) Fit for $\Omega(t)$ (several FIDs were excluded for the fit because of their low intensity).

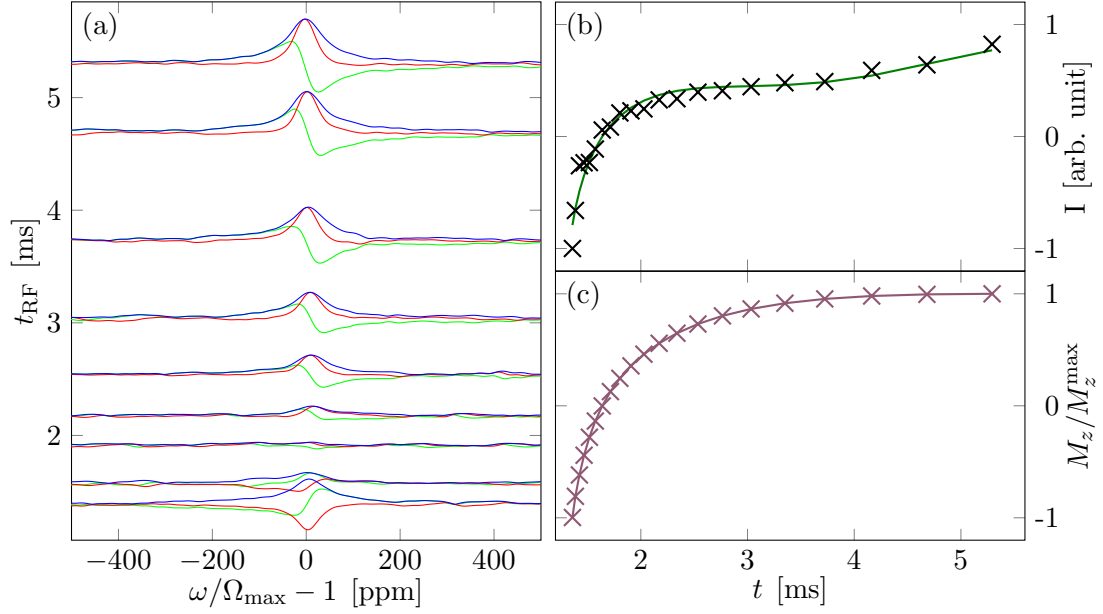


Figure 5.12: (a) Magnitude (blue), real part (red), and imaginary part (green) of Fourier transform with time-dependent base functions after manual phase adjustment (not all spectra are shown) of metallic gallium excited at different times t_{RF} near the field maximum of 58 T. (b) Observed intensities (black symbols) and fit to the model (green curve). (c) Normalized longitudinal magnetization from the fit model.

error if the RF field strength is assumed to be an order of magnitude smaller. Therefore, a value of $T_1 = (585 \pm 160) \mu\text{s}$ (with a 2σ confidence interval) is found and matches the expected $T_1 = 620 \mu\text{s}$.

Table 5.4: Fit parameters for relaxation measurements on metallic aluminum at a temperature of $T = 308 \text{ K}$ and a field of $B \approx 58 \text{ T}$. Parameter names refer to the the Python implementation in Lis. E.2.

parameter	value	error estimate σ
Brf	35 mT	fixed
tau	$0.2 \mu\text{s}$	fixed
gamma	$6.4323 \times 10^7 \text{ rad s}^{-1} \text{ T}$	fixed
Q	30	fixed
fcenter	594.7 MHz	fixed
Mstart	-28.94	9.58
Meq	1.52	0.11
T1	$585 \mu\text{s}$	$80 \mu\text{s}$

CHAPTER 6

Pulsed field NMR of strontium copper borate

Within this chapter, pulsed field NMR of the spin-dimer antiferromagnet $\text{SrCu}_2(\text{BO}_3)_2$ will be presented. The complex physics of this two-dimensional quantum spin system has been of recent interest in the context of frustrated magnetism and detailed overviews of the phenomenology and theory can be found in the literature, e.g., by Takigawa and Mila in Ref. [63] and Ref. [77]. In the following, only a brief description of the system including prior high magnetic field NMR investigations will be given before experimental results on a single crystal will be discussed.

Similar to the shift measurements, frequency-domain filtering and intensity corrections for the determination of the time-dependent relative magnetic field $B(t)/B_{\text{max}}$ and a Fourier transform with time-dependent base functions will be used. Depending on the magnetic field and temperature, simple spectra with three lines (due to the quadrupole splitting) or complex spectra that are spread across ≈ 9 MHz of bandwidth emerge in the case of an underlying electronic spin superstructure. These results have been published in Ref. [56] and were selected as a research highlight by the EMFL [54].

6.1 $\text{SrCu}_2(\text{BO}_3)_2$

Strontium copper borate has a tetragonal unit cell with lattice constants $a = b = 8.995 \text{ \AA}$ and $c = 6.649 \text{ \AA}$ at room temperature and belongs to the $I\bar{4}2m$ space group according to X-ray diffraction [102]. It has a layered structure consisting of planes with interconnected CuO_4 and BO_3 groups and planes composed of Sr^{2+} ions [46]. The crystal structure of the copper-containing plane is shown in the teal box in Fig. 6.1a. Here, the Cu^{2+} ions carry an electron spin $S = 1/2$ that has one nearest-neighbor (2.91 \AA , solid arrows in Fig. 6.1) and four second-nearest-neighbors (5.13 \AA , dashed arrows in Fig. 6.1) [46].

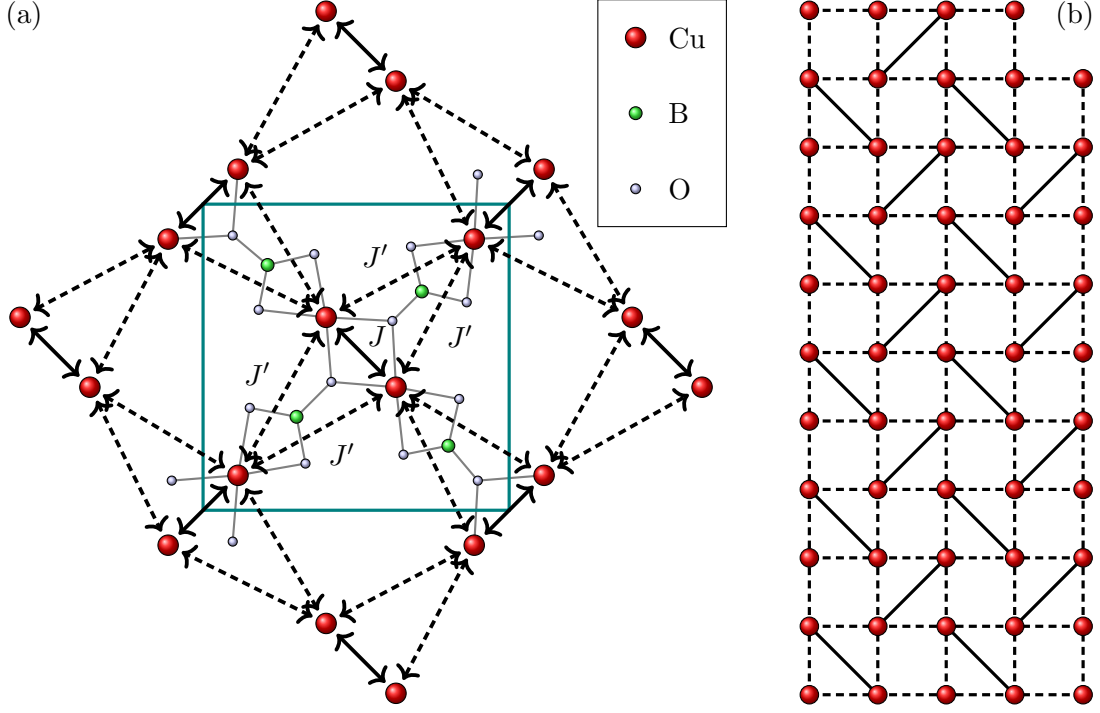


Figure 6.1: (a) Crystal structure of $\text{SrCu}_2(\text{BO}_3)_2$ along the $[100]$ direction and the lattice of Cu^{2+} ions (red balls). The teal box marks the crystallographic unit cell of the plane. (b) Considering interactions only up to second-nearest-neighbors, the interactions are equivalent to the Shastry-Sutherland model (solid and diagonal lines represent the nearest-neighbor interaction with a coupling constant J , dashed lines represent the interaction with second-nearest-neighbors with a coupling constant J').

Neglecting interactions with spins at larger distance, the Hamiltonian with Zeeman interaction (constant b that depends on the applied magnetic field 0) and isotropic exchange interactions between nearest-neighbors (n.n., coupling constant J) and second-nearest neighbors (s.n.n., coupling constant J') becomes

$$\mathcal{H} = J \sum_{\text{n.n.}} \hat{\mathbf{S}}_i \cdot \hat{\mathbf{S}}_j + J' \sum_{\text{s.n.n.}} \hat{\mathbf{S}}_i \cdot \hat{\mathbf{S}}_j + b \sum_i \hat{S}_{iz}. \quad (6.1)$$

An equivalent system was studied in theoretical works on a two-dimensional anisotropic quantum spin Heisenberg Hamiltonian by Shastry and Sutherland in Ref. [100]. In addition to a two dimensional square lattice, they introduced diagonal interactions with a different coupling constant, cf. Fig. 6.1b.

In the limit of a strong interaction between the second-nearest neighbors ($J \ll J'$), only the dashed lines in Fig. 6.1b remain. In this case, the model becomes a two-dimensional

antiferromagnet on a square lattice [63]. In the limit of a dominating nearest-neighbor coupling ($J \gg J'$), only the solid lines in Fig. 6.1b remain, and the ground state is given by a lattice of dimer singlets $|s\rangle$,

$$|s\rangle = \frac{1}{\sqrt{2}} (|\uparrow\downarrow\rangle - |\downarrow\uparrow\rangle), \quad (6.2)$$

and not the triplet states $|t_m\rangle$

$$|t_{-1}\rangle = |\downarrow\downarrow\rangle, \quad (6.3)$$

$$|t_0\rangle = \frac{1}{\sqrt{2}} (|\uparrow\downarrow\rangle + |\downarrow\uparrow\rangle), \quad (6.4)$$

$$|t_1\rangle = |\uparrow\uparrow\rangle. \quad (6.5)$$

In presence of both interactions, however, geometrical frustration emerges since the nearest-neighbor interaction (diagonal lines) favors the two spins to be antiparallel while the interaction along the square lattice favors them to be parallel. Nevertheless, in absence of an external magnetic field (b in Eq. (6.1)), a lattice of dimer singlets $|s\rangle$ remains the ground state of the system up to $J'/J \lesssim 0.7$ [78]. In case of $\text{SrCu}_2(\text{BO}_3)_2$, various techniques have confirmed the singlet groundstate and estimated the exchange parameter J to be in the range of 71 K to 85 K and found a ratio $0.60 \leq J'/J \leq 0.64$ [63].

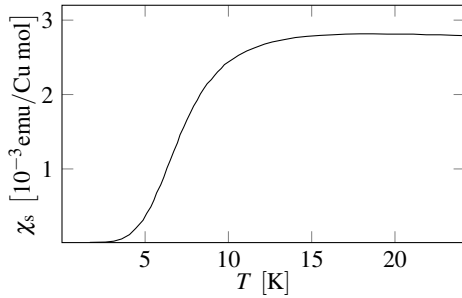


Fig. 6.2: Temperature dependence of the spin susceptibility χ_s (with Curie-Weiss contribution and constant part subtracted) of $\text{SrCu}_2(\text{BO}_3)_2$ at 1.0 T (data reproduced from Ref. [46]).

At low enough temperatures and vanishing or small fields, the singlet groundstate of the system is populated and as a consequence the net magnetization vanishes. By increasing the temperature, the excited triplet states become populated as well and the susceptibility increases, cf. Fig. 6.2.

With increasing external magnetic fields however, the Zeeman term $b \sum_i \hat{S}_{iz}$ in the Hamiltonian from Eq. (6.1) gains importance and can modify the groundstate away from the lattice of

singlet states to one that includes triplet states with a higher contribution from the $|t_1\rangle$ state (spins parallel to the applied field) than from the $|t_{-1}\rangle$ state (spins anti-parallel to the applied field). Therefore, even at low temperatures, the macroscopic magnetization of the system increases, cf. Fig. 6.3 above 20 T.

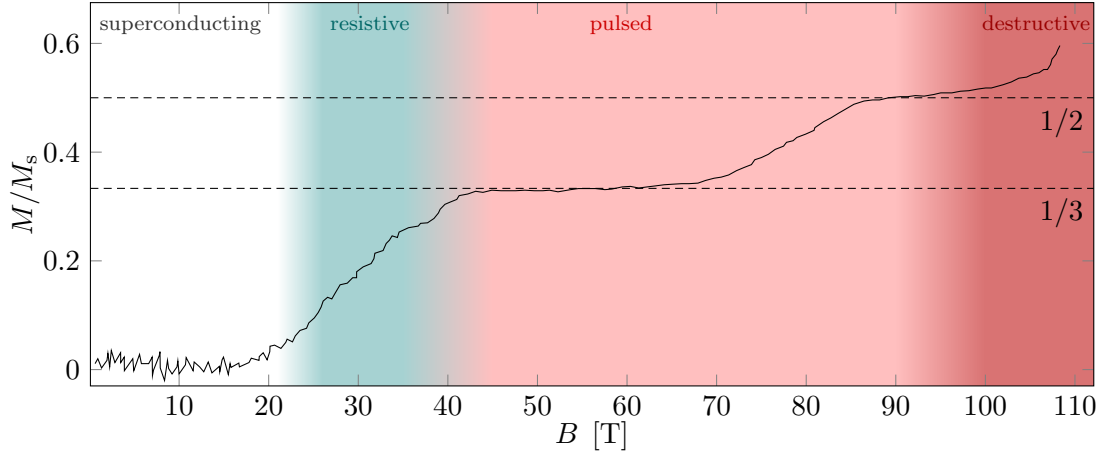


Figure 6.3: Field-dependent magnetization of $\text{SrCu}_2(\text{BO}_3)_2$ for $B \parallel c$ at a temperature of 2.1 K normalized by the saturation magnetization M_s (data reproduced from Ref. [67]). Within certain field ranges, plateaus with a constant magnetization emerge (plateaus of $1/4$ and below are only stable at lower temperatures). Background color illustrates the magnet technology that is needed to produce the field.

At sufficiently high fields, these electronic spins arrange in a lattice. Meaning that $\langle \hat{S}_{iz} \rangle$, the expectation value of the spin operator in the direction of the applied magnetic field of the electronic spin i , becomes periodic for different spins i , albeit with a larger unit cell than the chemical structure of the material.

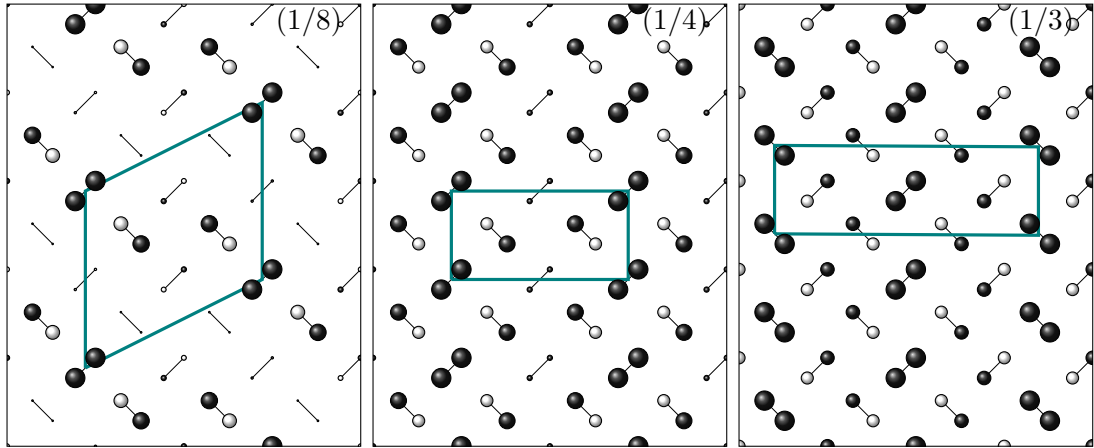


Figure 6.4: Spin superstructure in $\text{SrCu}_2(\text{BO}_3)_2$ in the $1/8$, $1/4$ and $1/3$ plateau [63, 77, 86]. Only the electronic spins i and the dimer bonds are shown (solid lines). The expectation value $\langle \hat{S}_{iz} \rangle$ is represented with symbol size according to magnitude and color according to sign (black: positive, white: negative). The size of the unit cell (teal box) and the number of distinct sites of the electronic spins depends on the plateau.

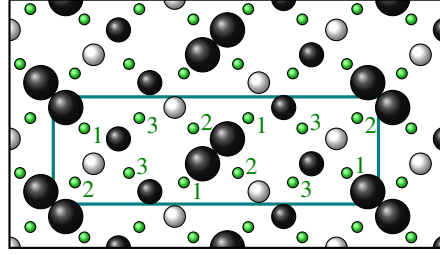


Figure 6.5: The three different ^{11}B crystal sites (green) in the $1/3$ plateau. Additional colors and symbols as in Fig. 6.4.

Among other methods, magnetization measurements in pulsed high-magnetic fields found it to be non-zero and exhibiting a series of plateaus at low temperatures, indicating a transition of the ground state of the material to a lattice of triplet states. In these plateaus, $M(B)$ becomes flat for a certain field range, e.g., from 40 T to 70 T at a temperature of 2.1 K with a value of $1/3$ of the saturation magnetization M_s [67], cf. Fig. 6.3. Each of the plateaus is linked to a specific superstructure of the electron spins at the Cu^{2+} ions with a different number k of distinct crystal sites, see Fig. 6.4. This number k decreases at higher fields but remains constant within a plateau.

The reason for the stability of the plateaus is assumed to be rooted in the strong suppression of the triplet kinetic energy caused by the frustration. As a consequence, the triplet states are highly localized in a stable configuration [78].

Due to the hyperfine coupling of the electronic spins, the emergent superstructure also breaks the symmetry of the boron sites in the material. In case of the $1/3$ plateau, three different positions exist, cf. Fig. 6.5. Note however, that the stacking of the layers along the c axis of the crystal increases the number of distinct sites further, see Supplemental Material B of Ref. [110].

6.2 Prior high field NMR

In order to induce a phase with an electronic spin superstructure, very high magnetic fields and low temperatures are needed. However, a sufficient field strength cannot be generated by superconducting magnets and all prior work with NMR had to be performed in resistive DC magnets. By using temperatures in the mK regime, these were able to give a great insight into the local magnetization.

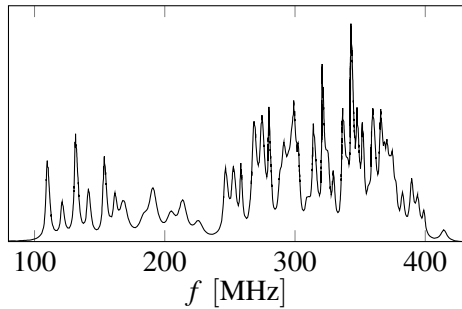


Fig. 6.6: Cu NMR spectra at 27.6 T and 35 mK (fit). Data from Ref. [51].

First successful reports included ^{63}Cu , ^{65}Cu and ^{11}B NMR in the $1/8$ plateau at a temperature of 35 mK [51]. While a field of 26 T only produced simple spectra with six copper lines resulting from an uniform magnetization distribution, the results changed substantially at a field of 27.6 T and proved the presence of the magnetic superstructure. The signals from the copper nuclei became spread over 300 MHz (see Fig. 6.6) while boron was confined to about 6 MHz. Here, the

authors were able to fit the copper spectra in good agreement using a model with 11 distinct sites, each giving six NMR lines due to quadrupole splitting and the two isotopes. In later works, the focus was put on the ^{11}B NMR at higher fields and evidence for other plateaus at $2/15$, $1/6$, $1/4$, and $1/3$ was found [106, 110, 111, 112]. Here, the quadrupole splitting $\omega'_Q/2\pi \approx 1.25$ MHz for $H \parallel c$ is comparable to the distribution of the local magnetic hyperfine fields. Therefore, a deconvolution becomes necessary to obtain the actual distribution.

Later, an advanced method to separate the quadrupole splitting from the local magnetic hyperfine fields was developed by Mila et al. and presented in Ref. [75]: by assuming a uniform quadrupole splitting ω'_Q , the spectra $g(\omega)$ were treated as a sum of the central transition and two frequency shifted satellites with different intensity $1/\alpha$ according to

$$g(\omega) = f(\omega - \omega'_Q) + \alpha f(\omega) + f(\omega + \omega'_Q). \quad (6.6)$$

An elegant rewrite of Eq. (6.6) then yielded an iterative solution that can be used to obtain the actual distribution of local hyperfine fields $f(\omega)$.

Remarkably, as a function of temperature and applied field, a coexistence of two phases producing a superposition of the associated spectra was found, suggesting a discontinuous transition between the normal state and the presence of the magnetic superstructure [111].

6.3 Experimental

In the following, pulsed magnetic field experiments aimed at the acquisition of ^{11}B spectra in the $1/3$ plateau will be described.

The experiments were performed on a single crystal of $\text{SrCu}_2(\text{BO}_3)_2$ with a mass of 19 mg and dimensions of $5\text{ mm} \times 1.5\text{ mm} \times 1.5\text{ mm}$ with the c axis along one of the 1.5 mm edges. The growth process of the samples is described in Ref. [15]. The sample was placed in a solenoid RF coil (8 turns, diameter 1.8 mm) with the c axis parallel to the applied main magnetic field ($B \parallel c$) which was produced by a $KS3$ coil that gives about 5 ms of observation time at its field maximum of 63 T, cf. Ch. 3.

The sample temperature was set by a bath cryostat and was measured with a calibrated Cernox sensor. A liquid helium bath was used for the 4.2 K (cryostat at atmospheric pressure) and 2 K (low pressure using a vacuum pump) measurements. At the higher temperatures $T > 100\text{ K}$, however, no cryogenic liquid was used in the cryostat and measurements were only started after temperatures stabilized. Note, however, that the $\text{SrCu}_2(\text{BO}_3)_2$ is known to show a strong magnetocaloric effect [63], i.e., the actual sample temperature is likely to be lowered during the experiment.

The FIDs were excited using 200 ns RF pulses with a repetition time of 0.5 ms at a constant carrier frequency that was equal to the resonance frequency of the probe head at the given temperature (based on reflected power). With an applied RF power level of about 50 W, quality factors $Q \approx 90$, and the coil geometry, the estimated flip angle is about 10° for on-resonance excitation (less than 2 % loss of longitudinal magnetization). The traces were recorded with a sampling rate of 10 MHz.

Table 6.1: Experimental parameters in the $\text{SrCu}_2(\text{BO}_3)_2$ measurements (maximum field B_0 , temperature T , carrier frequency ω_0 , and charging voltage $U_{\text{capacitors}}$). The carrier frequency was set according to the resonance frequency of the tank circuit before the field pulse based on the reflected power.

field B_0	T	$\omega_0/2\pi$	$U_{\text{capacitors}}$	experiment
42 T	193 K	573 MHz	14.58 kV	2014-11-14-00
	4.2 K	566 MHz	14.40 kV	2014-11-14-01
	2.0 K	566 MHz	14.40 kV	2014-11-14-02
46 T	117 K	634 MHz	16.18 kV	2014-11-17-01
	4.2 K	627 MHz	16.00 kV	2014-11-17-04
	2.0 K	624 MHz	16.01 kV	2014-11-17-03
54 T	119 K	741 MHz	19.12 kV	2014-11-13-00
	4.2 K	734 MHz	18.90 kV	2014-11-11-04
	2.0 K	734 MHz	18.97 kV	2014-11-12-04

6.4 Results

In the following, results from measurements at three different fields of about 42 T, 46 T, and 54 T each with three different temperatures will be discussed. Since the necessary steps in the reconstruction of spectra only differ significantly between the high-temperature phase and the low-temperature phase at a high field with an electronic spin superlattice, an extensive description will only be given for the 119 K and 2.0 K measurements at 54 T.

Fig. 6.7 shows the conventional Fourier transform of the FIDs for the 54 T series. At the highest temperature of 119 K, the material is in the paramagnetic state without the signature of an electronic spin superlattice with two STs around the CT, all showing the time dependence of the magnetic field (dashed lines). At low temperatures (4.2 K and 2.0 K) however, the spectra show a plethora of constituents that are spread over

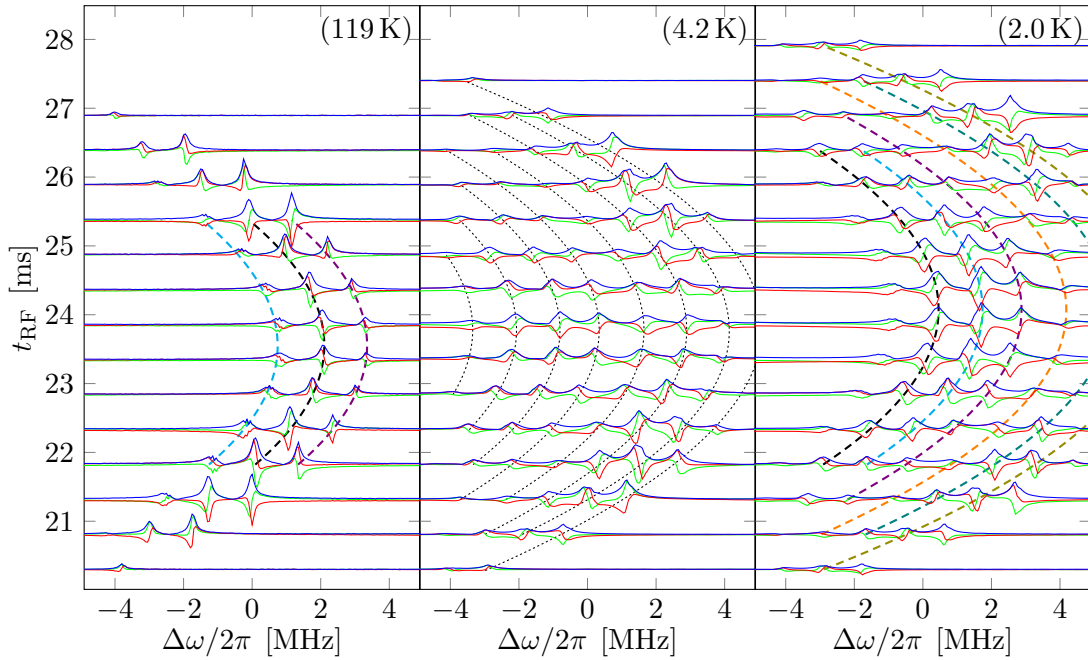


Figure 6.7: Magnitude (blue), real part (red), and imaginary part (green) of the Fourier transformed raw ^{11}B FIDs of a single crystal $\text{SrCu}_2(\text{BO}_3)_2$ sample at about 54 T in three field pulses (traces without signal are not shown). The signals were acquired at different temperatures and slightly different carrier frequencies: 119 K and 741 MHz, 4.2 K and 734 MHz, 2.0 K and 734 MHz. Spectra at 4.2 K are scaled by a factor of 0.5. Dotted curves are guides to the eye showing the frequency modulation due to the time dependence of the magnetic field, dashed curves according to the fits that are shown in Fig. 6.8 and Fig. 6.13 (same colors).

several MHz. In the measurement at 2.0 K, the intensities appear to be shifted to higher frequencies.

6.4.1 High-temperature paramagnetic phase (119 K)

Now, the reconstruction of spectra in the high-temperature paramagnetic state at 119 K will be discussed. As described in Ch. 4, fits for all three transitions are performed using rectangular frequency domain filters to isolated single components of the total signal. For this, the time dependence of the magnetic field is estimated as a parabolic curve, i.e., each transition in Fig. 6.7 (119 K) is identified manually based on the sequence of spectra calculated with the conventional Fourier transform. In the time frame 21.7 ms to 25.5 ms, all three remained within the bandwidth of detection of the spectrometer.

The resulting $\Omega(t)$ are shown in Fig. 6.8a. As expected for the quadrupole splitting, their maxima are shifted by ≈ 1.3 MHz. The normalized $\Omega(t)/\Omega_{\max}$ are almost identical and the used field range is only $\lesssim 0.3\%$, cf. Fig. 6.8b. Furthermore, the inaccuracies of the three fits lead to expected differences of $\lesssim 10$ kHz in the calculation of the spectra, cf. Fig. 6.8c. After applying the intensity correction filter $h(\Delta\omega)$, the spectra $Y_k(\omega)$ are calculated according to Eq. (4.48), cf. Fig. 6.9.1a. In order to combine them, the iterative procedure introduced in Ch. 4 is used to determine the proper phase offset for each one, cf. Fig. 6.9.2a. The combined spectrum then covers a broader frequency range and has a

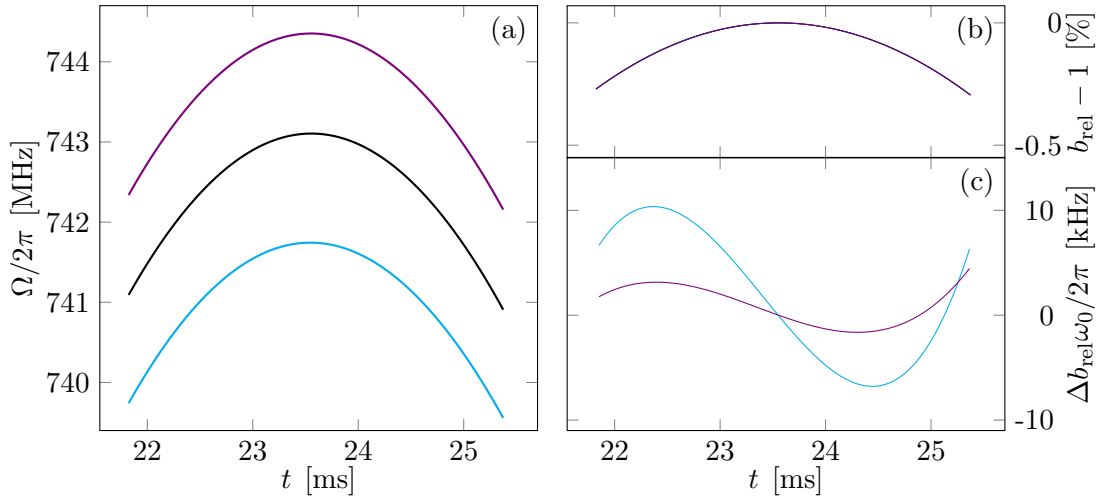


Figure 6.8: (a) Polynomial fit $\Omega(t)$ of the time-dependent frequency for the CT (black), lower ST (cyan), and upper ST (violet). (b) Difference of the normalized frequency $b_{\text{rel}}(t) = \Omega(t)/\Omega_{\max}$ relative to the maximum in % (all three curves overlap almost perfectly). (c) Expected shifts in calculated spectra due to differences $b_{\text{rel}}^i(t) - b_{\text{rel}}^{\text{CT}}(t)$ of the field fits from the STs i relative to the one based on the CT.

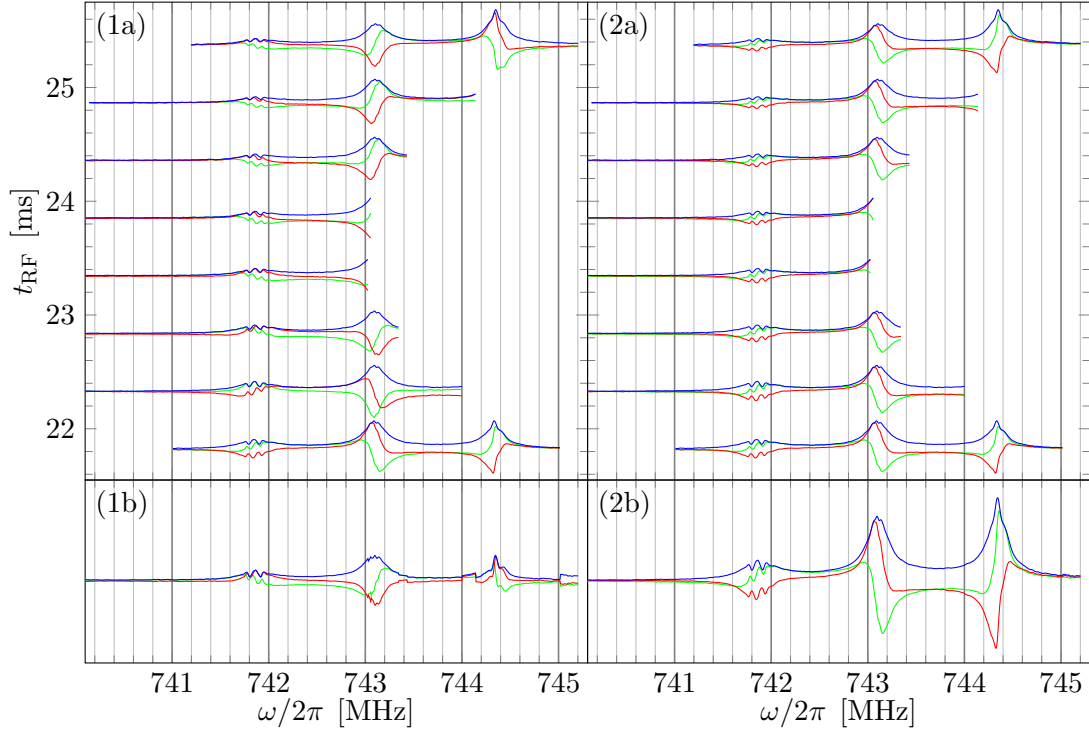


Figure 6.9: ^{11}B NMR spectra of $\text{SrCu}_2(\text{BO}_3)_2$ at 54 T and 119 K. Magnitude (blue), real part (red), and imaginary part (green) of $Y_k(\omega)$ based on $\Omega(t)$ from the CT for each FID k according to Eq. (4.48) without phase adjustment (1a) and with phase adjusted using the iterative procedure described in Ch. 4 (2a). The combined spectra Y^c for both sets are shown in the bottom (1b and 2b, same y scale).

higher SNR in case of overlap, cf. Fig. 6.9.2b.

The remaining phase modulation is clearly visible in $Y^c(\omega)$ in Fig. 6.9.2b. While the real part of the CT is almost in phase, it appears inverted in case of the STs. Therefore, the manual linear phase correction is performed to obtain $Y(\omega)$ according to Eq. (4.56), with the results shown in Fig. 6.10a. Here, the linear term $2\pi\zeta_1 = 2.7 \text{ rad MHz}^{-1} \approx \pi/1.25 \text{ rad MHz}^{-1}$ is in good agreement with the inversion for the STs that have an expected offset of $\approx 1.25 \text{ MHz}$. Note that this value corresponds to the signal delay from about 90 m of *RG-58* coaxial cable and is thus within the expected range since it still includes phase shifts from the off-resonance excitation and detection as well as the spectrometer electronics.

Using the fit for $\Omega(t)$ based on the STs, the steps are repeated, and almost identical results are found, cf. Fig. 6.10a and Fig. 6.10b. The spectra show a quadrupole splitting of $\omega'_Q/2\pi = (1.24 \pm 0.04) \text{ MHz}$ based on the CT and the upper ST in good agreement

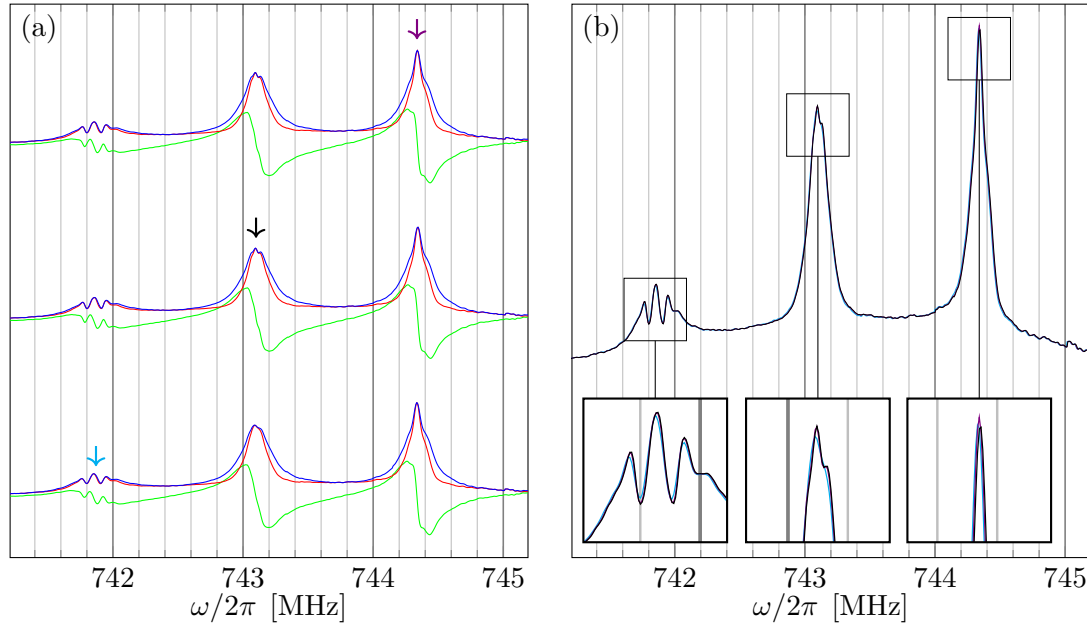


Figure 6.10: ^{11}B NMR spectra of $\text{SrCu}_2(\text{BO}_3)_2$ at 54 T and 119 K. (a) Magnitude (blue), real (red), and imaginary part (green) of the phase-corrected combined $Y(\omega)$ based on fit of $\Omega(t)$ from the lower ST, CT and the upper ST (in that order, also indicated with arrows) after a manual linear phase adjustment. (b) Real part of all three calculated spectra (colors mark which fit was used).

with the expected value [52, 112].

It is apparent from the additional fine structure of the lower ST compared with the upper ST, that the spectral shapes of the STs are different. Since the local EFG and magnetic hyperfine shift tensor depends on the ^{11}B site in the crystallographic unit cell [52], the symmetry of the STs can be broken by a misorientation of the crystallographic c -axis relative to the magnetic field. Test measurements in a highly homogeneous superconducting magnet on the same sample at a field of 6.3 T showed a similar effect in the case of a misorientation of a few degrees [132].

Note that the linewidth of the CT at $\omega/2\pi = 734.1$ MHz is 17 times larger than in low field measurements at about 86 MHz on the same sample [132]. This broadening is likely due to the significant field inhomogeneity over the sample volume.

6.4.2 Low-temperature paramagnetic phase with a superstructure (2 K)

We continue with the discussion of the measurements at 2 K. During the experiments, the power level of the reflected RF pulse increased substantially above a certain magnetic field, consistent with a field-induced detuning of the tank circuit.

Furthermore, a shift of the intensities towards higher frequency offsets can already be seen in the conventional Fourier transform spectra in Fig. 6.7c. This systematic, frequency-dependent, alteration of the intensities becomes even more clear in Fig. 6.11a that shows the normalized intensities of three spectral maxima as a function of their offset. Note that these three peaks were chosen because of the frequency offsets in different FIDs. To remove the effect of the excitation conditions, the intensities are divided by the small angle excitation envelope of a rectangular RF pulse with a duration of τ to obtain

$$I_{\text{sinc}}(\Delta\omega) = \frac{I(\Delta\omega)}{\text{sinc}(\Delta\omega\tau/2\pi)}. \quad (6.7)$$

As can be seen in Fig. 6.11, these still grow towards higher frequency offsets. In order to compensate for this systematic modification of the signal intensities, another digital filter $g(\Delta\omega)$ that is given by the inverse of a Lorentzian curve fit to $I_{\text{sinc}}(\Delta\omega)$ is introduced. Note that while this fit produces estimates for the resonance frequency and the bandwidth of the resonator, these are not reliable for determining the properties of the resonator since the input data only covered one shoulder of the Lorentzian curve. However, these quantities are not needed for the reconstruction of spectra.

Again, we manually estimate the time dependence of the

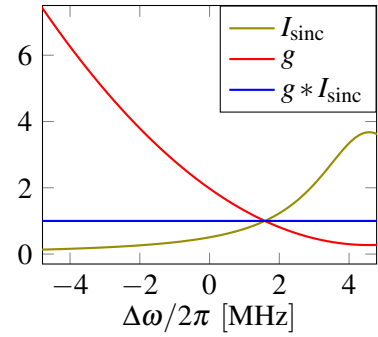


Fig. 6.12: Digital filter $g(\Delta\omega)$ to compensate for the intensity modification I_{sinc} due to the detuned resonator.

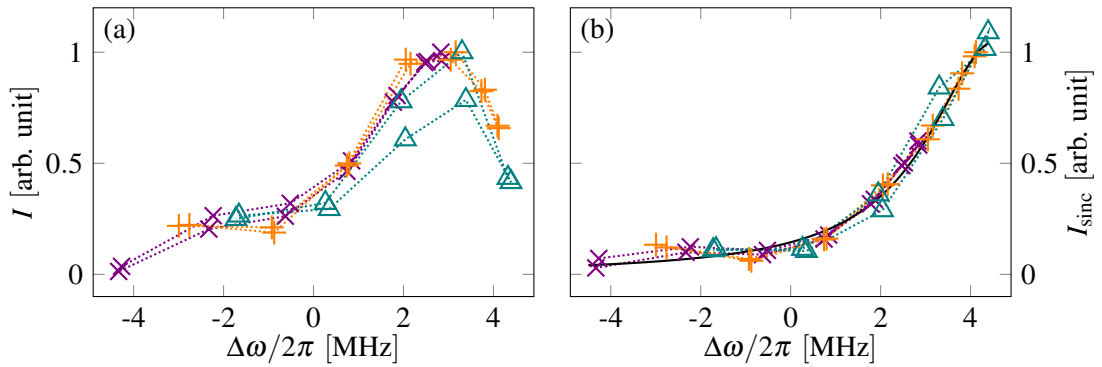


Figure 6.11: (a) Normalized signal intensities at 54 T and 2 K as a function of the frequency offset $\Delta\omega$. Three different lines are shown (same colors as in Fig. 6.7 and Fig. 6.13). (b) Intensities divided by the small angle excitation envelope (I_{sinc}). They are well-described by the shoulder of a Lorentzian curve (black curve) and consistent with a detuned tank circuit.

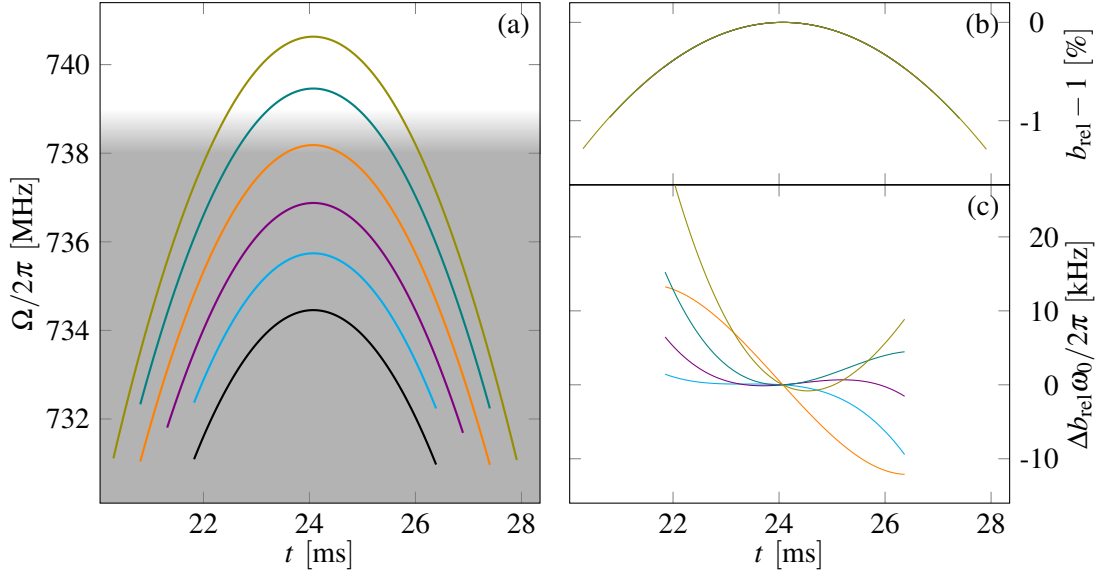


Figure 6.13: (a) Polynomial fit $\Omega(t)$ of the time-dependent frequency for six different spectral maxima. The gray area marks the bandwidth of detection of the spectrometer. (b) Difference of the normalized frequency $b_{\text{rel}}(t) = \Omega(t)/\Omega_{\text{max}}$ relative to the maximum in % (all curves overlap almost perfectly). (c) Expected shifts in calculated spectra due to differences in $\Omega(t)$ relative to the one based on the black curve.

magnetic field and apply rectangular frequency filters accordingly to extract $\Omega(t)$ for several spectral maxima and show the results in Fig. 6.13. Here, we find only slightly larger differences $\Delta b_{\text{rel}} \omega_0$ compared with the measurement at 119 K.

Based on the fits, the spectra $Y_k(\omega)$ are calculated after applying the filter $g(\Delta\omega)$ together with the filter for the off-resonance excitation $h(\Delta\omega)$, cf. Fig. 4.1. The reconstructed spectrum shown in Fig. 6.14.2b is spread over 9 MHz and shows eight distinctive spectral maxima that are presumably produced by several overlapping transitions due to the quadrupole splitting.

In the manual phase correction, a 20 % smaller value of $2\pi\zeta_1 = 2.2 \text{ rad MHz}^{-1}$ is found compared to the measurement at 119 K. A decreased value of ζ_1 is in agreement with a detuned tank circuit during the detection of the NMR signal where the phase shift $\Delta\alpha$ relative to the onresonance detection approaches a value of $-\pi/2$ asymptotically for frequencies well below the bandwidth of the resonator, see Fig. 4.6 and Eq. (4.29). Thus, within this regime, the off-resonance detection does not produce a phase modulation anymore.

Fig. 6.15 shows the spectra $Y(\omega)$ calculated for the six different $\Omega(t)$. They are very similar and only show slight differences at higher values of ω . In addition, there is an

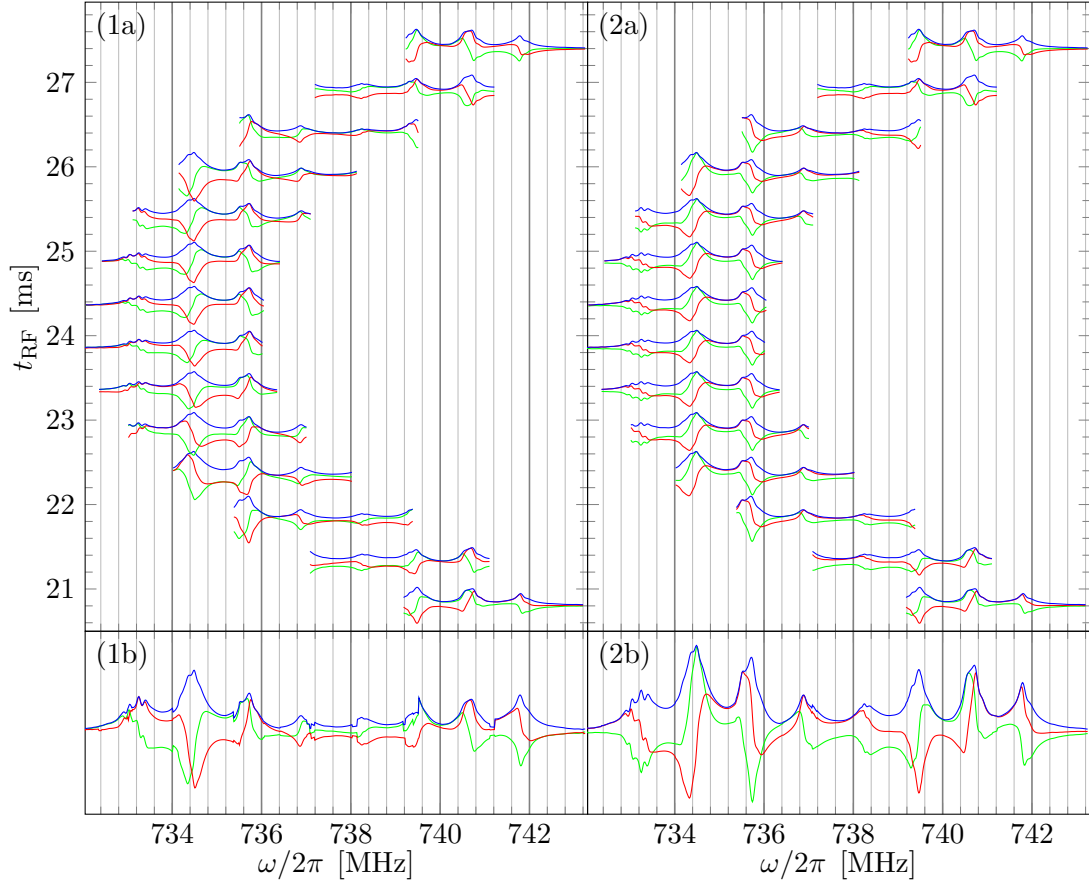


Figure 6.14: ^{11}B NMR spectra of $\text{SrCu}_2(\text{BO}_3)_2$ at 54 T and 2 K. Magnitude (blue), real part (red), and imaginary part (green) of spectra Y_k based on fit from the CT for each FID k according to Eq. (4.48) without phase adjustment (1a) and with phase adjusted using the iterative procedure described in Ch. 4 (2a). The combined spectra Y^c for both sets are shown in the bottom (1b and 2b, same y scale).

inversion of the phase with unknown origin between 736 MHz and 739 MHz.

Based on frequency dependence of the argument of $Y(\omega)$ (shown in Fig. 6.16a), an additional naïve phase correction (shown in Fig. 6.16b) is performed according to

$$\bar{Y}(\omega) = Y(\omega) \exp[i\zeta_L(\omega)], \quad (6.8)$$

$$\zeta_L(\omega) = \frac{\pi w^2}{(\omega - c)^2 + w^2}. \quad (6.9)$$

This phase correction then produces an almost properly phased spectrum, see Fig. 6.16c. In order to demonstrate the necessity to compensate for the systematic intensity variation towards higher frequencies, Fig. 6.17 shows the resulting spectrum calculated once with

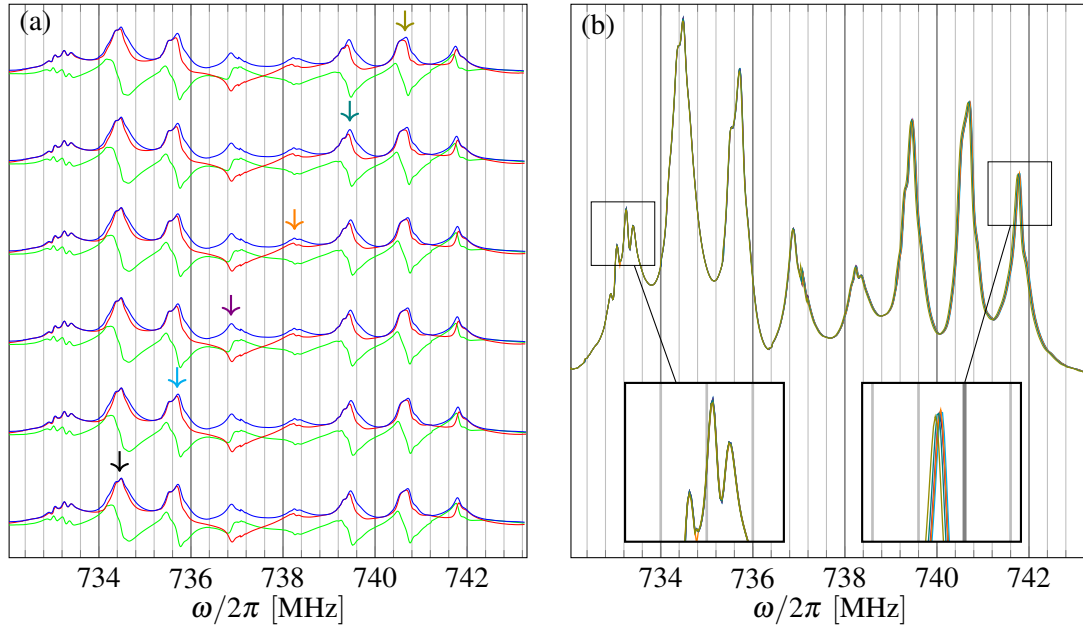


Figure 6.15: ^{11}B NMR spectra of $\text{SrCu}_2(\text{BO}_3)_2$ at 54 T and 2 K. (a) Magnitude (blue), real (red), and imaginary part (green) of the phase-corrected and combined $Y(\omega)$ based on the fit of $\Omega(t)$ from six different spectral maxima (indicated with arrows) after a manual linear phase adjustment. (b) Magnitude of all six calculated spectra (colors mark which fit was used).

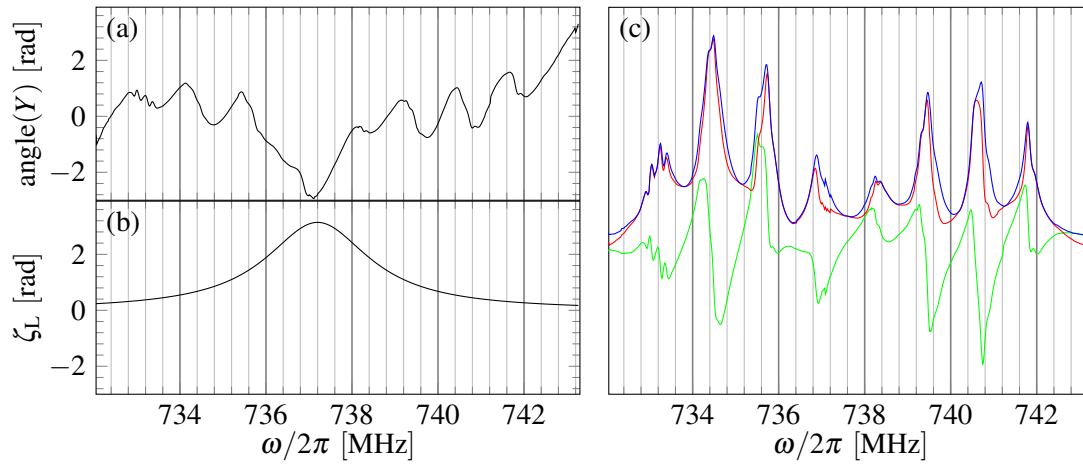


Figure 6.16: (a) Angle of $Y(\omega)$. (b) $\zeta_L(\omega)$ with $c = 737.2$ MHz and $w = 1.467$ MHz. (c) $\tilde{Y}(\omega)$. Magnitude (blue), real part (red), and imaginary part (green) of the phase-corrected and combined $Y(\omega)$.

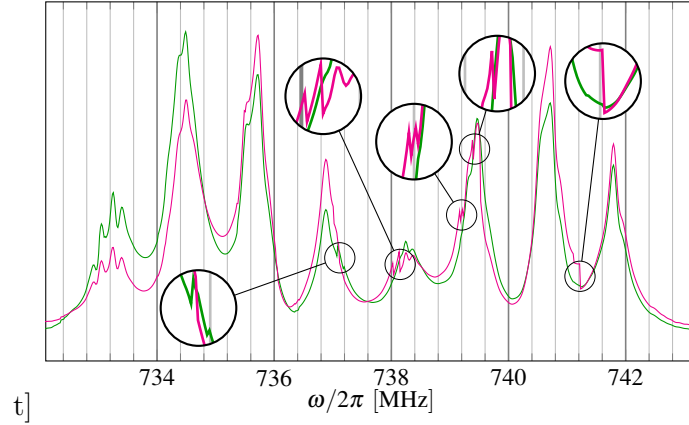


Figure 6.17: ^{11}B NMR spectra of $\text{SrCu}_2(\text{BO}_3)_2$ at 54 T and 2 K calculated with intensity correction filter $g(\Delta\omega)$ (green) and without it (magenta).

$g(\Delta\omega)$ and once without $g(\Delta\omega)$. Since the observed intensity originating from a narrow part of the spectrum depends strongly on $\Delta\omega$ during the experiment, the associated spectra $Y_k(\omega)$ are affected by amplitude modifications as well. Not taking this effect into account then produces combined spectra $Y(\omega)$ that show a decreased intensity for those spectral regions that were only observed at lower values of $\Delta\omega$. While this does not have to correspond to the lower values of ω in $Y_k(\omega)$ and $Y(\omega)$ in general, it does in this experiment. For example, the spectral maximum marked with a black arrow in Fig. 6.15a and the black curve in Fig. 6.13a only reaches $\Delta\omega \approx 0.4$ MHz and is thus only recorded with lower intensity, cf. Fig. 6.11. As a consequence, the combined spectrum $Y(\omega)$ can then show discontinuities at the cutoff frequencies ω_j^\pm (enlarged parts in Fig. 6.17).

6.4.3 Comparison with DC field measurements

While most work on ^{11}B NMR of $\text{SrCu}_2(\text{BO}_3)_2$ in DC fields [51, 110, 111, 112] was limited to fields that only induced superstructures belonging to plateaus lower than the $1/3$ at mK temperatures, Ref. [106] reported field-stepped spectra with a $1/3$ superstructure at 2 K and fields of around 41 T. Similiar to the calculation of the spectra, the mapping of $Y(\omega)$ onto a field scale is not trivial due to the field-dependent and field-independent interactions. Neglecting the latter, $B = \omega_{\text{ref}}^2 / \gamma\omega^{-1}$ can be used for the conversion, cf. Fig. 6.18. While the spectra are very similar, the one acquired in the pulsed high-magnetic field shows broader lines and a slightly larger spread. However, the field difference in between 54 T and 41 T is quite substantial with the latter one being just in the beginning of the $1/3$ plateau, cf. Fig. 6.3.

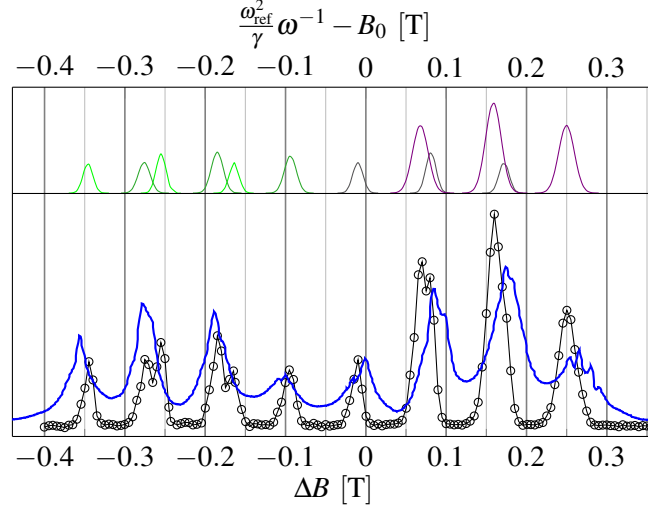


Figure 6.18: ^{11}B NMR spectra of $\text{SrCu}_2(\text{BO}_3)_2$ at 2 K in presence of the 1/3 superlattice. Black curve and symbols were acquired at DC fields of around 41 T and fits (reproduced from Ref. [106]). Blue curve is the magnitude of the spectra from Fig. 6.14.2b plotted as a function of $\omega_{\text{ref}}^2/\gamma\omega^{-1} - B_0$ with $\omega_{\text{ref}}^2/(2\pi\gamma) = 3.597 \times 10^4 \text{ MHz T}$ and $B_0 = 53.7 \text{ T}$ (top x scale).

6.4.4 Spectra at 46 T and 42 T

While the reconstruction of ^{11}B spectra of $\text{SrCu}_2(\text{BO}_3)_2$ in the two different phases at 54 T were discussed in detail, we now consider the measurements at a lower field of 46 T. Fig. 6.19 shows the conventional FT spectra during field pulses at three different sample temperatures.

In case of the 117 K and the 4.2 K measurements, only simple spectra similar to the ones at 119 K and 54 T in Fig. 6.7a are found. At 2 K however, the spectra are more complicated and change significantly between before the field maximum at $t_{\text{RF}} \approx 23.8 \text{ ms}$ and after with additional resonance lines appearing, e.g., for $0 \text{ MHz} \leq \Delta\omega \leq 2 \text{ MHz}$ at $t_{\text{RF}} \approx 28.4 \text{ ms}$.

The cause for the change is difficult to identify with certainty. While the dynamics of the phase transition might be able to distort the spectra at earlier times (e.g., by a superlattice that is not pinned on the time scale given by the Larmor precession), an incomplete longitudinal magnetization due to a long nuclear T_1 would do so as well. Especially in the case of a non-uniform T_1 that depends on the ^{11}B site within the superstructure of the 1/3 plateau, understanding the resulting spectra becomes a complicated endeavor that would require a new set of dedicated experiments, i.e., at slightly different fields and temperatures.

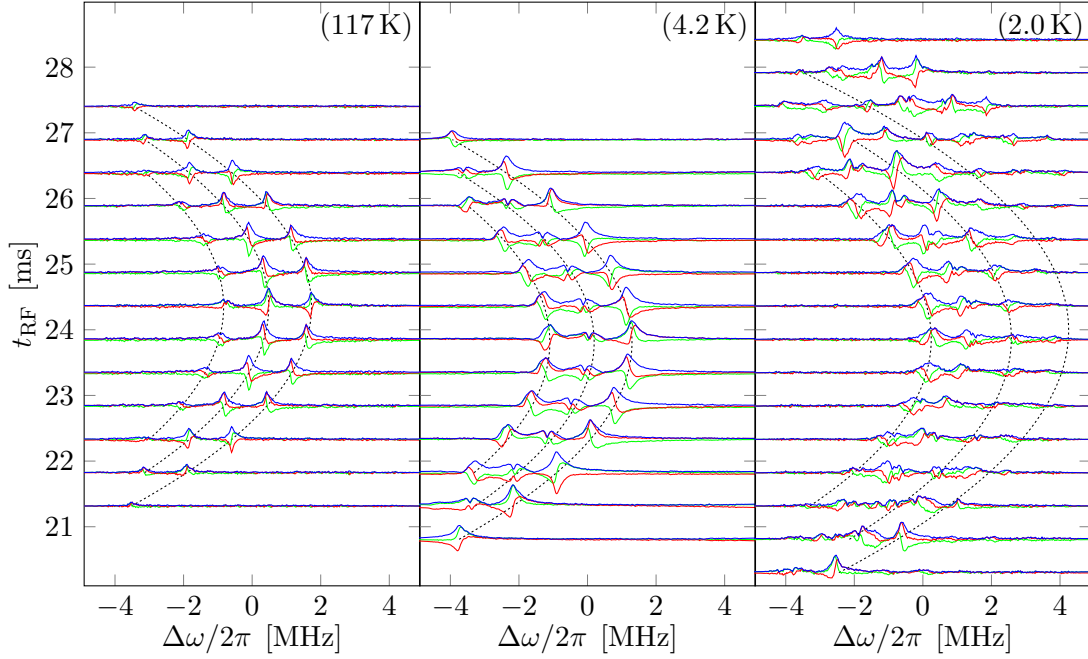


Figure 6.19: Magnitude (blue), real (red), and imaginary part (green) of the Fourier transformed raw ^{11}B FIDs of a single crystal $\text{SrCu}_2(\text{BO}_3)_2$ sample at about 46 T in three field pulses (traces without signal are not shown). The signals were acquired at different temperatures and slightly different carrier frequencies: 117 K and 634 MHz (a), 4.2 K and 627 MHz (b), 2.0 K and 624 MHz (c). Spectra at 4.2 K are scaled by a factor of 0.5. Dotted curves are guides to the eye showing modulation due to the time dependence of the magnetic field.

Under these circumstances, however, no reliable fit of $\Omega(t)$ to determine the time-dependence of the relative magnetic field can be performed and the reconstruction of the spectrum just from the acquired data is not possible.

At an even lower field of about 42 T however, no signature of an underlying superstructure was observed at any temperature, cf. Fig. 6.20.

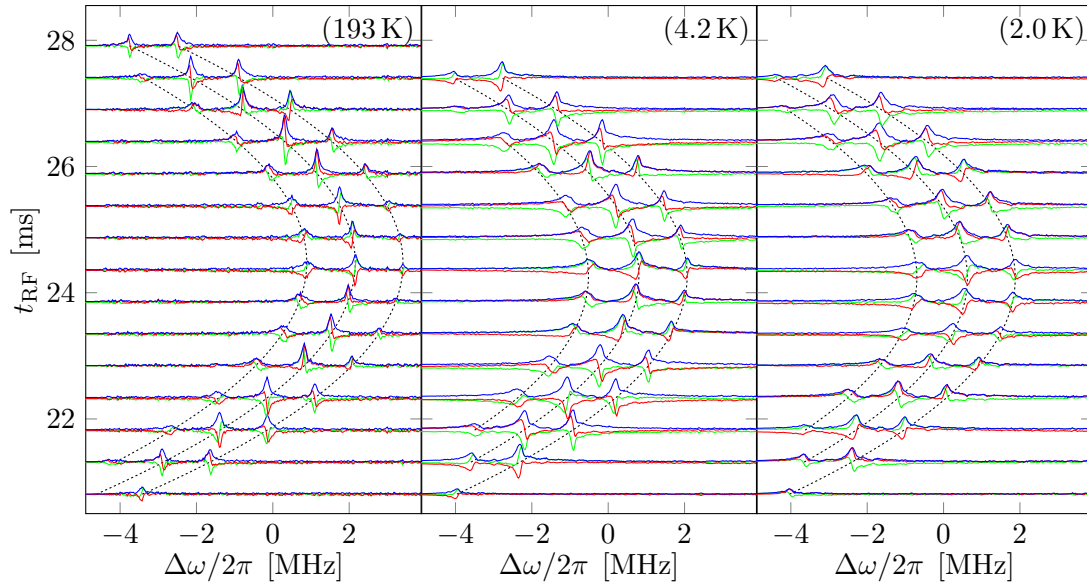


Figure 6.20: Magnitude (blue), real (red), and imaginary part (green) of the Fourier transformed raw ^{11}B FIDs of a single crystal $\text{SrCu}_2(\text{BO}_3)_2$ sample at about 42 T in three field pulses (traces without signal are not shown). The signals were acquired at different temperatures and slightly different carrier frequencies: 193 K and 573 MHz (a), 4.2 K and 566 MHz (b), 2.0 K and 566 MHz (c). Spectra at 4.2 K and 2.0 K are scaled by a factor of 0.5. Dotted curves are guides to the eye showing modulation due to the time dependence of the magnetic field.

CHAPTER 7

Electronic spin susceptibilities in cuprates

In this chapter, temperature-dependent ^{63}Cu shift measurements for different doping levels δ of the cuprate high-temperature superconductor $\text{HgBa}_2\text{CuO}_{4+\delta}$ will be presented. The described experiments were conducted together with D. Rybicki and the analysis was developed and performed by the author of this thesis under the guidance of J. Haase.

By comparing two different orientations and four doping levels, it becomes apparent that the data cannot be explained with the prevalent model using a single isotropic spin susceptibility. Instead a universal pseudogap component, a Fermi liquid-like component (only present at higher doping levels and constant above T_c), and an additional third component (carrying the temperature-dependent anisotropy) are identified. These results were published in Ref. [95].

7.1 High-temperature superconductivity in the cuprates

Superconductivity in $\text{La}_{5-x}\text{Ba}_x\text{Cu}_5\text{O}_{5(3-y)}$ was reported by J. G. Bednorz and K. A. Müller in 1986 [8] and awarded the Nobel Price in Physics in 1987. Soon after, additional superconducting compounds belonging to the class of cuprates were found, and investigations into the electronic properties of these materials with NMR commenced.

Common to all cuprates is the layered, perovskite-type, structure with copper-oxygen planes that are separated by charge reservoir layers. These materials share a common electronic phase diagram which includes antiferromagnetism, a pseudogap phase, and superconductivity depending on temperature and doping and can be divided into two groups that have different doping mechanisms. Here, research into the *hole*-doped cuprates is far more prevalent than into the *electron*-doped ones.

It is believed, that the copper-oxygen planes are the structural element carrying the

superconducting currents. However, despite the discovery of superconductivity in the cuprates almost 30 years ago, the underlying mechanisms and the normal state electronic properties remain enigmatic.

7.2 $\text{HgBa}_2\text{CuO}_{4+\delta}$

The cuprate $\text{HgBa}_2\text{CuO}_{4+\delta}$ has a single CuO_2 layer per unit cell and a high transition temperature into the superconducting state of $T_c = 97\text{ K}$ at optimal doping. It has a tetragonal unit cell with $a = b = 3.878\text{ \AA}$ and $c = 9.509\text{ \AA}$ and belongs to the space group $P4/mmm$ [91]. In addition to the oxygen in the CuO_2 plane, the structure incorporates an additional oxygen site O(2) inbetween the Cu and Hg atom that is fully occupied as well as O(3) that only is filled upon doping the material via a higher oxygen concentration δ [119], see Fig. 7.1a.

The CuO_2 plane is nominally formed by Cu^{2+} and O^{2-} ions with $3d_{x^2-y^2}$ and $2p_\sigma$ bonding orbitals respectively. Here, one hole is contained in the $3d_{x^2-y^2}$ orbital in the undoped parent material, and, upon doping, the hole contents of both orbitals change [97]. The relationship of the doping p and the chemical composition δ , however, is more complicated and often only T_c and p are used when discussing different samples. Similar to other cuprates, the phase diagram has an antiferromagnetic phase at low doping levels and

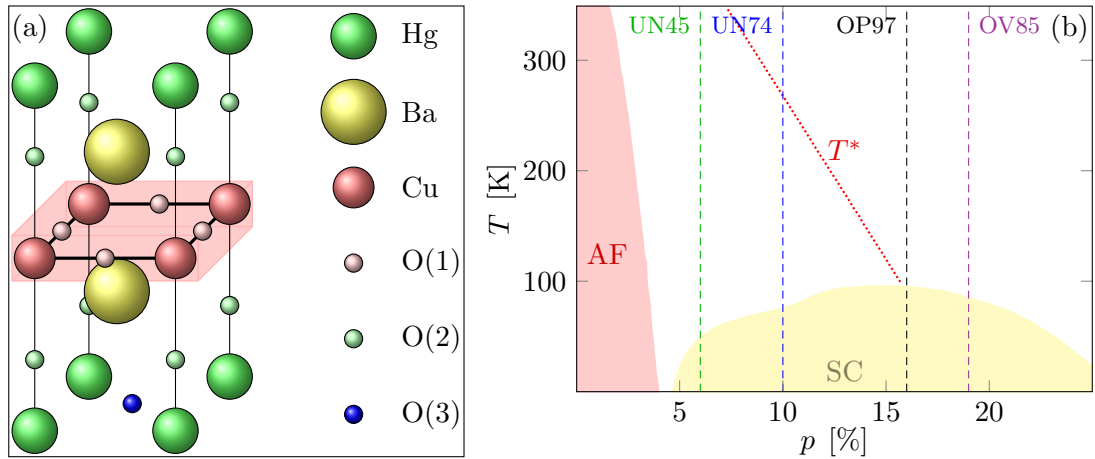


Figure 7.1: (a) Crystal structure of $\text{HgBa}_2\text{CuO}_{4+\delta}$ according to Ref. [91]. The shaded red box marks the cuprate copper-oxygen plane. Additional oxygen atoms at O(3) (in the mercury plane) change the doping δ of the material. (b) Doping-dependent phase diagram of $\text{HgBa}_2\text{CuO}_{4+\delta}$ with antiferromagnetic phase (AF) and superconducting phase (SC) according to Ref. [4]. The dotted line shows the doping dependence of the pseudogap temperature T^* . Dashed vertical lines show doping levels of studied samples (same colors as in following figures).

only becomes superconducting at $p \approx 5\%$. For the superconducting samples, T_c depends approximately parabolic on p and reaches its maximum at $p \approx 0.16$, cf. Fig. 7.1b.

Samples with different doping levels have been investigated with NMR using the ^{17}O , ^{63}Cu , and ^{199}Hg nuclei [79, 94, 95, 96].

7.3 NMR of cuprates and electronic spin susceptibility

NMR was extensively used to study cuprates [120]. A concise description of the interpretation of the NMR spectra and relaxation by C. P. Slichter can be found in Ref. [99].

Since most of the nuclei under study in cuprates have a spin $I > 1/2$ the Hamiltonian describing the nuclear spin system has to take the quadrupolar interaction into account (note that the large splittings in the case of ^{63}Cu and ^{65}Cu often require a treatment with second order perturbations to the Zeeman Hamiltonian).

The spin susceptibility of conduction band electrons give rise to a Knight shift that can be used to study the electronic properties of the materials. In the cuprates, the characteristic CuO_2 planes have unpaired electrons in the $3d_{x^2-y^2}$ orbitals of the copper atoms and the $2p_x/2p_y$ orbitals of the oxygen atoms. Therefore, in case of ^{63}Cu and ^{17}O , one would naïvely assume to find Knight shifts of

$$^{63}K_S = \frac{A}{\gamma_e \gamma_{63} \hbar^2} \chi_d, \quad (7.1)$$

$$^{17}K_S = \frac{C_p}{\gamma_e \gamma_{17} \hbar^2} \chi_p. \quad (7.2)$$

Here, χ_d and χ_p are the susceptibilities of two electron species at Cu^{2+} and O^{2-} that are coupled with constants A and C_p . These constants describe the spatial overlap of the Bloch wave functions and the nuclei, cf. Sect. 2.4. In general, the temperature dependences of χ_d and χ_p could be different.

Based on Cu NMR shift and T_1 data, a description using a spin singlet state was proposed by Mila, Rice and Zhang [74, 131]. Here, the electron spin of the oxygen is paired to the electron spin from the copper atom to form the so-called *Zang-Rice singlet*. In this model, only a single spin fluid exists and the resulting Knight shifts of different sites share a common temperature dependence due to the associated susceptibility χ_{ZR} [99]. With the applied magnetic field along the z -direction, including coupling constants A , B and

C , they are then given by

$${}^{63}K_S = \frac{A + 4B}{\gamma_e \gamma_{63} \hbar^2} \chi_{ZR}, \quad (7.3)$$

$${}^{17}K_S = \frac{2C}{\gamma_e \gamma_{17} \hbar^2} \chi_{ZR}. \quad (7.4)$$

The prefactor 4 in Eq. (7.3) arises from the number of neighboring copper atoms (linked by oxygen atoms) for each ${}^{63}\text{Cu}$ nucleus, and, similarly, 2 in Eq. (7.4) for the two copper atoms at opposing sides of each ${}^{17}\text{O}$ nucleus.

Then, the temperature-dependent shifts of the nuclei in the CuO_2 planes are all governed by a single isotropic electronic spin susceptibility and show the same evolution as a function of temperature apart from a scaling factor given by the hyperfine coupling constant and a constant orbital shift. While this was found in measurements on $\text{YBa}_2\text{Cu}_3\text{O}_{6.63}$ powder [3, 113], measurements on another cuprate, $\text{La}_{2-x}\text{Sr}_x\text{CuO}_4$, revealed that such a description does not apply to all cuprates [33, 34].

Note that in the case of $\text{YBa}_2\text{Cu}_3\text{O}_{6+y}$, an accidental cancellation, meaning $A + 4B \approx 0$ in Eq. (7.3), gives a convenient explanation for the temperature-independent Knight shift above T_c if the magnetic field is applied perpendicular to the copper-oxygen planes and parallel to the c -direction, cf. Fig. 7.1.

While the electronic spin susceptibility $\chi_S(T)$ can be measured using NMR, measurements of the macroscopic susceptibility $\chi(T)$ are a more direct probe. Multiple experimental methods exist to measure $\chi(T)$ [83]. Due to the need for sufficient sample mass, most early measurements on cuprates were performed on powder samples only.

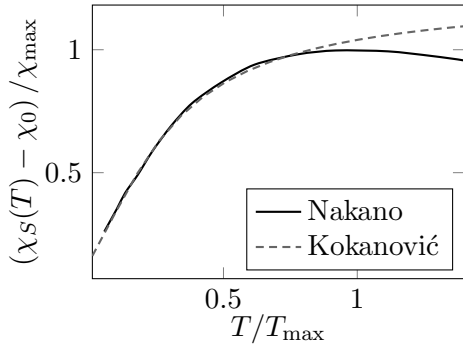


Fig. 7.2: Universal spin susceptibility in cuprates as observed by Nakano et al. [80] and for a V-shaped DOS after Kokanović et al. [57, 65].

Surprisingly, a number of different systems ($\text{Bi}_2\text{Sr}_{3-y}\text{Ca}_{y-x}\text{Cu}_2\text{O}_8$ and $(\text{La}_{1-x}\text{M}_x)_2\text{CuO}_4$ with $\text{M} = \text{Sr}, \text{Ba}$), each for different doping levels, showed a universal temperature-dependence for $\chi_S(T)$ [6, 44, 80, 84], i.e., $\chi_S(T)$ is described by a common function, cf. Fig. 7.2,

$$F(T/T_{\max}) = (\chi_S(T) - \chi_0) / \chi_{\max} \quad (7.5)$$

after subtracting a sample-dependent constant value χ_0 followed by a rescaling of temperature and amplitude. The continuous change of $\chi_S(T)$ is

attributed to the cuprate *pseudogap* [98, 114], the exact origin of this behaviour, however,

remains an open question [118].

The presence of a Fermi liquid (with a constant susceptibility above T_c) that is responsible for superconductivity in addition to an insulating spin liquid that causes the *pseudogap* was proposed by Barzykin and Pines [6]. Contributions that match the expected temperature dependences of the associated susceptibilities were identified in NMR experiments by Ohsugi et al. [85] and by Haase et al. by investigating different systems, nuclei, sample orientations, and samples under high pressure [33, 34, 73].

While the anisotropy of NMR shifts was usually attributed to orientation-dependent hyperfine coupling constants, the spin susceptibility itself was assumed to be isotropic. However, with the availability of larger crystals, susceptibility measurements on single crystals became possible and this assumption was cast into doubt [42, 57, 123]. Here, depending on the doping level, clear deviations for different sample orientations were found.

On top of the experimental properties like macroscopic susceptibility, Knight shift, and T_1 relaxation, a deeper understanding of the physics of the electronic system of the cuprates involves the Fermi surface. Starting from the two-dimensional layered structure of the parent material, the volume of the first Brillouin zone of the hole states is decreased by a factor of two due to the anti-ferromagnetism that doubles the effective size of the unit cell. This smaller Brillouin zone leads to a reconstruction of the Fermi surface at the edges that produces hole pockets and electron pockets [20], cf. Fig. 7.3. Upon doping, the density of holes increases and defects are introduced to the antiferromagnetic spin

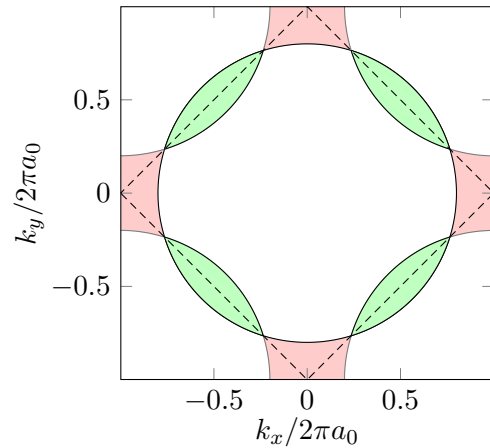


Fig. 7.3: Fermi surface of a cuprate parent material. The anti-ferromagnetism reduces the size of the first Brillouin zone (dashed square) and produces a reconstruction of the Fermi surface that produces hole pockets (green) and electron pockets (red).

structure that, as a consequence, is weakened. The weakening is reflected in the phase diagram (see Fig. 7.1b) by the decrease of the Néel temperature that marks the transition from an antiferromagnetic material to a paramagnetic material. Then, at high doping levels, the Fermi surface resembles that of a metal, i.e., it is more circular since no reconstruction occurs. A more detailed review on the electronic structure based on *Angle-resolved photoemission* measurements in different cuprate families can be found in

Ref. [17].

The presence of additional *charge-stripe order*, different from simple antiferromagnetism, was debated earlier [50, 116], but regained attention recently [14, 109, 127].

7.4 Experimental

The investigations were performed on two single crystal samples with different transition temperatures $T_c = 45$ K (underdoped) and $T_c = 85$ K (overdoped). Furthermore, data from two additional samples from Ref. [36] was used in the analysis. The sample preparation is described in Refs. [5, 133]. Based on the transition temperatures of the samples, the doping levels are estimated. The sample parameters are summarized in Tab. 7.1.

A 11.75 T magnet with a cryostat insert and a homebuilt NMR probe was used together with a *Tecmag Apollo* spectrometer. Frequency stepped measurements using a simple spin echo sequence with a $\pi/2$ and a π pulse for the studied transition were performed. Spectra were then obtained using the echo intensity as a function of the excitation frequency.

Table 7.1: Parameters of the four investigated $\text{HgBa}_2\text{CuO}_{4+\delta}$ samples with different transition temperatures T_c and associated doping levels p .

sample	UN45	UN74	OP97	OV85
	underdoped	underdoped	optimally doped	overdoped
T_c	45 K	74 K	97 K	85 K
p	0.06 ± 0.01	0.10 ± 0.01	0.16 ± 0.02	0.19 ± 0.01

7.5 Results and discussion

We start with a short discussion of the observed temperature-dependent shifts before a numerical analysis based on three distinct susceptibility components will be presented.

The performed analysis is sketched in Fig. 7.4. By comparing the shifts from two different orientations and four different samples, a scaling behavior is found and it becomes apparent that the data cannot be explained with the prevalent model using a single isotropic spin susceptibility (red boxes). Instead two components $q_\eta\chi(T)$ and $q_{\kappa,\eta}\chi_\kappa(T)$, with different hyperfine constants, are needed. Using a decomposition procedure, they are separated. Then, justified by the observed scaling behavior, a further decomposition into a universal pseudogap component $q_\eta\chi_{\text{PG}}(T)$ and a Fermi liquid-like component $q_\eta\chi_{\text{FL}}(T)$ is performed. While the pseudogap component is present in all samples, the Fermi liquid-like component (constant above T_c) is only present at higher doping levels. The additional third component $q_{\kappa,\eta}\chi_\kappa(T)$ carries the temperature-dependent anisotropy and vanishes in the optimally doped sample.

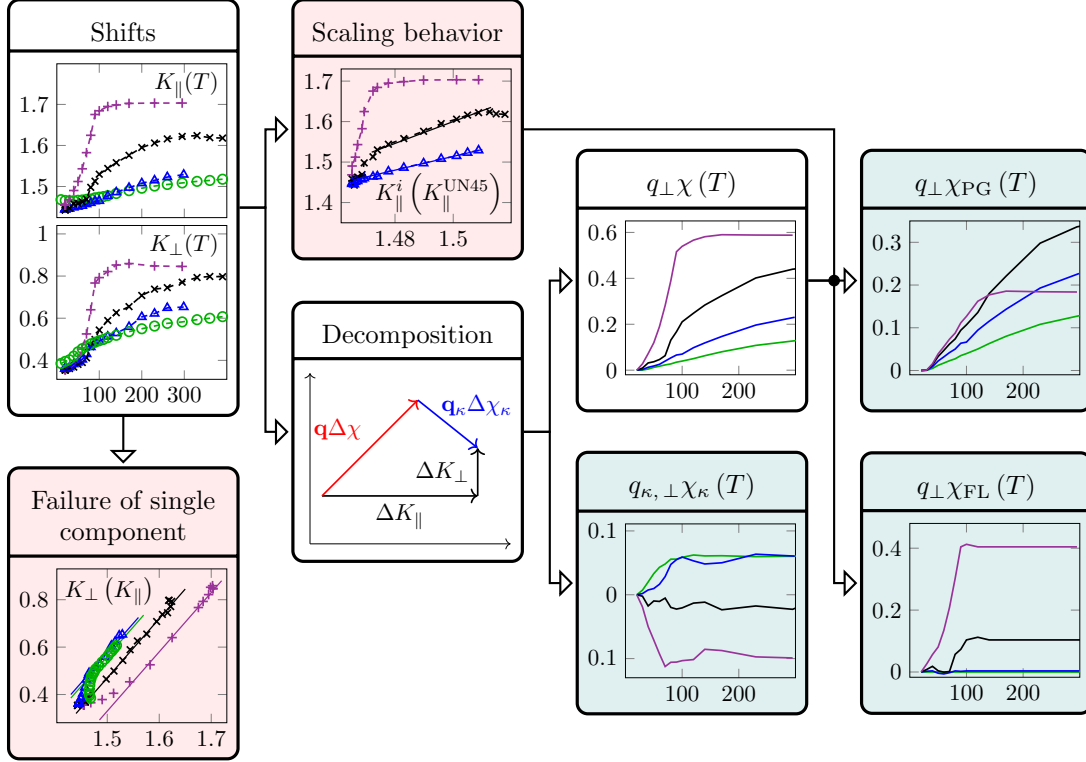


Figure 7.4: Shift analysis for $\text{HgBa}_2\text{CuO}_{4+\delta}$ (details in text).

7.5.1 Temperature-dependent shifts

Fig. 7.5a and Fig. 7.5b show the shift values K_{η} as a function of temperature with the external magnetic field parallel ($c \parallel \mathbf{B}$, $\eta = ||$) and perpendicular ($c \perp \mathbf{B}$, $\eta = \perp$) to the c -axis of the sample after the second order quadrupole shifts have been removed.

Note that these values still contain the temperature-independent orbital shifts $K_{L,\eta}$. Similar to $\text{La}_{2-x}\text{Sr}_x\text{CuO}_4$ [93], these values appear to be doping-independent since the measured shift values converge to common, only orientation-dependent, constants,

$$K_{L,||} \approx 1.44 \%, \quad (7.6)$$

$$K_{L,\perp} \approx 0.34 \%. \quad (7.7)$$

Starting from low temperatures, the underdoped samples show a very smooth increase of the shift without any noticeable signature around the transition temperature T_c . However, the optimally doped and especially the overdoped sample show a clearly visible jump just below their transition temperature, independent of the sample orientation.

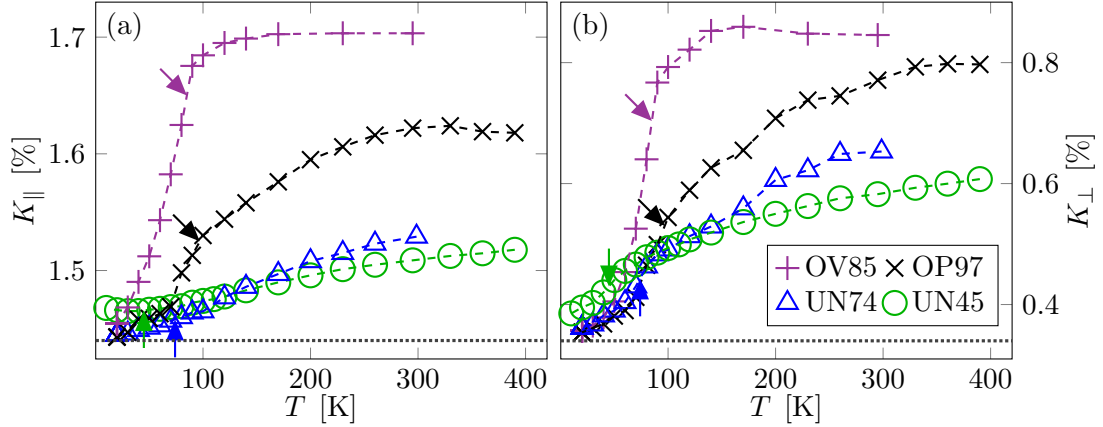


Figure 7.5: ^{63}Cu NMR shifts in $\text{HgBa}_2\text{CuO}_{4+\delta}$ samples for parallel (K_{\parallel} , left) and perpendicular (K_{\perp} , right) orientation as a function of temperature at 11.75 T (based on the central transition with second order quadrupole contribution removed). Arrows indicate T_c , dashed lines are a guide to the eye, dotted gray lines are estimates for $K_{L,\eta}$.

Fig. 7.6a shows K_{\parallel} as a function of K_{\perp} with the temperature as implicit parameter. At high temperatures (large shift values), the changes in shifts in both orientations appear to be proportional (indicated by straight lines) with a common slope of $dK_{\perp}/dK_{\parallel} \approx 2.5 = 1/c_0$. Towards low temperatures, however, a deviation from this proportionality occurs for the overdoped and the underdoped samples.

This deviation is emphasized as $\kappa(T)$ in Fig. 7.6b (after subtracting $K_{L,\parallel}$ and $K_{L,\perp}$)

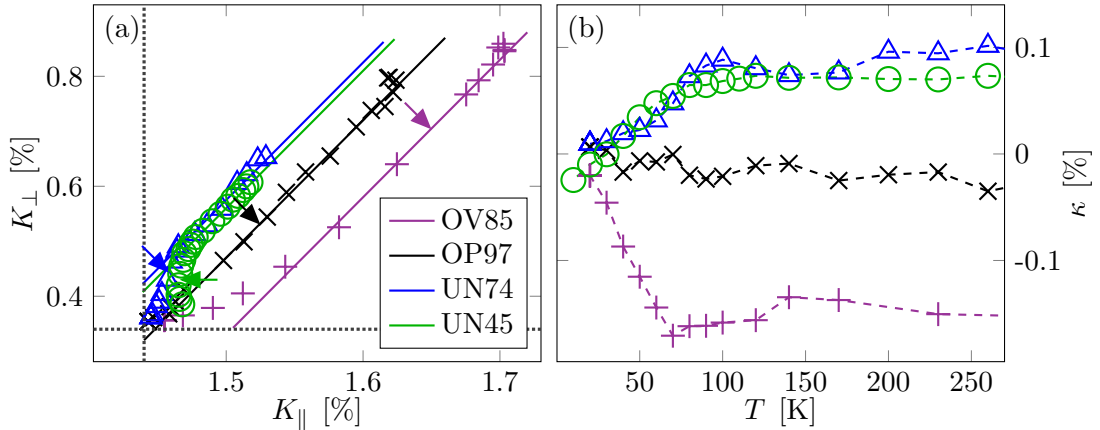


Figure 7.6: (a) $K_{\perp}(T)$ as a function of $K_{\parallel}(T)$ with the temperature as implicit parameter. Solid curves are straight lines with a slope of $dK_{\perp}/dK_{\parallel} = 2.5$. Arrows indicate T_c , dotted gray lines are estimates for $K_{L,\eta}$. (b) $\kappa(T)$ showing the deviation from proportional changes for both orientations.

using

$$\kappa(T) = K_{S\parallel}(T) - K_{S\perp}(T)/c_0. \quad (7.8)$$

While $\kappa(T)$ vanishes for the optimally doped sample (OP97), the underdoped samples (UN45 and UN74) show very similar curves with opposing sign compared with the overdoped sample (OV85). In all cases, $\kappa(T)$ becomes constant above a certain temperature ((80 ± 10) K for UN45 and UN74, (60 ± 10) K for OV85) and does not have any characteristic signature around T_c .

Fig. 7.7 shows the shifts K_η of three of the samples as a function of the shifts of the UN45 sample for both orientations with the temperature as implicit parameter. In case of the $i = \text{UN74}$ and the $i = \text{OP97}$ sample, above a certain temperature, the changes in shift $dK_\eta^i = K_\eta^i(T_2) - K_\eta^i(T_1)$ are well described by a proportional dependence on the changes in shift $K_\eta^{\text{UN45}} = K_\eta^{\text{UN45}}(T_2) - K_\eta^{\text{UN45}}(T_1)$ of the UN45 sample for two temperatures,

$$dK_\eta^i = x \cdot dK_\eta^{\text{UN45}}, \quad (7.9)$$

$$\text{with } x = p^i/p^{\text{UN45}}, \quad (7.10)$$

where the proportionality factor appears to be given by the ratio of the doping values p^i/p^{UN45} relative to the UN45 sample.

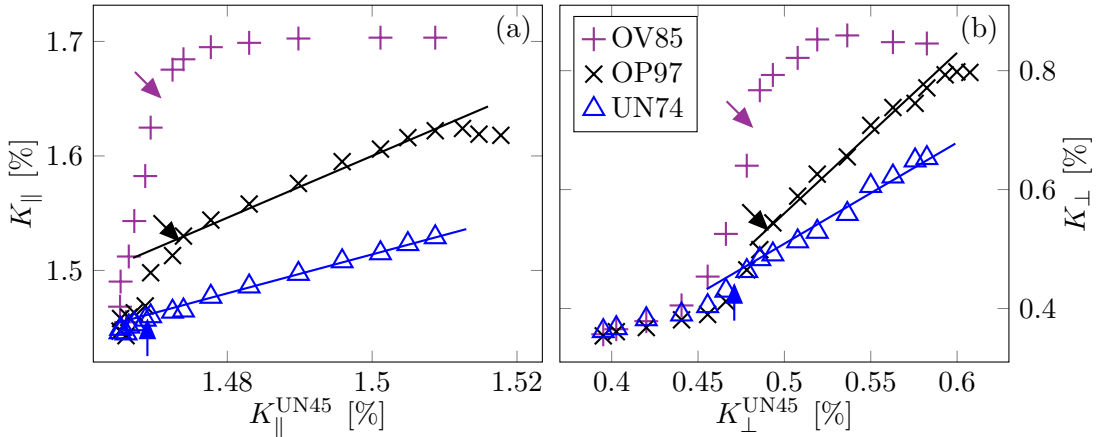


Figure 7.7: ^{63}Cu NMR shifts of the UN74, OP97, and OV85 samples for parallel orientation (a) and perpendicular orientation (b) as a function of the corresponding shifts of the UN45 sample with the temperature as implicit parameter (based on the central transition with second order quadrupole contribution removed). Arrows indicate T_c , solid lines are guides to the eye with slopes p^i/p^{UN45} based on doping levels.

7.5.2 Decomposition into shift components

The prevalent interpretation of cuprates assumes isotropic spin susceptibilities from the mobile charge carriers [40]. However, this does not apply to the associated Knight shifts from NMR measurements due to the orientation dependence of the hyperfine coupling constants q_η , cf. Sect. 2.4. Since q_η only depends on the probability density of the electronic wave function at the site of the nucleus, i.e., a high energy property, it is expected to be independent of temperature.

In the case of a single spin liquid, e.g., the widely accepted *Zang-Rice singlet* states, this would produce orientation-dependent NMR shifts of

$$K_\eta(T) = q_\eta \chi(T) + K_{L,\eta}. \quad (7.11)$$

Substituting $\chi(T)$ in Eq. (7.11) for $\eta = \parallel$ and $\eta = \perp$ then yields

$$K_\perp(T) = \frac{q_\perp}{q_\parallel} (K_\parallel(T) - K_{L,\parallel}) + K_{L,\perp}. \quad (7.12)$$

Therefore, the dependence of K_\perp on K_\parallel described by Eq. (7.12) is in contradiction with the observed shifts, cf. Fig. 7.6, where such a behavior was only found for the optimally doped OP97 sample. Consequently, a multi-component approach is necessary to explain the data. Introducing an additional susceptibility χ_κ that is coupled to the nuclear spins through orientation-dependent hyperfine coefficients $q_{\kappa,\eta}$ and constant at higher temperatures $T \gtrsim 80$ K, Eq. (7.11) is replaced by

$$K_\eta(T) = q_\eta \chi(T) + q_{\kappa,\eta} \chi_\kappa(T) + K_{L,\eta}. \quad (7.13)$$

Based on Eq. (7.13), the changes in the shift $\Delta K_\eta = K_\eta(T_2) - K_\eta(T_1)$ between any two temperatures $T_2 > T_1$ can be written using the change in susceptibility $\Delta\chi = \chi(T_2) - \chi(T_1)$ and $\Delta\chi_\kappa = \chi_\kappa(T_2) - \chi_\kappa(T_1)$,

$$\Delta K_\parallel = q_\parallel \Delta\chi + q_{\kappa,\parallel} \Delta\chi_\kappa, \quad (7.14)$$

$$\Delta K_\perp = q_\perp \Delta\chi + q_{\kappa,\perp} \Delta\chi_\kappa. \quad (7.15)$$

In principle, the system given by Eqs. (7.14) and (7.15) could be solved for $\Delta\chi$ and $\Delta\chi_\kappa$ as long as all q_η and $q_{\kappa,\eta}$ were known. While macroscopic susceptibility measurements might be used above T_c for the exact determination of q_η , solving for the changes in shift $q_\eta \Delta\chi$ and $q_{\kappa,\eta} \Delta\chi_\kappa$ only requires knowledge of the ratios q_\parallel/q_\perp and $q_{\kappa,\parallel}/q_{\kappa,\perp}$.

Assuming the ratios of the hyperfine coefficients for the different orientations were known, the task of extracting $q_\eta \Delta\chi$ and $q_{\kappa,\eta} \Delta\chi_\kappa$ can be understood as a vector decomposition, cf. Fig. 7.8, onto a basis of two vectors,

$$\mathbf{q} = \begin{pmatrix} q_\parallel \\ q_\perp \end{pmatrix}, \quad (7.16)$$

$$\mathbf{q}_\kappa = \begin{pmatrix} q_{\kappa,\parallel} \\ q_{\kappa,\perp} \end{pmatrix}, \quad (7.17)$$

that, in general, are neither normalized nor orthogonal. As long as \mathbf{q} and \mathbf{q}_κ are linearly independent, i.e., $q_\parallel/q_\perp \neq q_{\kappa,\parallel}/q_{\kappa,\perp}$, a solution exists,

$$q_\parallel \Delta\chi = \frac{\Delta K_\parallel - \frac{q_{\kappa,\parallel}}{q_{\kappa,\perp}} \Delta K_\perp}{1 - \frac{q_\perp}{q_\parallel} \frac{q_{\kappa,\parallel}}{q_{\kappa,\perp}}}, \quad (7.18)$$

$$q_\perp \Delta\chi = \frac{q_\perp}{q_\parallel} (q_\parallel \Delta\chi), \quad (7.19)$$

$$q_{\kappa,\parallel} \Delta\chi_\kappa = \frac{\Delta K_{S\parallel} - \frac{q_\parallel}{q_\perp} \Delta K_\perp}{1 - \frac{q_{\kappa,\perp}}{q_{\kappa,\parallel}} \frac{q_\parallel}{q_\perp}}, \quad (7.20)$$

$$q_{\kappa,\perp} \Delta\chi_\kappa = \frac{q_{\kappa,\perp}}{q_{\kappa,\parallel}} q_{\kappa,\parallel} \Delta\chi_\kappa. \quad (7.21)$$

Starting from the lowest temperature T_{\min} at which the shifts were measured, the changes in the shift relative to T_{\min} due to $q_\eta \Delta\chi$ and $q_{\kappa,\eta} \Delta\chi_\kappa$ can be obtained. Furthermore, assuming vanishing susceptibilities at T_{\min} , the temperature-dependent shift contributions

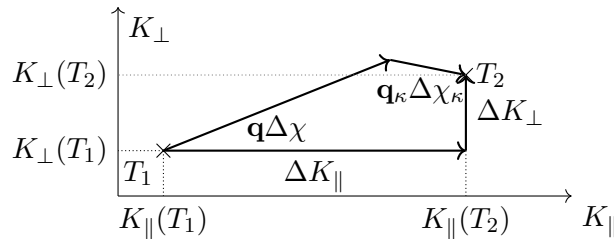


Figure 7.8: Geometric interpretation of Eqs. (7.14) and (7.15). The changes of the shift values for both orientations can be understood as the addition of two vectors \mathbf{q} and \mathbf{q}_κ (multiplied by a change in the associated susceptibility) with different directions.

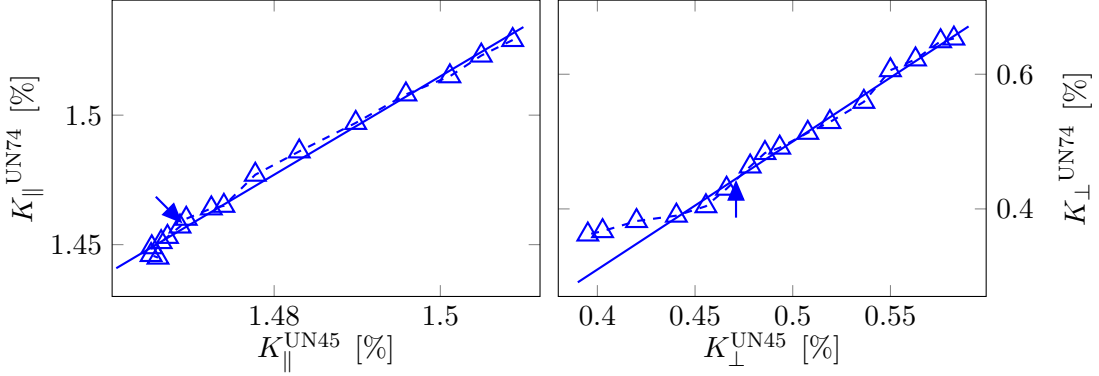


Figure 7.9: Scaling of $K_{\eta}(T)$ for both underdoped samples (temperature as implicit parameter). Straight lines are a guide to the eye with a slope of 1.9.

can be approximated as

$$q_{\eta}\chi(T) = q_{\eta}\Delta\chi(T) + q_{\eta}\chi(T_{\min}) \approx q_{\eta}\Delta\chi(T), \quad (7.22)$$

$$q_{\kappa,\eta}\chi(T) = q_{\kappa,\eta}\Delta\chi(T) + q_{\kappa,\eta}\chi(T_{\min}) \approx q_{\kappa,\eta}\Delta\chi(T), \quad (7.23)$$

with $\Delta\chi(T_{\min}) = \Delta\chi_{\kappa}(T_{\min}) = 0$.

As already stated, the ratios q_{\perp}/q_{\parallel} and $q_{\kappa,\perp}/q_{\kappa,\parallel}$ are needed. While $q_{\perp}/q_{\parallel} \approx 2.5$ can be extracted from the linear regions in Fig. 7.6a, it is more complicated in the case of $q_{\kappa,\perp}/q_{\kappa,\parallel}$. Here, no apparent region exists, where the changes of shift originate only from $q_{\kappa,\eta}\Delta\chi_{\kappa}$, i.e., $K_{\perp}(K_{\parallel})$ having a sample-independent fixed slope in Fig. 7.6a.

Instead, the scaling of the shifts of both underdoped samples can give a hint, cf. Fig. 7.9 (and Fig. 7.7). At high temperatures, i.e., larger shift values, the shifts are described by a linear behavior with a slope of

$$\frac{dK_{\eta}^{\text{UN74}}}{dK_{\eta}^{\text{UN45}}} \approx 1.9, \quad (7.24)$$

that is equal to the ratio of doping levels within the margin of error. At lower temperatures, however, there is a deviation for $\eta = \perp$ that does not exist for $\eta = \parallel$.

Assuming that the shifts for both orientations and samples are given by Eq. (7.13) and

$$q_{\eta}\chi(T)^{\text{UN74}} = kq_{\eta}\chi(T)^{\text{UN45}} \quad (7.25)$$

with a proportionality constant k , a criterion for having used the correct ratio of hyperfine

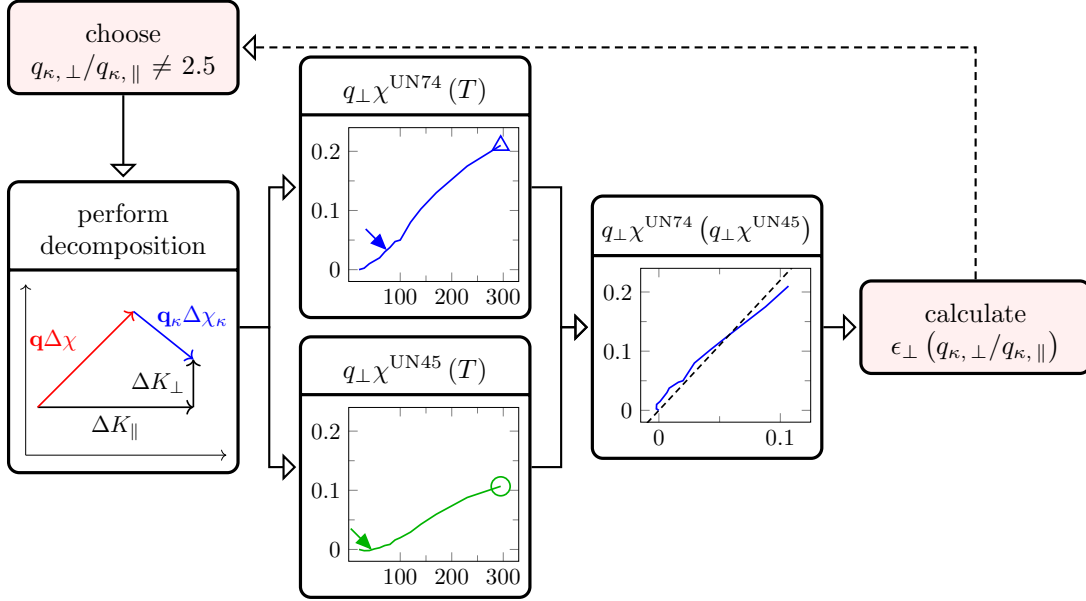


Figure 7.10: Schema for determining $\varepsilon(q_{\kappa,\perp}/q_{\kappa,\parallel})$ (shown curves are for $q_{\kappa,\parallel}/q_{\kappa,\perp} = 0$). For each value of $q_{\kappa,\perp}/q_{\kappa,\parallel}$ the decomposition described by Eqs. (7.18) - (7.21) is performed to obtain $q_{\perp}\chi^{\text{UN45}}(T)$ and $q_{\perp}\chi^{\text{UN74}}(T)$. Using the temperature as an implicit parameter, $q_{\perp}\chi^{\text{UN74}}(q_{\perp}\chi^{\text{UN45}})$ is fitted with a linear regression. Then, the differences of fit and data are used to calculate ε . Afterwards, the procedure is repeated for the next value of $q_{\kappa,\perp}/q_{\kappa,\parallel}$ (dashed arrow).

constants $q_{\kappa,\perp}/q_{\kappa,\parallel}$ can be postulated using the sum of the squared differences from a fit,

$$\varepsilon_{\eta}(q_{\kappa,\perp}/q_{\kappa,\parallel}) = \sqrt{\sum_{T_i} [q_{\eta}\chi^{\text{UN74}}(T_i) - k \cdot q_{\eta}\chi^{\text{UN45}}(T_i)]^2}. \quad (7.26)$$

Here, $q_{\eta}\chi^{\text{UN74}}$ and $q_{\eta}\chi^{\text{UN45}}$ have an implicit dependence on $q_{\kappa,\perp}/q_{\kappa,\parallel}$ due to the calculation according to Eqs. (7.18) - (7.21).

The necessary steps to obtain ε_{η} for a single value of $q_{\kappa,\perp}/q_{\kappa,\parallel}$ are illustrated in Fig. 7.10. Note that the value of ε_{η} only changes by a constant factor of 2.5 if calculated for both orientations η due to $q_{\perp} = 2.5q_{\parallel}$.

Evaluating $\varepsilon(q_{\kappa,\perp}/q_{\kappa,\parallel})$ for a set of values of $q_{\kappa,\perp}/q_{\kappa,\parallel}$ then permits to find the optimum where ε is minimized, cf. Fig. 7.11, with $q_{\kappa,\perp}/q_{\kappa,\parallel} \approx -7.4$. Using this value, the shifts are then separated into $q_{\eta}\chi(T)$ and $q_{\kappa,\eta}\chi_{\kappa}(T)$ for all samples. Fig. 7.12 shows the results for $c \perp B$ which are exactly the same as for $c \parallel B$ except for a factor of 2.5 ($q_{\eta}\chi$) or -7.4 ($q_{\kappa,\eta}\chi_{\kappa}$) respectively. Note that $q_{\kappa,\eta}\chi_{\kappa}(T)$ changes sign as a function of the doping level as already discussed for $\kappa(T)$, cf. Fig. 7.6.

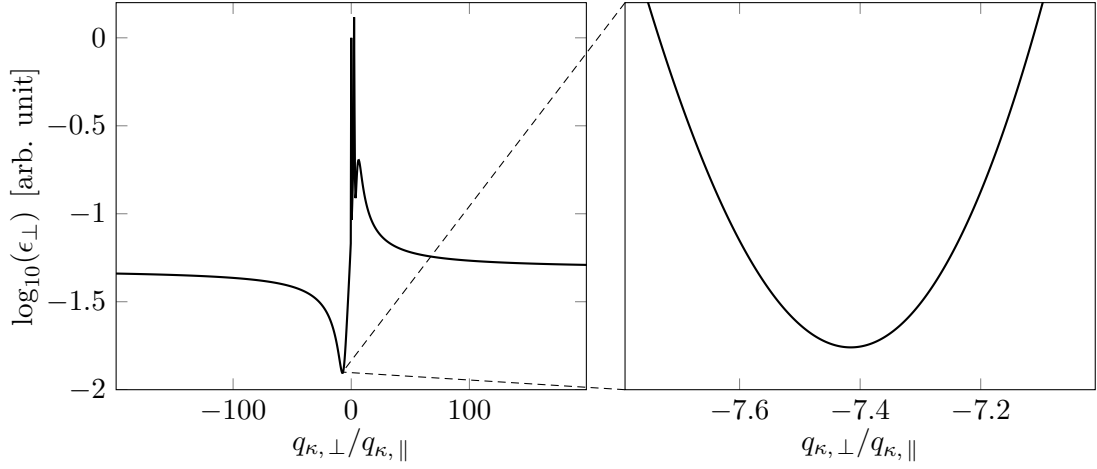


Figure 7.11: Logarithmic fit error ϵ_{\perp} as a function of $q_{\kappa, \perp}/q_{\kappa, \parallel}$ with a minimum for $q_{\kappa, \perp}/q_{\kappa, \parallel} = 7.4$ (enlarged region, right). Maxima occur for $q_{\kappa, \perp}/q_{\kappa, \parallel} = 0, 2.5, 6.2$ but are not of particular interest.

However, only changes relative to the lowest temperature T_{\min} are detected. Therefore, a negative shift contribution $q_{\kappa, \eta}\chi_{\kappa}(T)$ could also stem from decreasing, yet always positive, susceptibility. Furthermore, $q_{\kappa, \eta}$ could also be negative, i.e., the associated susceptibility $\chi(T)$ might have a different sign compared with the extracted shift $q_{\kappa, \eta}\chi_{\kappa}(T)$.

In the case of $q_{\eta}\chi(T)$, the shift contributions are positive for all samples and appear to be growing with doping level. While both underdoped samples UN45 and UN74 do

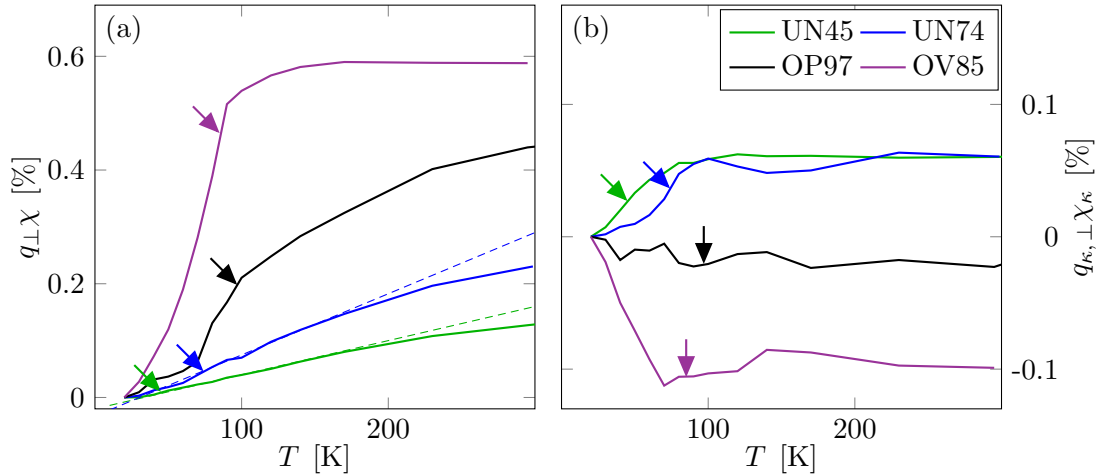


Figure 7.12: Results of the decomposition of the temperature-dependent NMR shifts into $q_{\perp}\chi(T)$ (a) and $q_{\kappa, \perp}\chi_{\kappa}(T)$ (b). Dashed lines in (a) are guides to the eye with a linear temperature dependence.

not show any features around T_c , the optimally doped sample OP97 and the overdoped sample OV85 show a sharp drop towards lower temperatures right around T_c .

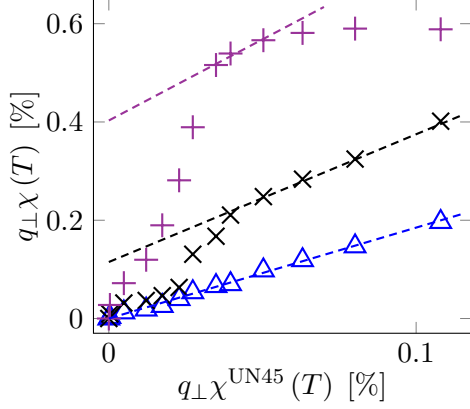


Fig. 7.13: Scaling of the Shift contribution $q_{\perp}\chi$. Dashed lines are guides to the eye.

Similar to the shifts before, Fig. 7.13 shows $q_{\perp}\chi(T)$ for the different samples (except for the UN45) as a function of $q_{\perp}\chi^{\text{UN45}}(T)$ with the temperature as implicit parameter.

In the case of the UN74 sample, a linear dependence is found and the deviation from this behavior towards low temperatures that was present for $K_{\perp}(T)$ is removed. Similar to the observed shifts, the optimally doped OP97 shows a linear, yet not proportional, dependence only above T_c with a temperature-dependent offset that becomes constant for $T > T_c$. The overdoped OV85, however, only shows a range of about 20 K where such a behavior might be present and will not be considered for now.

The presence of a universal (yet scaled) contribution to $q_{\eta}\chi(T)$ suggests an analysis in terms of one component $q_{\eta}\chi_{\text{PG}}(T)$ that complies with property within the whole temperature range and an additional one $q_{\eta}\chi_{\text{FL}}(T)$, both named according to temperature dependence that will be discussed in the following,

$$q_{\eta}\chi(T) = q_{\eta}[\chi_{\text{PG}}(T) + \chi_{\text{FL}}(T)]. \quad (7.27)$$

Due to the linear behavior for low temperatures, cf. Fig. 7.2, the universal pseudogap susceptibility that was discovered in measurements on different cuprate systems, cf. Sect. 7.3, has to produce a Knight shift $q_{\eta}\chi_{\text{PG}}(T)$ also with a linear temperature dependence at low temperatures. Then, comparing $q_{\eta}\chi_{\text{PG}}(T)$ of different samples will produce a linear dependence as well. Since the underdoped UN45 and UN74 show a linear $q_{\eta}\chi(T)$, cf. dashed lines in Fig. 7.12a, it can be concluded that these two samples have a vanishing $\chi_{\text{FL}}(T)$. However, for the analysis, we will only make this assertion for the UN45 sample, meaning

$$q_{\eta}\chi_{\text{PG}}^{\text{UN45}}(T) = q_{\eta}\chi^{\text{UN45}}(T), \quad (7.28)$$

$$q_{\eta}\chi_{\text{FL}}^{\text{UN45}}(T) \equiv 0. \quad (7.29)$$

In case of the $i = \text{UN74}$ and $i = \text{OP97}$ samples, the scaling behavior (with the doping ratios as prefactor x) is assumed for $q_\perp \chi_{\text{PG}}(T)$ in the whole temperature range and the remainder is considered as $\chi_{\text{FL}}(T)$,

$$q_\eta \chi_{\text{PG}}^i(T) = x q_\eta \chi^{\text{UN45}}(T), \quad (7.30)$$

$$x = \frac{p^i}{p^{\text{UN45}}}, \quad (7.31)$$

$$q_\eta \chi_{\text{FL}}^i(T) = q_\eta \chi^i(T) - q_\eta \chi_{\text{PG}}^i(T). \quad (7.32)$$

In the case of the OV85 sample, however, the same approach cannot be used since the shifts $K_\eta(T)$ become constant at higher temperatures, cf. Fig. 7.5. As a consequence, the scaling behavior for $q_\eta \chi_{\text{PG}}^{\text{OV85}}(T)$ with the UN45 sample cannot exist at high temperatures, cf. Fig. 7.13. This failure, however, is to be expected since the universal susceptibility is only linear up to $T/T_{\text{max}} \lesssim 0.5$, cf. Fig. 7.2, and the value of T_{max} decreases with doping. For a doping level of $p^{\text{OV85}} = 0.19$, a $T_{\text{max}} = 242 \text{ K}$ was found in $\text{La}_{2-x}\text{Sr}_x\text{CuO}_4$ [80]. While the exact T_{max} as a function of doping might depend on the system, we assume $T_{\text{max}} = 242 \text{ K}$ for the OV85 sample and use Eq. (7.30) - (7.32) only up to 120 K. Above this temperature, we assume $q_\eta \chi_{\text{FL}}^{\text{OV85}}(T) = \text{constant}$ and attribute all change to $q_\eta \chi_{\text{PG}}^{\text{OV85}}(T)$.

The resulting $q_\perp \chi_{\text{PG}}(T)$ and $q_\perp \chi_{\text{FL}}(T)$ for all samples are shown in Fig. 7.14. The underdoped sample UN74 shows a vanishing $q_\perp \chi_{\text{FL}}(T)$ as expected in contrast to the OP97

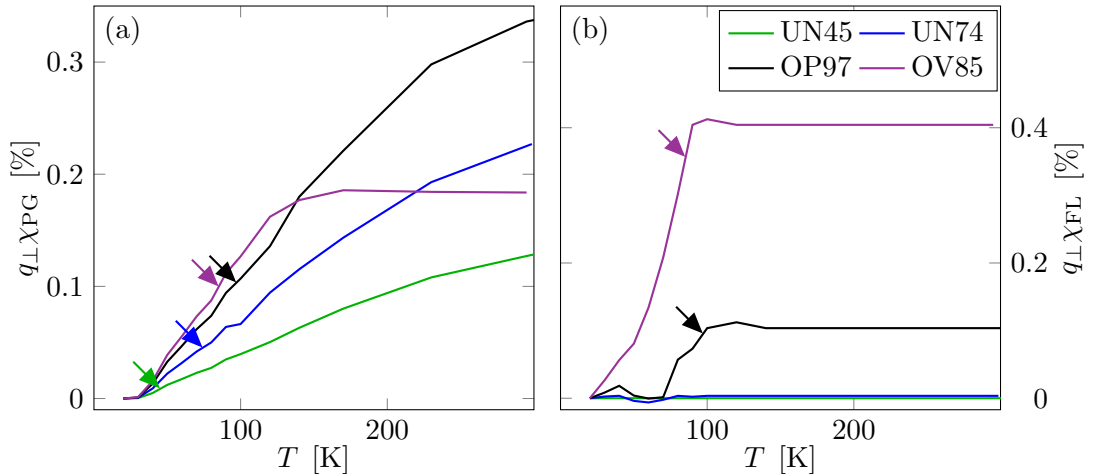


Figure 7.14: Results of the decomposition of $q_\perp \chi(T)$ into a pseudogap component $q_\perp \chi_{\text{PG}}(T)$ (a) and Fermi liquid component $q_\perp \chi_{\text{FL}}(T)$ (b) for all analyzed samples.

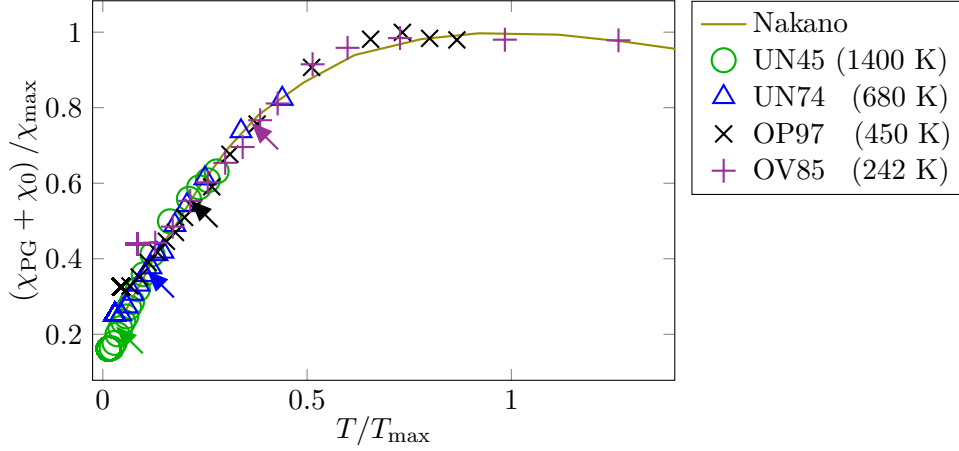


Figure 7.15: Normalized and temperature-scaled $q_{\perp}\chi_{\text{PG}}(T)$ (with a sample-dependent and temperature-independent offset χ_0 , T_{max} values from Ref. [80]) together with the universal curve from Nakano et al. [80] (solid olive line).

and OV85 samples. In these, a sharp drop occurs around T_c . The extracted $q_{\perp}\chi_{\text{PG}}(T)$, however, do not show any signature around the transition temperature. Furthermore, Fig. 7.15 shows the normalized and temperature-scaled $q_{\perp}\chi_{\text{PG}}(T)$ with T_{max} values from $\text{La}_{2-x}\text{Sr}_x\text{CuO}_4$ according to the doping levels [80]. Here, an almost perfect agreement of the extracted shift contribution and the universal susceptibility that was identified by Johnston [44] and Nakano et al. [80], cf. Fig. 7.2, is found. Note that in the analysis, this universal susceptibility was merely used as an additional justification for the assumed scaling behavior without any direct role in the decomposition procedure.

7.6 Summary

Based on the temperature-dependent ^{63}Cu NMR shift values in $\text{HgBa}_2\text{CuO}_{4+\delta}$, a failure of the prevalent single-fluid model was found. Instead three distinct components were identified, giving a temperature-dependent description of the shifts according to

$$K_{\parallel} = q_{\parallel} [\chi_{\text{PG}}(T) + \chi_{\text{FL}}(T)] + q_{\kappa, \parallel} \chi_{\kappa}(T), \quad (7.33)$$

$$K_{\perp} = q_{\perp} [\chi_{\text{PG}}(T) + \chi_{\text{FL}}(T)] + q_{\kappa, \perp} \chi_{\kappa}(T). \quad (7.34)$$

A subsequent decomposition allowed for the extraction of the temperature dependence of each one. This yielded a universal pseudogap-like component $q_{\eta}\chi_{\text{PG}}(T)$ (changes only the temperature scale and amplitude upon doping), a Fermi liquid-like $q_{\eta}\chi_{\text{FL}}(T)$ (constant above T_c , only present at higher doping levels), and a third $q_{\kappa, \eta}\chi_{\kappa}(T)$ (changes sign as

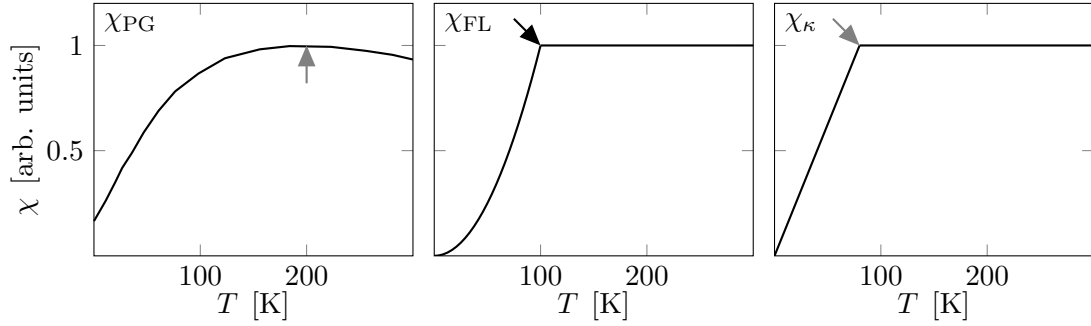


Figure 7.16: Sketch of the identified susceptibility components in $\text{HgBa}_2\text{CuO}_{4+\delta}$ that were detected in the NMR shifts. The superconducting transition temperature appears to be only relevant for $\chi_{\text{FL}}(T)$. The arrows indicate the characteristic temperatures T_{max} , T_c , and T_0 (in that order).

a function of doping and becomes constant above a certain temperature T_0 that depends only weakly on doping), cf. Fig. 7.16.

However, the physical interpretation of the presence of three components with the observed temperature dependences and the role for superconductivity remains to be explained by theory.

CHAPTER 8

Conclusion

In this thesis, three separate topics were presented. These include the development of novel experimental NMR methods and data analysis, as well as their application to current topics of condensed matter research.

The first part concerns NMR at the highest magnetic fields, i.e., in time-dependent pulsed high-field magnets. After a discussion of consequences for NMR, a method to acquire broad spectra was presented. Here, an intensity-correction for off-resonance effects was applied and the Fourier transform was modified to use time-dependent base functions. Subsequently, the method was tested with a Knight shift measurement of metallic aluminum using a second compound as a shift reference. It could be shown that signal averaging of a weak signal is possible, even across multiple field pulses. Thus, in principle, the signal-to-noise ratio can always be increased at the cost of measurement time, despite the inherently limited reproducibility of subsequent field high-field pulses. In another set of experiments, the feasibility of T_1 measurements was shown. Here, a weak radio frequency field was used to perform an adiabatic inversion of the spin system in the time-dependent field. Ensuing small-angle RF pulses monitored the relaxation process. Using a mathematical model, T_1 was then determined.

Finally, this method was applied for the investigation of the spin-dimer antiferromagnet $\text{SrCu}_2(\text{BO}_3)_2$. Evidence for a field-induced change in the ground state of the material was found. This appears to be the first convincing observation of a field-induced phenomenon with pulsed field NMR. It proves that nuclear magnetic resonance spectroscopy at the highest fields is able to produce unique insights into quantum materials.

The second part of the thesis concerns NMR investigations and analysis of cuprate high-temperature superconductors in conventional static field measurements. Results on $\text{HgBa}_2\text{CuO}_{4+\delta}$ for underdoped, optimally doped, and overdoped materials revealed that the measured shifts could not be understood with a single electronic spin component. The question arose how one can reconcile these findings in terms of basic NMR phenomenology. An analysis revealed the presence of three distinct contributions: A universal pseudogap component, a Fermi liquid-like component that only emerges at higher doping levels, and a third component that changes sign around optimal doping. This discovery demands the development of new theory for the understanding of cuprate superconductors.

The last topic concerns the dynamics of large dipolar coupled nuclear spin systems. In presence of a large oscillating magnetic field, additional non-secular resonances at frequencies different from the Larmor frequency are predicted. The presented preliminary results from ongoing experiments showed a sufficient ratio of the RF field and the static magnetic field according to the predictions, however, no effect has been observed yet.

Bibliography

- [1] Abou-Hamad, E., Bontemps, P., and Rikken, G. ‘NMR in pulsed magnetic field.’ In: *Solid State Nucl. Magn. Reson.* 40 (2011), p. 42. DOI: 10.1016/j.ssnmr.2011.06.002 (cit. on pp. 2, 17).
- [2] Abragam, A. ‘Principles of Nuclear Magnetism’. Oxford University Press, USA, 1960 (cit. on pp. 5, 11, 108).
- [3] Bankay, M., Mali, M., Roos, J., and Brinkmann, D. ‘Single-spin fluid, spin gap, and d-wave pairing in YBa₂Cu₄O₈: A NMR and NQR study’. In: *Phys. Rev. B* 50 (1994), p. 6416. DOI: 10.1103/PhysRevB.50.6416 (cit. on p. 76).
- [4] Barišić, N., Chan, M. K., Li, Y., Yu, G., Zhao, X., Dressel, M., Smontara, A., and Greven, M. ‘Universal sheet resistance and revised phase diagram of the cuprate high-temperature superconductors.’ In: *Proc. Natl. Acad. Sci. U. S. A.* 110 (2013), p. 12235. DOI: 10.1073/pnas.1301989110 (cit. on p. 74).
- [5] Barišić, N., Li, Y., Zhao, X., Cho, Y.-C., Chabot-Couture, G., Yu, G., and Greven, M. ‘Demonstrating the model nature of the high-temperature superconductor HgBa₂CuO_{4+δ}’. In: *Phys. Rev. B* 78 (2008), p. 054518. DOI: 10.1103/PhysRevB.78.054518 (cit. on p. 78).
- [6] Barzykin, V. and Pines, D. ‘Phenomenological Model of Protected Behavior in the Pseudogap State of Underdoped Cuprate Superconductors’. In: *Phys. Rev. Lett.* 96 (2006), p. 247002. DOI: 10.1103/PhysRevLett.96.247002 (cit. on pp. 76, 77).
- [7] Baum, J., Tycko, R., and Pines, A. ‘Broadband and adiabatic inversion of a two-level system by phase-modulated pulses’. In: *Phys. Rev. A* 32 (1985), p. 3435. DOI: 10.1103/PhysRevA.32.3435 (cit. on pp. 11, 116).
- [8] Bednorz, J. G. and Müller, K. A. ‘Possible high T_c superconductivity in the Ba-La-Cu-O system’. In: *Z. Phys. B - Condens. Matter* 193 (1986), p. 189. DOI: 10.1007/BF01303701 (cit. on p. 73).

- [9] Bloch, F., Hansen, W. W., and Packard, M. ‘Nuclear Induction’. In: *Phys. Rev.* 69 (1946), p. 127. DOI: 10.1103/PhysRev.69.127 (cit. on p. 1).
- [10] Bloch, F. ‘Nuclear Induction’. In: *Phys. Rev.* 70 (1946), p. 460. DOI: 10.1103/PhysRev.70.460 (cit. on pp. 1, 11).
- [11] Carter, G. C., Bennett, L. H., and Kahan, D. J. ‘Metallic Shifts in Nuclear Magnetic Resonance (Progress in Materials Science)’. Pergamon Press, 1977 (cit. on pp. 41, 42, 46, 50).
- [12] Chen, W., Ma, H., Yu, D., and Zhang, H. ‘SVD-Based Technique for Interference Cancellation and Noise Reduction in NMR Measurement of Time-Dependent Magnetic Fields’. In: *Sensors* 3 (2016), p. 323. DOI: 10.3390/s16030323 (cit. on p. 18).
- [13] Clogston, A. M. and Jaccarino, V. ‘Susceptibilities and negative knight shifts of intermetallic compounds’. In: *Phys. Rev.* 121 (1961), p. 1357. DOI: 10.1103/PhysRev.121.1357 (cit. on p. 11).
- [14] Comin, R. et al. ‘Symmetry of charge order in cuprates’. In: *Nat. Mater.* 14 (2015), p. 796. DOI: 10.1038/nmat4295 (cit. on p. 78).
- [15] Dabkowska, H. A., Dabkowski, A. B., Luke, G. M., Dunsiger, S. R., Haravifard, S., Cecchinell, M., and Gaulin, B. D. ‘Crystal growth and magnetic behaviour of pure and doped $\text{SrCu}_2(^{11}\text{BO}_3)_2$ ’. In: *J. Cryst. Growth* 306 (2007), p. 123. DOI: 10.1016/j.jcrysgro.2007.04.040 (cit. on p. 59).
- [16] Damadian, R. ‘Tumor detection by nuclear magnetic resonance’. In: *Science* 171 (1971), p. 1151. DOI: 10.1126/science.171.3976.1151 (cit. on p. 1).
- [17] Damascelli, A., Hussain, Z., and Shen, Z.-X. ‘Angle-resolved photoemission studies of the cuprate superconductors’. In: *Rev. Mod. Phys.* 75 (2003), p. 473. DOI: 10.1103/RevModPhys.75.473 (cit. on p. 78).
- [18] Debray, F., Jongbloets, H., Joss, W., Martinez, G., Mossang, E., Picoche, J. C., Plante, A., Rub, P., Sala, P., and Wyder, P. ‘Grenoble High Magnetic Field Laboratory as a user facility’. In: *Phys. B Condens. Matter* 294-295 (2001), p. 523. DOI: 10.1016/S0921-4526(00)00714-6 (cit. on p. 16).
- [19] Ding, H., Zhou, J., Xu, Y., Ding, T., Xiao, H., Li, L., and Hu, J. ‘Design of a Current-Controlled Power Supply for High-Stability Flat-Top Pulsed Magnetic Field’. In: *IEEE Trans. Appl. Supercond.* 26 (2016), p. 1. DOI: 10.1109/TASC.2015.2513211 (cit. on p. 16).

- [20] Doiron-Leyraud, N. ‘The Fermi surface of cuprate superconductors’. In: *Phys. Canada* 67 (2011), p. 89. URL: <https://www.cap.ca/en/article/fermi-surface-cuprate-superconductors> (cit. on p. 77).
- [21] Efetov, K. B., Meier, H., and Pépin, C. ‘Pseudogap state near a quantum critical point’. In: *Nat. Phys.* 9 (2013), p. 442. DOI: 10.1038/nphys2641 (cit. on p. 3).
- [22] Engelsberg, M. and Lowe, I. J. ‘Free-induction-decay measurements and determination of moments in CaF_2 ’. In: *Phys. Rev. B* 10 (08/1974), p. 822. DOI: 10.1103/PhysRevB.10.822 (cit. on p. 110).
- [23] Ernst, R., Bodenhausen, G., and Wokaun, A. ‘Principles of Nuclear Magnetic Resonance in One and Two Dimensions (International Series of Monographs on Chemistry)’. Clarendon Press, 1990 (cit. on p. 27).
- [24] Evangelisti, R., Pasotti, G., and Sacerdoti, G. ‘A pulsed magnet for high magnetic fields’. In: *Nucl. Instruments Methods* 16 (1962), p. 189. DOI: 10.1016/0029-554X(62)90116-7 (cit. on p. 16).
- [25] Farrar, T. C. and Becker, E. D. ‘Pulse and Fourier transform NMR: introduction to theory and methods’. Academic Press, 1971 (cit. on p. 12).
- [26] Freude, D. and Behrens, H.-J. ‘Investigation of ^{27}Al NMR chemical shifts in zeolites of the faujasite type’. In: *Cryst. Res. Techn.* 16 (1981), K36. DOI: 10.1002/crat.19810160322 (cit. on p. 42).
- [27] Freude, D. and Haase, J. ‘Quadrupole Effects in Solid-State Nuclear Magnetic Resonance’. In: *NMR Basic Princ. Prog.* Ed. by Pfeifer, H. and Barker, P. Springer Berlin Heidelberg, 1993, p. 1. DOI: 10.1007/978-3-642-50046-6_1 (cit. on p. 5).
- [28] Gan, Z., Kwak, H.-T., Bird, M., Cross, T., Gor’kov, P., Brey, W., and Shetty, K. ‘High-field NMR using resistive and hybrid magnets’. In: *J. Magn. Reson.* 191 (2008), p. 135. DOI: 10.1016/j.jmr.2007.12.008 (cit. on p. 19).
- [29] Haase, J., Conradi, M., Grey, C., and Vega, A. ‘Population Transfers for NMR of Quadrupolar Spins in Solids’. In: *J. Magn. Reson. Ser. A* 109 (1994), p. 90. DOI: 10.1006/jmra.1994.1138 (cit. on pp. 11, 116).
- [30] Haase, J., Eckert, D., Siegel, H., Eschrig, H., Müller, K.-H., Simon, A., and Steglich, F. ‘NMR at the frontier of pulsed high field magnets’. In: *Phys. B Condens. Matter* 346-347 (2004), p. 514. DOI: 10.1016/j.physb.2004.01.138 (cit. on p. 18).

- [31] Haase, J., Eckert, D., Siegel, H., Eschrig, H., Müller, K.-H., and Steglich, F. ‘Nuclear magnetic resonance in pulsed high-field magnets’. In: *Concepts Magn. Reson.* 19B (2003), p. 9. DOI: 10.1002/cmr.b.10084 (cit. on pp. 2, 17).
- [32] Haase, J., Kozlov, M. B., Webb, A. G., Büchner, B., Eschrig, H., Müller, K.-H., and Siegel, H. ‘2 GHz ^1H NMR in pulsed magnets’. In: *Solid State Nucl. Magn. Reson.* 27 (2005), p. 206. DOI: 10.1016/j.ssnmr.2004.10.002 (cit. on p. 17).
- [33] Haase, J., Slichter, C. P., and Williams, G. V. M. ‘Evidence for two electronic components in high-temperature superconductivity from NMR’. In: *J. Phys. Condens. Matter* 21 (2009), p. 455702. DOI: 10.1088/0953-8984/21/45/455702 (cit. on pp. 3, 76, 77).
- [34] Haase, J., Slichter, C. P., and Williams, G. V. M. ‘Two-component behaviour of high-temperature superconductors from NMR’. In: *J. Phys. Condens. Matter* 20 (2008), p. 434227. DOI: 10.1088/0953-8984/20/43/434227 (cit. on pp. 3, 76, 77).
- [35] Haase, J., Steglich, F., Eckert, D., Siegel, H., Eschrig, H., and Müller, K. ‘High-field NMR in pulsed magnets’. In: *Solid State Nucl. Magn. Reson.* 23 (2003), p. 263. DOI: 10.1016/S0926-2040(03)00015-8 (cit. on p. 17).
- [36] Haase, J., Rybicki, D., Slichter, C. P., Greven, M., Yu, G., Li, Y., and Zhao, X. ‘Two-component uniform spin susceptibility of superconducting $\text{HgBa}_2\text{CuO}_{4+\delta}$ crystals measured using ^{63}Cu and ^{199}Hg nuclear magnetic resonance’. In: *Phys. Rev. B* 85 (2012), p. 104517. DOI: 10.1103/PhysRevB.85.104517 (cit. on p. 78).
- [37] Hahn, E. L. ‘Nuclear induction due to free larmor precession’. In: *Phys. Rev.* 77 (1950), p. 297. DOI: 10.1103/PhysRev.77.297.2 (cit. on p. 12).
- [38] Hebel, L. C. and Slichter, C. P. ‘Nuclear Spin Relaxation in Normal and Superconducting Aluminum’. In: *Phys. Rev.* 113 (1959), p. 1504. DOI: 10.1103/PhysRev.113.1504 (cit. on p. 1).
- [39] Herlach, F. and Miura, N. ‘High Magnetic Fields: Science and Technology’. Condensed Matter Physics Series Magnet Technology and Experimental Techniques. Singapore: World Scientific, 2003. DOI: 10.1142/4764-vol1 (cit. on p. 2).
- [40] Hücker, M., Gu, G. D., and Tranquada, J. M. ‘Spin susceptibility of underdoped cuprate superconductors: Insights from a stripe-ordered crystal’. In: *Phys. Rev. B* 78 (2008), p. 214507. DOI: 10.1103/PhysRevB.78.214507 (cit. on p. 82).

- [41] Iijima, T. and Takegoshi, K. ‘Compensation of effect of field instability by reference deconvolution with phase reconstruction’. In: *J. Magn. Reson.* 191 (2008), p. 128. DOI: 10.1016/j.jmr.2007.12.009 (cit. on p. 19).
- [42] Islam, R. S., Cooper, J. R., Loram, J. W., and Naqib, S. H. ‘Pseudogap and doping-dependent magnetic properties of $\text{La}_{2-x}\text{Sr}_x\text{Cu}_{1-y}\text{Zn}_y\text{O}_4$ ’. In: *Phys. Rev. B* 81 (2010), p. 054511. DOI: 10.1103/PhysRevB.81.054511 (cit. on p. 77).
- [43] Jeener, J. and Broekaert, P. ‘Nuclear Magnetic Resonance in Solids: Thermodynamic Effects of a Pair of rf Pulses’. In: *Phys. Rev.* 157 (05/1967), p. 232. DOI: 10.1103/PhysRev.157.232 (cit. on p. 110).
- [44] Johnston, D. C. ‘Magnetic Susceptibility Scaling in $\text{La}_{2-x}\text{Sr}_x\text{CuO}_{4-y}$ ’. In: *Phys. Rev. Lett.* 62 (1989), p. 957. DOI: 10.1103/PhysRevLett.62.957 (cit. on pp. 76, 89).
- [45] Jones, E., Oliphant, T., Peterson, P., et al. ‘SciPy: Open source scientific tools for Python’. URL: <http://www.scipy.org/> (cit. on p. 33).
- [46] Kageyama, H., Yoshimura, K., Stern, R., Mushnikov, N. V., Onizuka, K., Kato, M., Kosuge, K., Slichter, C. P., Goto, T., and Ueda, Y. ‘Exact Dimer Ground State and Quantized Magnetization Plateaus in the Two-Dimensional Spin System $\text{SrCu}_2(\text{BO}_3)_2$ ’. In: *Phys. Rev. Lett.* (1999), p. 3. DOI: 10.1103/PhysRevLett.82.3168 (cit. on pp. 53, 55).
- [47] Kapitza, P. L. ‘A Method of Producing Strong Magnetic Fields’. In: *Proc. R. Soc. A* 105 (1924), p. 691. DOI: 10.1098/rspa.1924.0048 (cit. on p. 16).
- [48] Kaptein, R., Dijkstra, K., and Tarr, C. ‘A single-scan fourier transform method for measuring spin-lattice relaxation times’. In: *J. Magn. Reson.* 24 (1976), p. 295. DOI: 10.1016/0022-2364(76)90039-1 (cit. on p. 40).
- [49] Kellogg, J. M. B., Rabi, I. I., Ramsey, N. F. J., and Zacharias, J. R. ‘The Magnetic Moments of the Proton and the Deuteron - The Radiofrequency Spectrum of H_2 in Various Magnetic Fields’. In: *Phys. Rev.* 56 (1939), p. 728. DOI: 10.1103/PhysRev.56.728 (cit. on p. 1).
- [50] Kivelson, S. A., Bindloss, I. P., Fradkin, E., Oganessian, V., Tranquada, J. M., Kapitulnik, A., and Howald, C. ‘How to detect fluctuating stripes in the high-temperature superconductors’. In: *Rev. Mod. Phys.* 75 (2003), p. 1201. DOI: 10.1103/RevModPhys.75.1201 (cit. on p. 78).

- [51] Kodama, K., Takigawa, M., Horvatić, M., Berthier, C., Kageyama, H., Ueda, Y., Miyahara, S., Becca, F., and Mila, F. ‘Magnetic Superstructure in the Two-Dimensional Quantum Antiferromagnet $\text{SrCu}_2(\text{BO}_3)_2$ ’. In: *Science* 298 (2002), p. 395. DOI: 10.1126/science.1075045 (cit. on pp. 1, 3, 58, 68).
- [52] Kodama, K., Yamazaki, J., Takigawa, M., Kageyama, H., Onizuka, K., and Ueda, Y. ‘Cu nuclear spin-spin coupling in the dimer singlet state in $\text{SrCu}_2(\text{BO}_3)_2$ ’. In: *J. Phys. Condens. Matter* 14 (2002), p. L319. DOI: 10.1088/0953-8984/14/17/101 (cit. on p. 63).
- [53] Kohlrautz, J. ‘Zeitentwicklung stark korrelierter Kernspinzustände’. Diplomarbeit. Universität Leipzig, 2011 (cit. on p. 3).
- [54] Kohlrautz, J. and Kühne, H. ‘Pulsed-field broadband NMR of $\text{SrCu}_2(\text{BO}_3)_2$ ’. In: *EMFL NEWS No. 3*. 2016, p. 6. URL: http://www.emfl.eu/fileadmin/emfl.eu/user_upload/Media/Newsletter/emfl_newsletter_3_16_web.pdf (cit. on p. 53).
- [55] Kohlrautz, J., Reichardt, S., Green, E. L., Kühne, H., Wosnitza, J., and Haase, J. ‘NMR shift and relaxation measurements in pulsed high-field magnets up to 58 T’. In: *J. Magn. Reson.* 263 (2016), p. 1. DOI: 10.1016/j.jmr.2015.12.009 (cit. on pp. 1, 41).
- [56] Kohlrautz, J., Haase, J., Green, E., Zhang, Z., Wosnitza, J., Herrmannsdörfer, T., Dabkowska, H., Gaulin, B., Stern, R., and Kühne, H. ‘Field-stepped broadband NMR in pulsed magnets and application to $\text{SrCu}_2(\text{BO}_3)_2$ at 54 T’. In: *J. Magn. Reson.* 271 (2016), p. 52. DOI: 10.1016/j.jmr.2016.08.005 (cit. on pp. 1, 53).
- [57] Kokanović, I., Cooper, J. R., and Kozumasa, I. ‘Changes in the in- and out-of-plane magnetic susceptibility of YBCO crystals with temperature and hole content’. In: *EPL* 98 (2012), p. 57011. DOI: 10.1209/0295-5075/98/57011 (cit. on pp. 76, 77).
- [58] Kozlov, M. B., Haase, J., Baumann, C., and Webb, A. G. ‘56 T ^1H NMR at 2.4 GHz in a pulsed high-field magnet’. In: *Solid State Nucl. Magn. Reson.* 28 (2005), p. 64. DOI: 10.1016/j.ssnmr.2005.06.003 (cit. on p. 18).
- [59] Kropf, C. M. and Fine, B. V. ‘Nonsecular resonances for the coupling between nuclear spins in solids’. In: *Phys. Rev. B* 86 (2012), p. 094401. DOI: 10.1103/PhysRevB.86.094401 (cit. on pp. 3, 107, 108).

- [60] Kropf, C. M., Kohlrautz, J., Haase, J., and Fine, B. V. ‘Anomalous longitudinal relaxation of nuclear spins in CaF_2 ’. In: *Fortschr. Phys.* (2016). DOI: 10.1002/prop.201600023 (cit. on pp. 1, 107, 109–111, 114).
- [61] Krug, H. et al. ‘The Dresden high-magnetic field laboratory - overview and first results’. In: *Phys. B Condens. Matter* 295 (2001), p. 605. DOI: 10.1016/S0921-4526(00)00728-6 (cit. on p. 16).
- [62] Kupce, E. and Freeman, R. ‘Adiabatic pulses for wideband inversion and broadband decoupling’. In: *J. Magn. Reson. Ser. A* 115 (1995), p. 273. DOI: 10.1006/jmra.1995.1179 (cit. on pp. 11, 12).
- [63] Lacroix, C., Mendels, P., and Mila, F., eds. ‘Introduction to Frustrated Magnetism’. Vol. 164. Springer Series in Solid-State Sciences. Springer Berlin Heidelberg, 2011. DOI: 10.1007/978-3-642-10589-0 (cit. on pp. 53, 55, 56, 59).
- [64] Levitt, M. H. ‘Spin Dynamics: Basics of Nuclear Magnetic Resonance’. 2nd ed. Wiley, 2008 (cit. on pp. 1, 5, 110).
- [65] Loram, J., Mirza, K., Cooper, J., and Tallon, J. ‘Specific Heat Evidence on the Normal State Pseudogap’. In: *J. Phys. Chem. Solids* 59 (1998), p. 2091. DOI: 10.1016/S0022-3697(98)00180-2 (cit. on p. 76).
- [66] Mansfield, P. and Grannell, P. K. ‘NMR ‘diffraction’ in solids?’ In: *J. Phys. C Solid State Phys.* 6 (1973), p. L422. DOI: 10.1088/0022-3719/6/22/007 (cit. on p. 1).
- [67] Matsuda, Y. H., Abe, N., Takeyama, S., Kageyama, H., Corboz, P., Honecker, A., Manmana, S. R., Foltin, G. R., Schmidt, K. P., and Mila, F. ‘Magnetization of $\text{SrCu}_2(\text{BO}_3)_2$ in Ultrahigh Magnetic Fields up to 118 T’. In: *Phys. Rev. Lett.* 111 (2013), p. 137204. DOI: 10.1103/PhysRevLett.111.137204 (cit. on pp. 56, 57).
- [68] Matsumoto, S., Kiyoshi, T., Otsuka, A., Hamada, M., Maeda, H., Yanagisawa, Y., Nakagome, H., and Suematsu, H. ‘Generation of 24 T at 4.2 K using a layer-wound GdBCO insert coil with Nb_3Sn and Nb–Ti external magnetic field coils’. In: *Supercond. Sci. Technol.* 25 (2012), p. 025017. DOI: 10.1088/0953-2048/25/2/025017 (cit. on p. 15).
- [69] Meier, B. ‘Nuclear Magnetic Resonance in pulsed high magnetic fields’. PhD thesis. Universität Leipzig, 2012. URL: <http://nbn-resolving.de/urn:nbn:de:bsz:15-qucosa-101205> (cit. on p. 121).

- [70] Meier, B., Kohlrautz, J., and Haase, J. ‘Eigenmodes in the Long-Time Behavior of a Coupled Spin System Measured with Nuclear Magnetic Resonance’. In: *Phys. Rev. Lett.* 108 (2012), p. 1. DOI: 10.1103/PhysRevLett.108.177602 (cit. on pp. 3, 107, 110).
- [71] Meier, B., Kohlrautz, J., Haase, J., Braun, M., Wolff-Fabris, F., Kampert, E., Herrmannsdörfer, T., and Wosnitza, J. ‘Nuclear magnetic resonance apparatus for pulsed high magnetic fields’. In: *Rev. Sci. Instrum.* 83 (2012), p. 083113. DOI: 10.1063/1.4746988 (cit. on pp. 16, 18, 121).
- [72] Meier, B., Greiser, S., Haase, J., Herrmannsdörfer, T., Wolff-Fabris, F., and Wosnitza, J. ‘NMR signal averaging in 62 T pulsed fields’. In: *J. Magn. Reson.* 210 (2011), p. 1. DOI: 10.1016/j.jmr.2011.02.007 (cit. on pp. 2, 18, 19, 26).
- [73] Meissner, T., Goh, S., Haase, J., Williams, G., and Littlewood, P. ‘High-pressure spin shifts in the pseudogap regime of superconducting $\text{YBa}_2\text{Cu}_4\text{O}_8$ as revealed by ^{17}O NMR’. In: *Phys. Rev. B* 83 (2011), p. 1. DOI: 10.1103/PhysRevB.83.220517 (cit. on pp. 3, 77).
- [74] Mila, F. and Rice, T. ‘Analysis of magnetic resonance experiments in $\text{YBa}_2\text{Cu}_3\text{O}_7$ ’. In: *Phys. C Supercond.* 157 (1989), p. 561. DOI: 10.1016/0921-4534(89)90286-4 (cit. on p. 75).
- [75] Mila, F. and Takigawa, M. ‘Iterative deconvolution of quadrupole split NMR spectra’. In: *Eur. Phys. J. B* 86 (2013), p. 354. DOI: 10.1140/epjb/e2013-40544-x (cit. on p. 58).
- [76] Mispelter, J., Lupu, M., and Briguet, A. ‘NMR Probeheads for Biophysical and Biomedical Experiments: Theoretical Principles and Practical Guidelines’. Ed. by Tjan, K. W. Imperial College Press, 2006, p. 596 (cit. on p. 13).
- [77] Miyahara, S., Becca, F., and Mila, F. ‘Theory of spin-density profile and lattice distortion in the magnetization plateaus of $\text{SrCu}_2(\text{BO}_3)_2$ ’. In: *Phys. Rev. B* 68 (2003), p. 024401. DOI: 10.1103/PhysRevB.68.024401 (cit. on pp. 53, 56).
- [78] Miyahara, S. and Ueda, K. ‘Exact Dimer Ground State of the Two Dimensional Heisenberg Spin System $\text{SrCu}_2(\text{BO}_3)_2$ ’. In: *Phys. Rev. Lett.* 82 (1999), p. 3701. DOI: 10.1103/PhysRevLett.82.3701 (cit. on pp. 55, 57).

- [79] Mounce, A. M., Oh, S., Lee, J. A., Halperin, W. P., Reyes, A. P., Kuhns, P. L., Chan, M. K., Dorow, C., Ji, L., Xia, D., Zhao, X., and Greven, M. ‘Absence of static loop-current magnetism at the apical oxygen site in $\text{HgBa}_2\text{CuO}_{4+\delta}$ from NMR’. In: *Phys. Rev. Lett.* 111 (2013), p. 1. DOI: 10.1103/PhysRevLett.111.187003 (cit. on p. 75).
- [80] Nakano, T., Oda, M., Manabe, C., Momono, N., Miura, Y., and Ido, M. ‘Magnetic properties and electronic conduction of superconducting $\text{La}_{2-x}\text{Sr}_x\text{CuO}_4$ ’. In: *Phys. Rev. B* 49 (1994), p. 16000. DOI: 10.1103/PhysRevB.49.16000 (cit. on pp. 76, 88, 89).
- [81] National Research Council. ‘High Magnetic Field Science and Its Application in the United States: Current Status and Future Directions’. The National Academies Press, 2013. DOI: 10.17226/18355 (cit. on pp. 2, 16).
- [82] Newville, M., Stensitzki, T., Allen, D. B., and Ingargiola, A. ‘LMFIT: Non-Linear Least-Square Minimization and Curve-Fitting for Python’. 2014. DOI: 10.5281/zenodo.11813 (cit. on p. 38).
- [83] O’Connor, C. J. ‘Magnetic-Susceptibility Measurement Techniques’. In: *Mol. Magnetic Mater.* 1996. Chap. 4, p. 44. DOI: 10.1021/bk-1996-0644.ch004 (cit. on p. 76).
- [84] Oda, M., Matsuki, H., and Ido, M. ‘Common features of magnetic and superconducting properties in Y-doped $\text{Bi}_2(\text{Sr},\text{Ca})_3\text{Cu}_2\text{O}_8$ and Ba(Sr)-doped La_2CuO_4 ’. In: *Solid State Commun.* 74 (1990), p. 1321. DOI: 10.1016/0038-1098(90)91000-7 (cit. on p. 76).
- [85] Ohsugi, S., Kitaoka, Y., Ishida, K., Zheng, G.-q., and Asayama, K. ‘Cu NMR and NQR Studies of High- T_c Superconductor $\text{La}_{2-x}\text{Sr}_x\text{CuO}_4$ ’. In: *J. Phys. Soc. Japan* 63 (1994), p. 700. DOI: 10.1143/JPSJ.63.700 (cit. on pp. 3, 77).
- [86] Onizuka, K., Kageyama, H., Narumi, Y., Kindo, K., Ueda, Y., and Goto, T. ‘1/3 Magnetization Plateau in $\text{SrCu}_2(\text{BO}_3)_2$ - Stripe Order of Excited Triplets -’. In: *J. Phys. Soc. Japan* 69 (2000), p. 1016. DOI: 10.1143/JPSJ.69.1016 (cit. on p. 56).
- [87] Orlova, A., Frings, P., Suleiman, M., and Rikken, G. ‘New high homogeneity 55T pulsed magnet for high field NMR’. In: *J. Magn. Reson.* 268 (2016), p. 82. DOI: 10.1016/j.jmr.2016.04.016 (cit. on p. 17).

- [88] Pake, G. E. ‘Nuclear Resonance Absorption in Hydrated Crystals: Fine Structure of the Proton Line’. In: *J. Chem. Phys.* 16 (1948), p. 327. DOI: 10.1063/1.1746878 (cit. on p. 10).
- [89] Perenboom, J., Peters, R., Roeterdink, T., Wiegers, S., Zwinkels, P., Frings, P., and Maan, J.-K. ‘The new 20 MW high magnetic field installation at the University of Nijmegen’. In: *Phys. B* 295 (2001), p. 529. DOI: 10.1016/S0921-4526(00)00715-8 (cit. on p. 16).
- [90] Purcell, E., Torrey, H., and Pound, R. ‘Resonance Absorption by Nuclear Magnetic Moments in a Solid’. In: *Phys. Rev.* 69 (1946), p. 37. DOI: 10.1103/PhysRev.69.37 (cit. on p. 1).
- [91] Putilin, S. N., Antipov, E. V., Chmaissem, O., and Marezio, M. ‘Superconductivity at 94 K in $\text{HgBa}_2\text{CuO}_{4+\delta}$ ’. In: *Nature* 362 (1993), p. 226. DOI: 10.1038/362226a0 (cit. on p. 74).
- [92] Redfield, A. G. ‘Nuclear Magnetic Resonance Saturation and Rotatory Saturation in Solids’. In: *Phys. Rev.* 98 (1955), p. 1787. DOI: 10.1103/PhysRev.98.1787 (cit. on p. 108).
- [93] Renold, S., Heine, T., Weber, J., and Meier, P. F. ‘Nuclear magnetic resonance chemical shifts and paramagnetic field modifications in La_2CuO_4 ’. In: *Phys. Rev. B* 67 (2003), p. 024501. DOI: 10.1103/PhysRevB.67.024501 (cit. on p. 79).
- [94] Rybicki, D., Haase, J., Greven, M., Yu, G., Li, Y., Cho, Y., and Zhao, X. ‘Spatial inhomogeneities in single-crystal $\text{HgBa}_2\text{CuO}_{4+\delta}$ from ^{63}Cu NMR spin and quadrupole shifts’. In: *J. Supercond. Nov. Magn.* 22 (2009), p. 179. DOI: 10.1007/s10948-008-0376-2 (cit. on p. 75).
- [95] Rybicki, D., Kohlrantz, J., Haase, J., Greven, M., Zhao, X., Chan, M. K., Dorow, C. J., and Veit, M. J. ‘Electronic spin susceptibilities and superconductivity in $\text{HgBa}_2\text{CuO}_{4+\delta}$ from nuclear magnetic resonance’. In: *Phys. Rev. B* 92 (2015), p. 081115. DOI: 10.1103/PhysRevB.92.081115 (cit. on pp. 1, 73, 75).
- [96] Rybicki, D., Hasse, J., Lux, M., Jurkutat, M., Greven, M., Yu, G., Li, Y., and Zhao, X. ‘ ^{63}Cu and ^{199}Hg NMR study of $\text{HgBa}_2\text{CuO}_{4+\delta}$ single crystals’. 2012. arXiv: 1208.4690v1 (cit. on p. 75).
- [97] Rybicki, D., Jurkutat, M., Reichardt, S., Kapusta, C., and Haase, J. ‘Perspective on the phase diagram of cuprate high-temperature superconductors’. In: *Nat. Commun.* 7 (2016), p. 11413. DOI: 10.1038/ncomms11413 (cit. on p. 74).

- [98] Sadovskii, M. V. ‘Pseudogap in high-temperature superconductors’. In: *Physics-Usp ekhi* 44 (2001), p. 515. DOI: 10.1070/PU2001v044n05ABEH000902 (cit. on p. 76).
- [99] Schrieffer, J. R. and Brooks, J. S., eds. ‘Handbook of High -Temperature Superconductivity: Theory and Experiment’. Springer, 2007. DOI: 10.1007/978-0-387-68734-6 (cit. on p. 75).
- [100] Shastry, B. S. and Sutherland, B. ‘Exact ground state of a quantum mechanical antiferromagnet’. In: *Phys. B* 108 (1981), p. 1069. DOI: 10.1016/0378-4363(81)90838-X (cit. on p. 54).
- [101] Slichter, C. P. ‘Principles of Magnetic Resonance’. Springer-Verlag, Berlin, 1992. DOI: 10.1007/978-3-662-09441-9 (cit. on pp. 5, 108).
- [102] Smith, R. W. and Keszler, D. A. ‘Synthesis, structure, and properties of the orthoborate $\text{SrCu}_2(\text{BO}_3)_2$ ’. In: *J. Solid State Chem.* 93 (1991), p. 430. DOI: 10.1016/0022-4596(91)90316-A (cit. on p. 53).
- [103] Smith, S. A., Palke, W. E., and Gerig, J. T. ‘The Hamiltonians of NMR Part III’. In: *Concepts Magn. Reson.* 5 (1993), p. 151. DOI: 10.1002/cmr.1820050204 (cit. on p. 115).
- [104] Spokas, J. J. and Slichter, C. P. ‘Nuclear Relaxation in Aluminum’. In: *Phys. Rev.* 113 (1959), p. 1462. DOI: 10.1103/PhysRev.113.1462 (cit. on p. 12).
- [105] Springford, M., Challis, L. J., and Karow, H. U. ‘The Scientific Case for a European Laboratory for 100 Tesla Science’. Strasbourg: European Science Foundation, 1998. URL: <http://www.hzdr.de/pls/rois/Cms?p0id=14294> (cit. on p. 2).
- [106] Stern, R., Heinmaa, I., Kuhns, P. L., Reyes, A. P., Moulton, W. G., Dabkowska, H. A., and Gaulin, B. D. ‘HIGH FIELD ^{11}B NMR STUDY OF 1/3 MAGNETIZATION PLATEAU OF 2D QUANTUM SPIN SYSTEM $\text{SrCu}_2(\text{BO}_3)_2$ ’. 2004. URL: <https://legacywww.magnet.fsu.edu/mediacenter/publications/reports/2004annualreport/2004-NHMFL-Report278.pdf> (cit. on pp. 58, 68, 69).
- [107] Stork, H., Bontemps, P., and Rikken, G. ‘NMR in pulsed high-field magnets and application to high- T_c superconductors’. In: *J. Magn. Reson.* 234 (2013), p. 30. DOI: 10.1016/j.jmr.2013.06.005 (cit. on pp. 18, 19).

- [108] Suter, A., Mali, M., Roos, J., and Brinkmann, D. ‘Mixed magnetic and quadrupolar relaxation in the presence of a dominant static Zeeman Hamiltonian’. In: *J.Phys. Condens. Matter* 10 (1998), p. 5977. DOI: 10.1088/0953-8984/10/26/022 (cit. on p. 40).
- [109] Taillefer, L. ‘Fermi surface reconstruction in high- T_c superconductors’. In: *J. Phys. Condens. Matter* 21 (2009), p. 164212. DOI: 10.1088/0953-8984/21/16/164212 (cit. on p. 78).
- [110] Takigawa, M., Horvatić, M., Waki, T., Krämer, S., Berthier, C., Lévy-Bertrand, F., Sheikin, I., Kageyama, H., Ueda, Y., and Mila, F. ‘Incomplete Devil’s Staircase in the Magnetization Curve of $\text{SrCu}_2(\text{BO}_3)_2$ ’. In: *Phys. Rev. Lett.* 110 (2013), p. 067210. DOI: 10.1103/PhysRevLett.110.067210 (cit. on pp. 57, 58, 68).
- [111] Takigawa, M., Kodama, K., Horvatić, M., Berthier, C., Kageyama, H., Ueda, Y., Miyahara, S., Becca, F., and Mila, F. ‘The 1/8-magnetization plateau state in the 2D quantum antiferromagnet $\text{SrCu}_2(\text{BO}_3)_2$: Spin superstructure, phase transition, and spin dynamics studied by high-field NMR’. In: *Phys. B Condens. Matter* 346-347 (2004), p. 27. DOI: 10.1016/j.physb.2004.01.014 (cit. on pp. 58, 68).
- [112] Takigawa, M., Matsubara, S., Horvatić, M., Berthier, C., Kageyama, H., and Ueda, Y. ‘NMR Evidence for the Persistence of a Spin Superlattice Beyond the 1/8 Magnetization Plateau in $\text{SrCu}_2(\text{BO}_3)_2$ ’. In: *Phys. Rev. Lett.* 101 (2008), p. 037202. DOI: 10.1103/PhysRevLett.101.037202 (cit. on pp. 58, 63, 68).
- [113] Takigawa, M., Reyes, A. P., Hammel, P. C., Thompson, J. D., Heffner, R. H., Fisk, Z., and Ott, K. C. ‘Cu and O NMR studies of the magnetic properties of $\text{YBa}_2\text{Cu}_3\text{O}_{6.63}$ ($T_c = 62\text{ K}$)’. In: *Phys. Rev. B* 43 (1991), p. 247. DOI: 10.1103/PhysRevB.43.247 (cit. on p. 76).
- [114] Timusk, T. and Statt, B. ‘The pseudogap in high-temperature superconductors: an experimental survey’. In: *Reports Prog. Phys.* 62 (1999), p. 61. DOI: 10.1088/0034-4885/62/1/002 (cit. on p. 76).
- [115] Townes, C. H., Herring, C., and Knight, W. D. ‘The Effect of Electronic Paramagnetism on Nuclear Magnetic Resonance Frequencies in Metals’. In: *Phys. Rev.* 77 (1950), p. 852. DOI: 10.1103/PhysRev.77.852 (cit. on pp. 1, 10).
- [116] Tranquada, J. M. ‘Modulated spin and charge densities in cuprate superconductors’. In: *Phys. B* 241-243 (1998), p. 745. DOI: 10.1016/S0921-4526(97)00711-4 (cit. on p. 78).

- [117] Van Vleck, J. ‘The Dipolar Broadening of Magnetic Resonance Lines in Crystals’. In: *Phys. Rev.* 74 (1948), p. 1168. DOI: 10.1103/PhysRev.74.1168 (cit. on p. 107).
- [118] Varma, C. ‘High-temperature superconductivity: Mind the pseudogap’. In: *Nature* 468 (2010), p. 184. DOI: 10.1038/468184a (cit. on pp. 3, 77).
- [119] Wagner, J. L., Radaelli, P. G., Hinks, D. G., Jorgensen, J. D., Mitchell, J. F., Dabrowski, B., Knapp, G. S., and Beno, M. A. ‘Structure and superconductivity of $\text{HgBa}_2\text{CuO}_{4+\delta}$ ’. In: *Phys. C Supercond.* 210 (1993), p. 447. DOI: 10.1016/0921-4534(93)90989-4 (cit. on p. 74).
- [120] Walstedt, R. E. ‘The NMR Probe of High- T_c Materials’. 1 ed. Springer, 2007. DOI: 10.1007/978-3-540-75565-4 (cit. on p. 75).
- [121] Walt, S. van der, Colbert, S. C., and Varoquaux, G. ‘The NumPy Array: A Struture for Efficient Numerical Computation’. In: *Comput. Sci. & Engeneering* 13 (2011), p. 22. DOI: 10.1109/MCSE.2011.37 (cit. on p. 33).
- [122] Wang, Y. and Chubukov, A. ‘Charge-density-wave order with momentum $(2Q, 0)$ and $(0, 2Q)$ within the spin-fermion model: Continuous and discrete symmetry breaking, preemptive composite order, and relation to pseudogap in hole-doped cuprates’. In: *Phys. Rev. B* 90 (2014), p. 1. DOI: 10.1103/PhysRevB.90.035149 (cit. on p. 3).
- [123] Watanabe, T., Fujii, T., and Matsuda, A. ‘Pseudogap in $\text{Bi}_2\text{Sr}_2\text{CaCu}_2\text{O}_{8+\delta}$ Studied bz Measuring Anisotropic Susceptibilities and Out-of-Plane Transport’. In: *Phys. Rev. Lett.* 84 (2000), p. 5848. DOI: 10.1103/PhysRevLett.84.5848 (cit. on p. 77).
- [124] Weickert, F., Meier, B., Zherlitsyn, S., Herrmannsdörfer, T., Daou, R., Nicklas, M., Haase, J., Steglich, F., and Wosnitza, J. ‘Implementation of specific-heat and NMR experiments in the 1500 ms long-pulse magnet at the Hochfeld-Magnetlabor Dresden’. In: *Meas. Sci. Technol.* 23 (2012), p. 105001. DOI: 10.1088/0957-0233/23/10/105001 (cit. on p. 16).
- [125] Wolf, F., Kline, D., and Story, H. ‘ ^{93}Nb and ^{23}Na NMR in Polycrystalline Sodium Niobate’. In: *J. Chem. Phys.* 53 (1970), p. 3538. DOI: 10.1063/1.1674529 (cit. on p. 8).
- [126] Wosnitza, J., Bianchi, A., Freudenberger, J., Haase, J., Herrmannsdörfer, T., Kozlova, N., Schultz, L., Skourski, Y., Zherlitsyn, S., and Zvyagin, S. ‘Dresden pulsed magnetic field facility’. In: *J. Magn. Magn. Mater.* 310 (2007), p. 2728. DOI: 10.1016/j.jmmm.2006.10.1115 (cit. on pp. 16, 17).

- [127] Wu, T., Mayaffre, H., Krämer, S., Horvatić, M., Berthier, C., Hardy, W. N., Liang, R., Bonn, D. A., and Julien, M.-H. ‘Magnetic-field-induced charge-stripe order in the high-temperature superconductor $\text{YBa}_2\text{Cu}_3\text{O}_y$ ’. In: *Nature* 477 (2011), p. 191. DOI: 10.1038/nature10345 (cit. on p. 78).
- [128] Wu, T., Mayaffre, H., Krämer, S., Horvatić, M., Berthier, C., Hardy, W., Liang, R., Bonn, D., and Julien, M.-H. ‘Incipient charge order observed by NMR in the normal state of $\text{YBa}_2\text{Cu}_3\text{O}_y$ ’. In: *Nat. Commun.* 6 (2015), p. 6438. DOI: 10.1038/ncomms7438 (cit. on pp. 1, 3).
- [129] Xiao, H., Ma, Y., Lv, Y., Ding, T., Zhang, S., Hu, F., Li, L., and Pan, Y. ‘Development of a high-stability flat-top pulsed magnetic field facility’. In: *IEEE Trans. Power Electron.* 29 (2014), p. 4532. DOI: 10.1109/TPEL.2013.2285125 (cit. on p. 16).
- [130] Xu, Y., Pi, H., Ren, T., Yang, Y., Ding, H., Peng, T., and Li, L. ‘Design of a Multipulse High-Magnetic-Field System Based on Flywheel Energy Storage’. In: *IEEE Trans. Appl. Supercond.* 26 (2016), p. 1. DOI: 10.1109/TASC.2016.2542340 (cit. on p. 16).
- [131] Zhang, F. C. and Rice, T. M. ‘Effective Hamiltonian for the superconducting Cu oxides’. In: *Phys. Rev. B* 37 (1988), p. 3759. DOI: 10.1103/PhysRevB.37.3759 (cit. on p. 75).
- [132] Zhang, Z. and Kühne, H. ‘Private communication’. 2016 (cit. on p. 63).
- [133] Zhao, X., Yu, G., Cho, Y.-C., Chabot-Couture, G., Barišić, N., Bourges, P., Kaneko, N., Li, Y., Lu, L., Motoyama, E. M., Vajk, O. P., and Greven, M. ‘Crystal Growth and Characterization of the Model High-Temperature Superconductor $\text{HgBa}_2\text{CuO}_{4+\delta}$ ’. In: *Adv. Mater.* 18 (2006), p. 3243. DOI: 10.1002/adma.200600931 (cit. on p. 78).
- [134] Zheng, G., Katayama, K., Nishiyama, M., Kawasaki, S., Nishihagi, N., Kimura, S., Hagiwara, M., and Kindo, K. ‘Spin-Echo NMR in Pulsed High Magnetic Fields up to 48 T’. In: *J. Phys. Soc. Japan* 78 (2009), p. 095001. DOI: 10.1143/JPSJ.78.095001 (cit. on pp. 2, 17).

APPENDIX A

Dynamics of interacting spin systems

Nuclear spin systems are an ideal test bed for the dynamics of large interacting spin systems with wide ranges of internal interactions and coupling to the external environment. For example, the benchmark compound CaF_2 offers characteristic time constants T_1 and T_2 that differ by six orders of magnitude [70]. For the theoretical treatment, a large number of interacting spins has to be considered and often approximations are applied. In the following, experiments aimed at the discovery of additional resonances are presented. These non-secular resonances were predicted to exist in the presence of relatively large RF fields B_{RF} [59, 60]. Depending on B_{RF}/B_0 the non-secular parts of the dipolar Hamiltonian, i.e., those that do not conserve the total magnetization, are predicted to become relevant again.

A.1 Non-secular resonances in dipolar coupled spin systems

First theoretical discussions and experimental verifications of a nuclear spin systems with dipolar interactions in the presence of a strong magnetic field \mathbf{B}_0 were presented by Van Vleck [117].

As discussed in Ch. 2, the coupling of the dipolar moments of different spins j and k is described by the Hamiltonian \mathcal{H}_{DD} (\mathbf{r}_{jk} is the vector connecting both spins, θ_{jk} the angle between \mathbf{r}_{jk} and \mathbf{B}_0),

$$\mathcal{H}_{\text{DD}} = \sum_{j,k} \frac{\hbar^2 \gamma_j \gamma_k}{2} \left[\frac{\hat{\mathbf{I}}_j \cdot \hat{\mathbf{I}}_k}{r_{jk}^3} + 3 \frac{(\hat{\mathbf{I}}_j \cdot \mathbf{r}_{jk})(\hat{\mathbf{I}}_k \cdot \mathbf{r}_{jk})}{r_{jk}^5} \right]. \quad (\text{A.1})$$

The expression can be rewritten as the (*dipolar alphabet*) using six different terms, each

with a characteristic combination of spin operators [2, 101],

$$\mathcal{H}_{\text{DD}} = \sum_{j,k} \frac{\hbar^2 \gamma_j \gamma_k}{2r_{jk}^3} [A_{jk} + B_{jk} + C_{jk} + D_{jk} + E_{jk} + F_{jk}], \quad (\text{A.2})$$

with

$$A_{jk} = \hat{I}_{jz} \hat{I}_{kz} (1 - 3 \cos^2 \theta_{jk}), \quad (\text{A.3})$$

$$B_{jk} = -\frac{1}{4} [\hat{I}_j^+ \hat{I}_k^- + \hat{I}_j^- \hat{I}_k^+] (1 - 3 \cos^2 \theta_{jk}), \quad (\text{A.4})$$

$$C_{jk} = -\frac{3}{2} [\hat{I}_j^+ \hat{I}_{kz} + \hat{I}_{jz} \hat{I}_k^+] \sin \theta_{jk} \cos \theta_{jk} e^{-i\phi_{jk}}, \quad (\text{A.5})$$

$$D_{jk} = -\frac{3}{2} [\hat{I}_j^- \hat{I}_{kz} + \hat{I}_{jz} \hat{I}_k^-] \sin \theta_{jk} \cos \theta_{jk} e^{-i\phi_{jk}}, \quad (\text{A.6})$$

$$E_{jk} = -\frac{3}{4} \hat{I}_j^+ \hat{I}_k^+ \sin^2 \theta_{jk} e^{-2i\phi_{jk}}, \quad (\text{A.7})$$

$$F_{jk} = -\frac{3}{4} \hat{I}_j^- \hat{I}_k^- \sin^2 \theta_{jk} e^{2i\phi_{jk}}. \quad (\text{A.8})$$

The dominance of the Zeeman terms of the magnetic field justifies a truncation of some parts of \mathcal{H}_{DD} such that only A_{jk} and, in case of like spins, B_{jk} remain (in the relevant case of like spins).

Later work by Redfield included perturbations from an oscillating, linear polarized, magnetic field $2B_{\text{RF}}(t)$ (with a frequency ω_{RF}) in the discussion. The time-dependent magnetic field is then given by

$$\mathbf{B}(t) = (2B_{\text{RF}} \cos \omega_{\text{RF}} t, 0, B_0) \quad (\text{A.9})$$

and leads to an additional second truncation of the dipolar terms, keeping only the terms that commute with the Zeeman Hamiltonian for the effective magnetic field in the rotating frame [92].

However, in a recent work, Kropf and Fine argued that this procedure with two consecutive truncation steps is not always valid in the case of a large B_{RF} [59]. Instead, for certain frequencies ω_{ns} , different from the Larmor frequency ω_{L} , additional non-secular resonances were predicted to exist at rational multiples of ω_{e} ,

$$\omega_{\text{ns}} = \pm \frac{p}{q} \omega_{\text{e}}, \quad (\text{A.10})$$

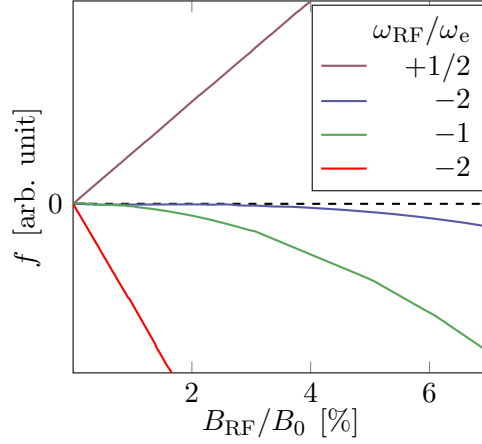


Figure A.1: Strength f of the non-secular Hamiltonian for different frequencies $\omega_{\text{RF}}/\omega_e$ (see legend) of the oscillating magnetic field B_{RF} . Note that the two curves for $\omega_{\text{RF}}/\omega_e = -2$ correspond to $\omega_{\text{RF}} = -2\gamma B_0$ and $\omega_{\text{RF}} = -2\gamma B_0/3$. Data reproduced from Ref. [60].

with the gyromagnetic ratio γ of the nucleus and

$$\omega_e = \gamma \sqrt{\gamma^2 B_{\text{RF}}^2 + (\gamma B_0 + \omega_{\text{RF}})^2}. \quad (\text{A.11})$$

At these frequencies ω_{ns} , the non-secular Hamiltonian \mathcal{H}_{ns} , given by the terms C_{jk} to F_{jk} in Eq. (A.2), does not vanish. While the explicit form of \mathcal{H}_{ns} depends on ω_{ns} , all corresponding prefactors $f(\omega_{\text{ns}})$, i.e., the interaction strength of \mathcal{H}_{ns} , increase with the ratio B_{RF}/B_0 , cf. Fig. A.1. However, in common NMR experiments, B_0 is typically about three orders of magnitude larger than B_{RF} . Decreasing B_0 reduces the Larmor frequency, equilibrium magnetization, and thus the signal intensity. On the other hand, B_{RF} can be increased by applying a higher RF power level or by using a smaller RF coil.

Table A.1: Estimates for the secular local magnetic field $B_{\text{loc}}^{\text{sec}}$ and non-secular local magnetic field $B_{\text{loc}}^{\text{ns}}$ in CaF_2 for three different crystal orientations (relative to the applied static magnetic field \mathbf{B}_0) for two sets of field values B_0 and B_{RF} . Data reproduced from Ref. [60].

	Optimistic choice			Conservative choice		
B_0	250 mT (≈ 10 MHz)			1 T (≈ 40 MHz)		
B_{RF}	10 mT (≈ 0.4 MHz)			3 mT (≈ 0.1 MHz)		
B_{RF}/B_0 [%]	4			0.1		
B_0 orientation	[100]	[110]	[111]	[100]	[110]	[111]
$B_{\text{loc}}^{\text{sec}}$	0.3 mT	0.18 mT	0.12 mT	0.3 mT	0.18 mT	0.12 mT
$B_{\text{loc}}^{\text{ns}}$	0.007 mT	0.013 mT	0.014 mT	0.0005 mT	0.0010 mT	0.0011 mT
T_1^{ns}	0.024 s	0.0042 s	0.0024 s	4.8 s	0.72 s	0.39 s

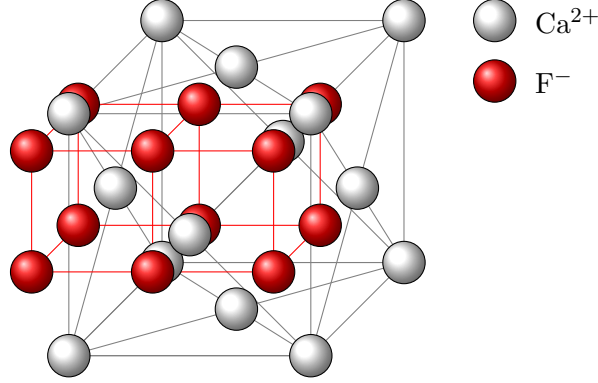


Figure A.2: Crystal structure of CaF_2 . The ^{19}F nuclei form a simple cubic lattice and have an abundance of 100 %.

Regarding the dependence on B_{RF}/B_0 , the resonance with $\omega = -2\omega_e$ promises the best conditions for success in a proposed double resonance experiment [60]. The non-secular resonance is predicted to produce an anomalous longitudinal relaxation, i.e., a depolarization of the sample caused by the terms that do not conserve the spin polarization. Estimates for the time constant T_1^{ns} describing the relaxation process are reproduced in Tab. A.1 for two sets of B_0 and B_{RF} and three different crystal orientations of CaF_2 . This material has often been used as a benchmark compound to test theories on dipolar coupled systems using ^{19}F NMR [22, 43, 70] because the ^{19}F nuclei have an abundance of 100 % and a high gyromagnetic ratio of $\gamma = 251.815 \times 10^6 \text{ rad s}^{-1} \text{ T}$ [64]. The crystal structure of CaF_2 arranges the fluorine nuclei on a simple cubic lattice, cf. Fig. A.2.

A.2 Experimental

Instead of the double resonance experiment that was proposed in Ref. [60], the following experiments use field cycling to test the predictions. As sketched in Fig. A.3, the sample relaxes for a time $t_{\text{relax}} \gg T_1$ at a field B_i . Afterward, three consecutive rectangular RF pulse (durations $t_{\text{low}}/3$) with carrier frequencies $\omega_{\text{RF}} - \Delta\omega$, ω_{RF} , and $\omega_{\text{RF}} + \Delta\omega$ are applied (with $\Delta\omega = 10 \text{ kHz}$). Note that the Larmor frequency for B_i

$$\omega_{\text{L}} = \gamma B_i \approx \frac{1}{2} \omega_{\text{RF}} \quad (\text{A.12})$$

is about one half of the carrier frequency and thus close to the predicted non-secular resonance frequency. After the RF pulse is finished, the field is increased (within a time frame t_{sweep}) to B_{high} where $\omega_{\text{L}} = \omega_{\text{RF}}$. At B_{high} , a $\pi/2$ pulse is used to excite a FID that measures the longitudinal magnetization M_z . In order to prevent T_1 relaxation to

cover a possible effect, the following two conditions have to be met,

$$t_{\text{relax}} \gg T_1, \quad (\text{A.13})$$

$$t_{\text{low}} + t_{\text{sweep}} \lesssim T_1. \quad (\text{A.14})$$

The experiment is repeated for different values of B_i . Analyzing the signal intensity as a function of B_i should then show a decrease at the non-secular resonance. The allowed difference in two consecutive field values B_{i+1} and B_i is set by the dipolar linewidth ω_{DD} [60],

$$B_{i+1} - B_i < \frac{\omega_{\text{DD}}}{\gamma}. \quad (\text{A.15})$$

Experiments were performed on a $1 \text{ mm} \times 1 \text{ mm} \times 10 \text{ mm}$ CaF_2 single crystal (from *Mateck*, Germany, $T_1 \approx 80 \text{ s}$) in a sweepable 16 T *Oxford Instruments* magnet with an integrated flow cryostat. A crystal orientation with $[110] \parallel \mathbf{B}_0$ was chosen and confirmed with the nodes of the FID. The sample was placed in a solenoid RF coil with a high filling factor that was soldered to a home-built probehead. Additional capacitors (parallel to tuning and matching capacitors) were introduced to the RF tank circuit to decrease the resonance frequency to $\omega_{\text{RF}}/2\pi = 18.822 \text{ MHz}$. The pulses at B_i were applied for 300 ms each (at frequencies 18.812 MHz, 18.822 MHz, and 18.832 MHz).

At a temperature of $T = 150 \text{ K}$, a quality factor of $Q \approx 100$ was found. ^{19}F FIDs were acquired with a *Tecmag Apollo* spectrometer as I/Q-demodulated traces with a sampling

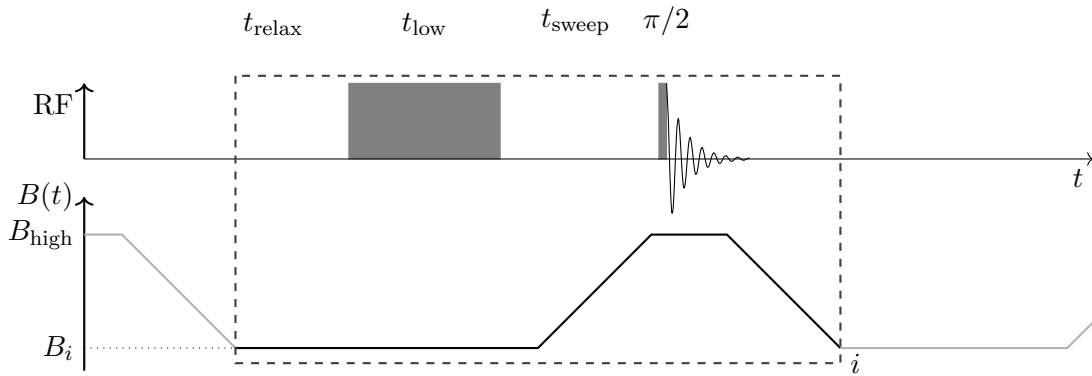


Figure A.3: Field cycling experiment for the detection of a non-secular resonance. The sample is equilibrated for a duration of t_{relax} at a field B_i . Then, three consecutive RF pulses are applied for a total duration of t_{low} . Within a time frame of t_{sweep} , the field is increased and a $\pi/2$ pulse is used to measure the sample magnetization.

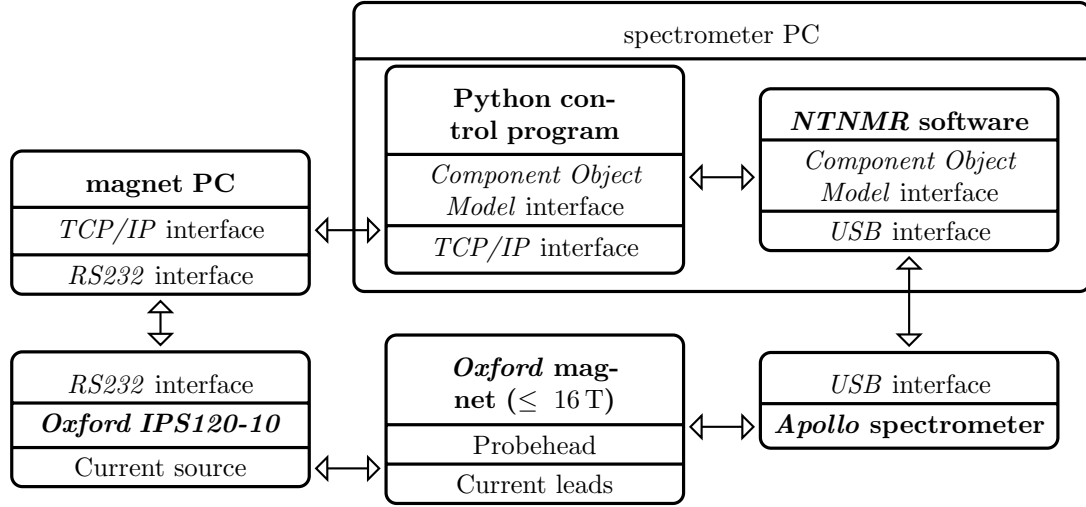


Figure A.4: Setup for field cycling experiments. A small *Python* program on the spectrometer controls the NMR software via a *Component Object Model* interface. The magnetic field is set using another computer that is connected to the *IPS120-10* power supply.

rate of 1 MHz.

The field cycling experiments were conducted using a small *Python* program running on the spectrometer PC, cf. Fig. A.4. The NMR excitation and data acquisition were performed by the *NTNMR* software via a *Component Object Model* interface.

A.3 Results and discussion

Nutation

In a first step, a nutation experiment was performed to obtain an estimate of the RF field strength. A typical FID and the associated FT spectrum after baseline correction, left shift, and manual phase correction are shown in Fig. A.5.a and Fig. A.5b. The intensities I for different pulse lengths τ are obtained as the sum of the real part of the FT spectra, cf. Fig. A.5c.

A sinusoidal function

$$I(\tau) = A \sin(\gamma B_{\text{RF}} \tau + \phi_0) \quad (\text{A.16})$$

with an initial phase $\phi_0 = -23.8^\circ$ describes $I(\tau)$ in good approximation, cf. orange curve in Fig. A.5c. This $\phi_0 \neq 0$ is assumed to be caused by the time constant τ_Q of the RF tank circuit. Due to the low resonance frequency and the high quality factor a value of $\tau_Q \approx 5 \mu\text{s}$ is expected.

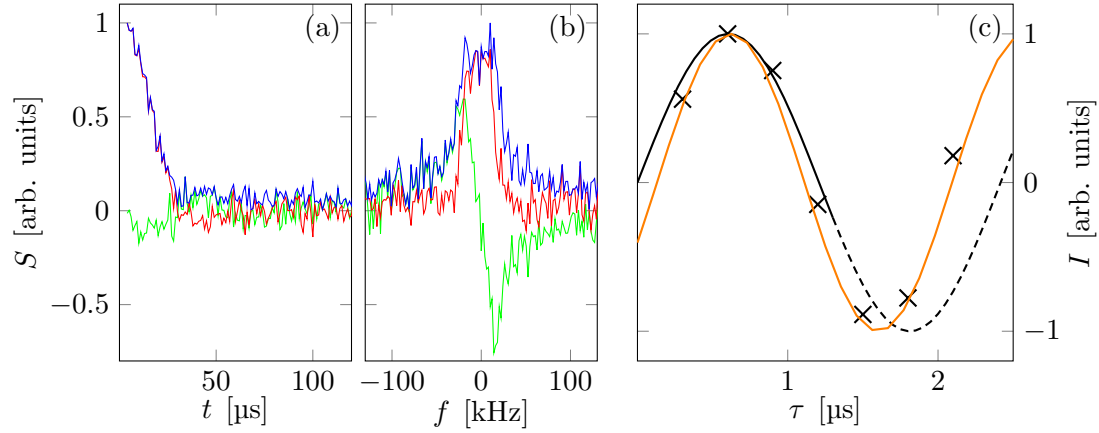


Figure A.5: Nutation experiment for the determination of B_{RF} . (a, b) Real part (red), imaginary part (green), and magnitude (blue) of FID and its FT for a RF pulse length $\tau = 0.6 \mu\text{s}$. (c) Intensities as a function of pulse length τ (sum over real part of the FT from -40 kHz to 40 kHz). Curves are sinusoidal functions with initial phases $\phi_0 = 0^\circ$ (black) and $\phi_0 = -23.8^\circ$ (orange).

As a consequence, the nutation can only be used to provide a lower estimate for the RF field with

$$B_{\text{RF}} \geq 12 \text{ mT}. \quad (\text{A.17})$$

Non-secular resonance

Using the estimate for the RF field from the nutation, the ratio magnetic fields can be projected,

$$\frac{B_{\text{RF}}}{B_0} \approx 5 \%, \quad (\text{A.18})$$

thus, close to the optimistic case in Tab. A.1. Therefore, a time constant T_1^{ps} in order of 4 ms is expected, giving one order of magnitude room in error for the estimates.

Fig. A.6 shows the observed intensities I as a function of the magnetic field that was applied during the long pulse, cf. Fig. A.3. An increase of I is found for higher values of B_i . This is expected due to the field dependence of the equilibrium magnetization. However, around the expected value $B_i = 235 \text{ mT}$, no effect is found.

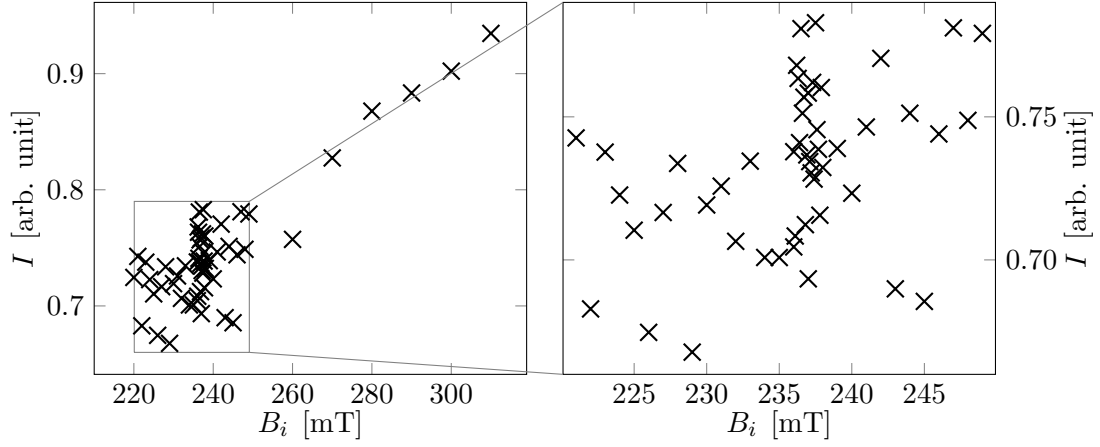


Figure A.6: Observed intensities as a function of the applied magnetic field B_i during the long RF pulses. Values of B_i correspond to the magnetic field set using the power supply based on the ratio of Larmor frequency and field setting during the FID detection.

A.4 Conclusion

Even though a sufficient field ratio B_{RF}/B_0 according to the predictions from Ref. [60] was found, no effect was detected. Possible reasons for failure include a non-linear dependence of B_i as a function of the set value or too large steps between the used values of B_i . As a consequence, further experiments are needed to answer the question whether the predicted non-secular resonance exists.

APPENDIX B

Simulation of an adiabatic inversion in the rotating frame

While there are different ways to understand the action of a sequence of RF pulses on a spin system, the description using the density operator $\hat{\rho}$ is among the most elegant approaches. A brief overview on this formalism can be found in Ref. [103]. For a system with the eigenstates $|\psi_i\rangle$ and the probabilities p_i to be in those states (with $\sum_i p_i = 1$), it is given by

$$\hat{\rho} = \sum_i p_i |\psi_i\rangle \langle \psi_i|. \quad (\text{B.1})$$

The expectation value $\langle A \rangle$ of an observable \hat{A} can then be obtained using the trace operation according to

$$\langle A \rangle = \text{tr} [\hat{\rho} \hat{A}]. \quad (\text{B.2})$$

While the equilibrium density operator $\hat{\rho}_0$ is given by

$$\hat{\rho}_0 = \exp \left(\frac{\hat{H}}{k_B T} \right) / \text{tr} \left[\exp \left(\frac{\hat{H}}{k_B T} \right) \right] \approx \frac{\hat{1} + \hat{H}/k_B T}{2I + 1}, \quad (\text{B.3})$$

it is often more convenient to use the simplified density operator

$$\hat{\rho}'_0 = \hat{I}_z \quad (\text{B.4})$$

that marks the unnormalized deviation from the unity operator $\hat{1}$ (all relevant observables vanish for it).

The time-evolution of the system can be described using the time-evolution operator $\hat{U}(t, t_0)$ and its adjoint $\hat{U}^\dagger(t, t_0)$ according to

$$\rho(t) = \hat{U}(t, t_0)\rho(t_0)\hat{U}^\dagger(t, t_0), \quad (\text{B.5})$$

$$\hat{U}(t, t_0) = \exp \left[-\frac{i}{\hbar} \int_{t_0}^t \hat{H}(t') dt' \right]. \quad (\text{B.6})$$

In the case of a time-independent Hamiltonian, the integral for $\hat{U}(t)$ becomes trivial, and one finds

$$\hat{U}(t, t_0) = \exp \left[-\frac{i}{\hbar} \hat{H} (t - t_0) \right]. \quad (\text{B.7})$$

However, the integral in Eq. (B.6) is not necessarily as trivial for time-dependent Hamiltonians. While an analytical solution can often be found, simple numerical simulations can already shed light on the outcome of a given experiment. For a short time step Δt , the time-evolution operator and the density operator starting from t can be approximated using

$$\hat{U}(t + \Delta t, t) = \exp \left[-\frac{i}{\hbar} \int_t^{t+\Delta t} \hat{H}(t') dt' \right] = \exp \left[-\frac{i}{\hbar} \hat{H}(t) \Delta t \right], \quad (\text{B.8})$$

$$\rho(t + \Delta t) = \exp \left[-\frac{i}{\hbar} \hat{H}(t) \Delta t \right] \rho(t) \exp \left[\frac{i}{\hbar} \hat{H}(t) \Delta t \right]. \quad (\text{B.9})$$

In calculations, a description using an interaction picture with the time-independent Hamiltonian separated off, corresponding to the rotating frame with the Larmor frequency, can be advantageous.

We will now use the density operator to briefly show an adiabatic inversion of a free spin in a time-dependent field qualitatively. More systematic studies can be found in literature, e.g., in Refs. [7, 29].

For a linear time-dependence of $B(t)$, the Hamiltonian in the presence of a linear polarized RF field with an amplitude B_{RF} and a frequency ω in x direction is given by

$$\hat{H}(t) = \gamma B(t) \hat{I}_z + \gamma B_{\text{RF}} \sin(\omega t) \hat{I}_x. \quad (\text{B.10})$$

For the simulation according to Eq. (B.9), we use the Schrödinger picture for a spin 1/2

system with the gyromagnetic ratio $\gamma = 26.7519 \times 10^7 \text{ rad s}^{-1} \text{ T}$ of ^1H , a magnetic field close to 1 T, i.e., $\omega = \gamma \cdot 1 \text{ T}$, and a time step of $\Delta t = 2 \text{ ns}$. Furthermore, we choose the simplified version $\rho(t_0 = 0) = \hat{I}_z$ for the initial density operator.

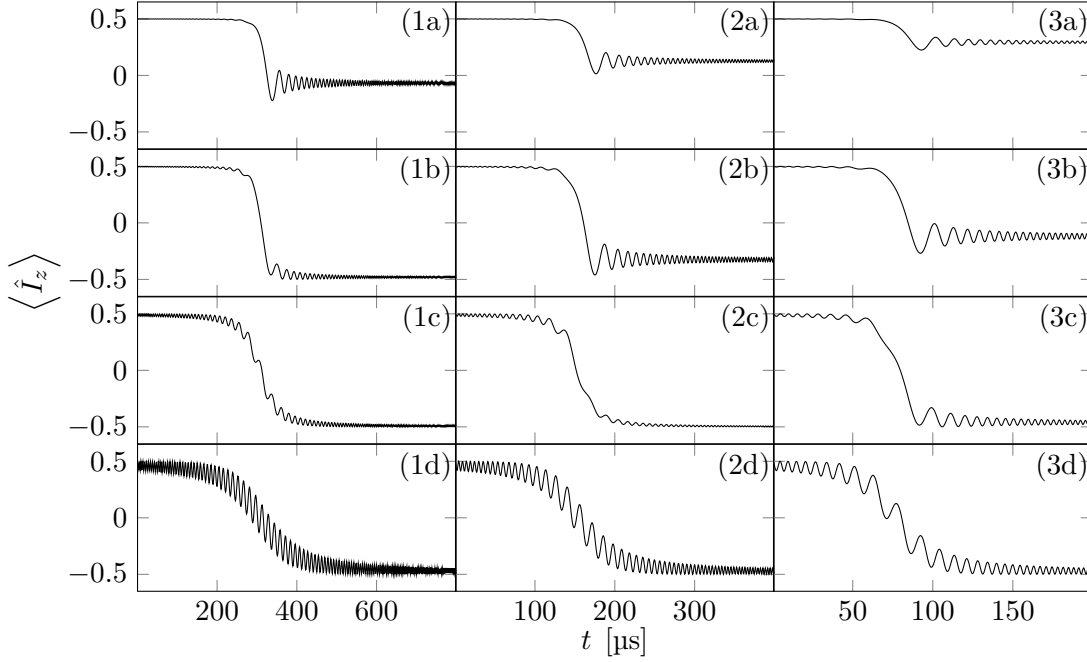


Figure B.1: Simulated expectation values for \hat{I}_z in a linear changing magnetic field $B_0(t)$ starting at 995 mT increasing to 1008 mT under the presence of a weak RF field with different amplitudes for γB_{RF} of 100 krad s⁻¹ (a), 200 krad s⁻¹ (b), 400 krad s⁻¹ (c), 800 krad s⁻¹ (d) and different sweep rates of 13 mT (equivalent to 0.5 MHz) per 800 μs (1), 400 μs (2), and 200 μs (3).

Fig. B.1 shows the time-dependent expectation value of \hat{I}_z during the application of the inversion field with a rectangular shape for different amplitudes of B_{RF} and different field sweep rates. Here, the need for a sufficiently large B_{RF} becomes apparent since the inversion is incomplete at all sweep rates for the weakest RF field of $\gamma B_{\text{RF}} = 100 \text{ krad s}^{-1}$ (a), and even at a field of $\gamma B_{\text{RF}} = 200 \text{ krad s}^{-1}$, the inversion is inadequate at the higher sweep rates (2b, 3b).

On the other hand, a weaker RF field can be beneficial if the time available after the crossing of the Larmor condition is limited: (1b) already shows an almost complete inversion at $t = 400 \mu\text{s}$, while (1d) exhibits a modulation at the same point in time that only vanishes at a later time corresponding to a larger difference in between the Larmor frequency and the frequency of the RF field. This problem can be mitigated using an RF field with a modulated amplitude.

APPENDIX C

Radio frequency circuits

To verify Eq. (C.1), ^1H intensity measurements on tap water were performed.

C.1 Experimental

A drop of tap water was put in a short cut from a NMR tube and sealed with hot-melt adhesive. This tube was placed into a tight RF coil that was part of a resonance circuit equivalent to Fig. 2.4 on a home-built probe. Experiments were performed in a sweepable *Oxford Research* 16 T magnet.

Using a spectrum analyser, the resonator was tuned and matched to a frequency of $f_0 = 110.7$ MHz and consecutively the -7 dB bandwidth $\text{BW}_{-7\text{dB}} = 0.84$ MHz was determined. Using a setup including a Python program on the spectrometer PC that originally was intended for the acquisition of broad band spectra using field sweeps (see Fig. A.4), the static magnetic field B_0 was set to different values B_0^i and NMR experiments were conducted at each field. Here, a nutation experiment with a fixed excitation pulse length of $\tau = 50$ μs and different power levels in 1 dB steps was carried out. The carrier frequency was set to the expected Larmor frequency for each field B_0^i .

C.2 Results and discussions

Fig. C.1 shows the obtained normalized intensities (absolute values) for different pulse power levels at different fields B_0^i . The local maxima at the highest attenuation values correspond to a $\pi/2$ pulse. Due to the mismatch of the carrier frequency of the pulses and the RF resonator, not all power is absorbed by the probe. Thus, the maxima shift to lower attenuation values which correspond to a larger power level of the excitation pulse. The symbols in Fig. C.2 shows the maxima of the nutation curves as a function of the

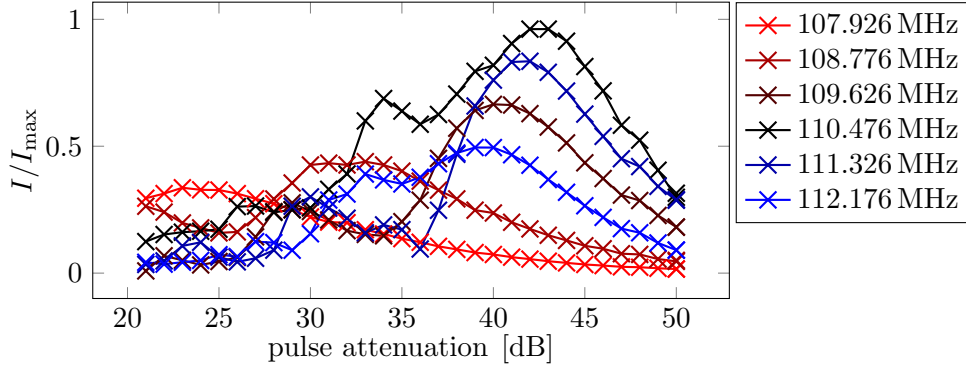


Figure C.1: Power nutation curves at different Larmor frequencies (not all shown). A higher attenuation value correspond to a lower RF pulse power.

Larmor frequency. Using the quality factor $Q_{\text{loaded}} = f_0/2\text{BW}$ for the loaded resonator, we find a good agreement with the expected values (solid black curve)

$$g(\omega) = \frac{\omega_0}{\omega} \frac{1}{\sqrt{Q^2 \varepsilon^2 + 1}}, \quad (\text{C.1})$$

and a clear deviation from the values for the $Q = f_0/\text{BW}$ measured with the spectrum analyser (dashed gray curve).

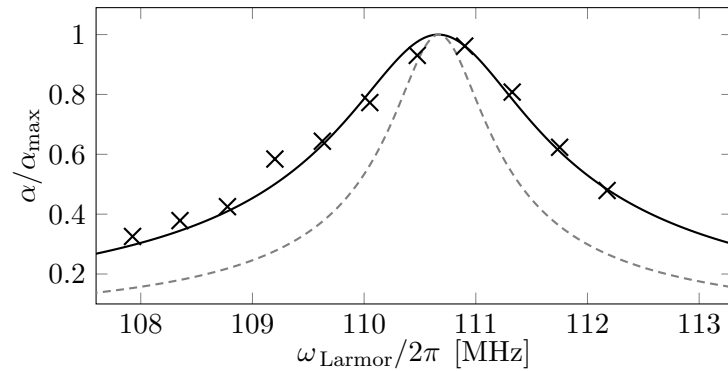


Figure C.2: Intensity variation due to off-resonance detection. Symbols are observed intensities. Curves are according to Eq. (??) with $Q = Q_{\text{loaded}}$ (solid black curve) and $Q = f_0/\text{BW} = 2Q_{\text{loaded}}$ (dashed gray curve).

APPENDIX D

Modification of pulse field spectrometer for T_1 measurements

A signal path with changeable attenuation was added to the spectrometer, see Fig. D.1.

The pulse sequence for T_1 measurements using adiabatic inversions is shown in Fig. D.2, cf. Fig. 5.8. Furthermore, a function to read pulse sequences from simple *XML* files, cf. Lis. D.2, was added to the *LabVIEW* control program that conducts the experiments. In order to facilitate the generation of the corresponding input files, a small *Python* script was implemented. Lis. D.1 shows the usage for the sequence shown in Fig. D.2.

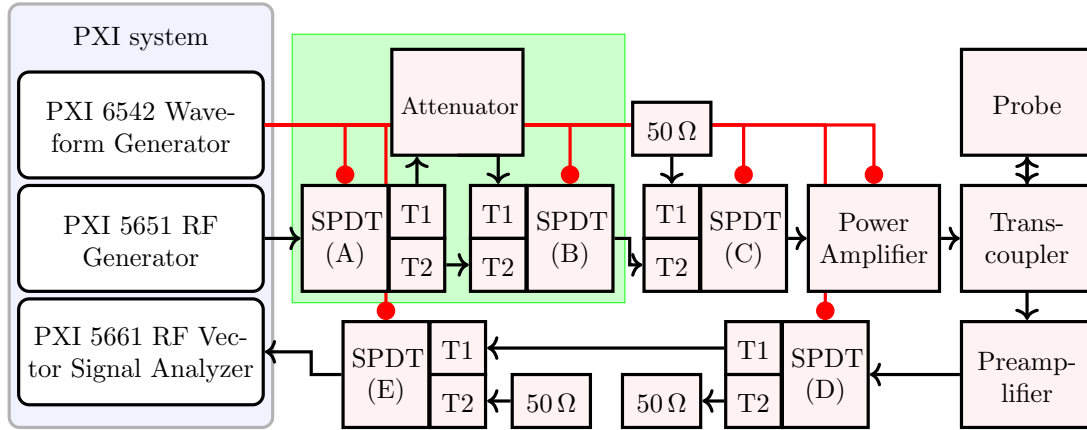


Figure D.1: Schematic of the pulsed field spectrometer based on a National Instruments PXI system [69, 71]. The waveform generator acts as a pulse programmer, that can guide the signal from the frequency source directly to the power amplifier or through a passive attenuator using a set of single pole, double throw (SPDT) switches (green box.). Furthermore, it gates the power amplifier and controls a pair of switches that protect the receiver during the pulse.

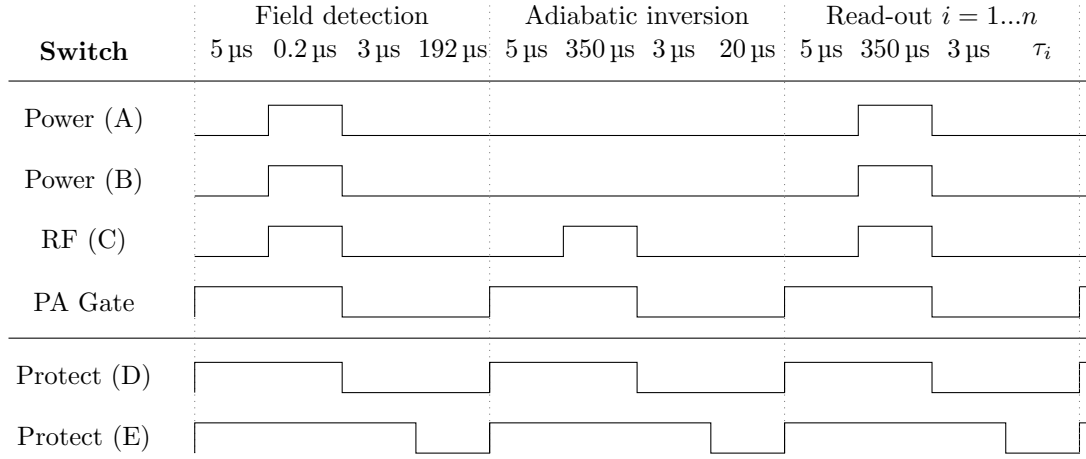


Figure D.2: Sequence of TTL output values for T_1 measurements with an adiabatic inversion. Each pulse is followed by an acquisition window and consist of four steps.

```

1 pp=pulseProgram()
2
3 # list of acquisition times after read-out pulses
4 tauL=[50e-6,70e-6,100e-6]
5
6 # field detection
7 pp.addUnblank(5e-6)
8 pp.addRFHigh(200e-9)
9 pp.addRingDown(3e-6)
10 pp.addDigitize(192e-6)
11
12 # adiabatic inversion
13 pp.addUnblank(5e-6)
14 pp.addRFLow(350e-6)
15 pp.addRingDown(3e-6)
16 pp.addDigitize(20e-6)
17
18 # read-out pulses
19 for tau in tauL:
20     pp.addUnblank(5.1e-6)
21     pp.addRFHigh(2e-7)
22     pp.addRingDown(2.4e-6)
23     pp.addDigitize(tau)

```

Listing D.1: Usage of *Python* script for pulse sequence of T_1 measurements, cf. Fig. D.2.

```

1 <Cluster>
2 <Name>Channel1Timing</Name>
3 <NumElts>3</NumElts>
4 <Array>
5 <Name>Time (s) Channel 1</Name>
6 <Dimsize>4</Dimsize>
7 <DBL>
8 <Name>Wait</Name>
9 <Val>5e-06</Val>
10 </DBL>
11 <DBL>
12 <Name>Wait</Name>
13 <Val>2e-07</Val>
14 </DBL>
15 <DBL>
16 <Name>Wait</Name>
17 <Val>3e-06</Val>
18 </DBL>
19 <DBL>
20 <Name>Wait</Name>
21 <Val>0.000192</Val>
22 </DBL>
23 </Array>
24 <Array>
25 <Name>PulseArray</Name>
26 <Dimsize>4</Dimsize>
27 <U16>
28 <Name>Ring</Name>
29 <Val>14</Val>
30 </U16>
31 <U16>
32 <Name>Ring</Name>
33 <Val>111</Val>
34 </U16>
35 <U16>
36 <Name>Ring</Name>
37 <Val>8</Val>
38 </U16>
39 <U16>
40 <Name>Ring</Name>
41 <Val>0</Val>
42 </U16>
43 </Array>
44 <DBL>
45 <Name>Number of Scans</Name>
46 <Val>1</Val>
47 </DBL>
48 </Cluster>

```

Listing D.2: Sample *XML* file for a single pulse including an acquisition window (delays according to the *field detection* part in Fig. D.2 and Lis. D.1).

APPENDIX E

Source code for pulsed field analysis

```
1 from numpy import *
2
3 def fcFT(parameters, x,y):
4     """ function to calculate the FT with time-dependent base functions according to B(t)
5
6     parameters are
7         flo                spectrometer frequency
8         gamma              gamma or frequency at max field of the fit reference
9         gammaStart, gammaStop  range for calculation
10        nb                  number of frequency values
11        a, b, c, d          fit constants for B(t)
12    """
13
14    [flo, gamma, gammaStart, gammaStop, a, b, c, d, nb] = parameters
15    dwellTime = x[1] - x[0]
16
17    # define frequency values for calculation
18    gammaRange = linspace(gammaStart, gammaStop, nb)
19
20    # filter only values within the excitation bandwidth
21    t = x[0]
22    B0 = (flo * 2 * pi + (a + 2 * b * t ** 1 + 3 * c * t ** 2 + 4 * d * t ** 3)) / gamma
23    mi = 2 * pi * (flo + dic['ExFilterRange'][0]) / B0
24    ma = 2 * pi * (flo + dic['ExFilterRange'][1]) / B0
25    gammaR = array(filter(lambda x: x >= mi and x <= ma, ))
26
27    # calculate the spectral coefficients
28    yr = []
```

```

29 B=[(flo*2*pi+(a+2*b*t**1+3*c*t**2+4*d*t**3))/gamma for t in x] # B(t)
30 for i in gammaR1:
31     t=0
32     phase=0
33     for j in xrange(len(y)):
34         t+=y[j]*exp(-1j*phase)
35         phase+=(i*B[j]-flo*2*pi)*dwellTime
36         yr.append(t)
37
38 # return gamma values/frequencies and spectral coefficients
39 return gammaR1,array(yr)

```

Listing E.1: Source code for Fourier transform with time-dependent base functions (Python).

```

1 from numpy import *
2
3 def t1Fit(params, x, y, offsets):
4     """ fit model for T1 relaxation in a pulsed magnetic field
5
6     params contains fit variables as well as constants describing the experiment
7
8     x are times of RF pulses
9
10    y are observed intensities
11
12    offsets are frequency offsets during excitation
13    """
14
15    Mstart = params['Mstart'].value
16    Meq = params['Meq'].value
17    T1 = params['T1'].value
18
19    # Brf can be kept constant or not
20    Brf = params['Brf'].value
21
22    """ constants """
23    gamma=params['gamma'].value
24    tau=params['tau'].value
25    Q=params['Q'].value
26    fcenter=params['fcenter'].value
27

```

```

28 results=[]
29 lastTime=0
30 Mz=Mstart
31
32 for t, offset in zip(x, offsets):
33     # the last RF pulse was at t=lastTime, giving a relaxation time of dt:
34     dt=t-lastTime
35
36     # the relaxation process changes Mz:
37     Mz=Meq-(Meq-Mz)*exp(-dt/T1)
38
39     # the effective RF field:
40     Beff=sqrt(Brf**2+(2*pi*offset/gamma)**2)
41
42     # calculation of the angles for the rotations
43     beta=-1*gamma*Beff*tau
44     theta=arctan2(Brf,2*pi*offset/gamma)
45
46     # after pulse magnetization values:
47     mx=sin(beta)*sin(theta)
48     my=(1-cos(beta))*sin(theta)*cos(theta)
49     mz=cos(theta)**2+cos(beta)*sin(theta)**2
50
51     # calculate factor to compensate for the resonator
52     omega0=2*pi*fcenter
53     omega=2*pi*(fcenter+offset)
54     epsilon=(omega0**2-omega**2)/(omega*omega0)
55     g=omega0/omega/(sqrt(Q**2*epsilon**2+1))
56
57     # store value representing the signal intensity
58     results.append(g*Mz*sqrt(mx**2+my**2))
59
60     # set after pulse values for next iteration
61     Mz=Mz*mz
62     lastTime=t
63
64     # we need an array with the difference of model and data
65     return array(results)-y

```

Listing E.2: Source code for T_1 fit in a pulsed magnetic field (*Python*).

```

1 import numpy as np

```

```
2 from lmfit import minimize, Parameters, Parameter, report_fit
3
4 # create a set of parameters according to the experiment
5 params = Parameters()
6 params.add('Mstart',value=-1.0)
7 params.add('Meq',value=1.0)
8 params.add('T1', value=.6e-3)
9
10 # Brf is set to constant
11 params.add('Brf', value=6e-3,vary=False)
12
13 # constants
14 params.add('tau', value=100e-9,vary=False)
15 params.add('gamma', value=6.97e7,vary=False)
16 params.add('Q', value=13.5,vary=False)
17 params.add('fcenter', value=322.3e6,vary=False)
18
19 # do fit, here with leastsq model
20 result = minimize(t1Fit, params, args=(t, y,off))
21
22 # write report
23 report_fit(result.params)
```

Listing E.3: Usage of the fit function from Lis. E.2.

Acknowledgments

The endeavors presented in this work were only made possible by a number of people.

Most importantly, the help, guidance, and critical discussions with Jürgen Haase were essential and helped to shape the ideas that were shown for which I am deeply grateful.

Furthermore, I am thankful to Michael Jurkutat for proofreading this manuscript and providing valuable insights in discussions.

I would also like to thank Benno Meier who introduced NMR experiments to me and, later, the *art* of NMR in a pulsed magnetic field.

The experiments at the HZDR would not have been possible without the support of the local staff for which I am grateful. Here, I would especially like to thank Elizabeth L. Green and Hannes Kühne.

Steven Reichardt helped with the experiments presented in Ch. 5 and the subsequent publication. Regarding the work on $\text{HgBa}_2\text{CuO}_{4+\delta}$, I would like to extend my gratitude to Damian Rybicki.

Furthermore, discussions on fundamental NMR topics with Boris V. Fine and Chahan M. Kropf were always helpful.

In addition to the previously mentioned M. Jurkutat and S. Reichardt, I would also like to thank Nataliya M. Georgieva, Matthias Mendt and Elisabeth Vonhof for providing an enjoyable atmosphere at work.

I am deeply grateful to Norma and Alexander, you are my home. Ulla und Reinhold, you provided invaluable help to us three.

This work was supported by the Free State of Saxony and the Deutsche Forschungsgemeinschaft within the Graduate School BuildMoNa as well as by the European Social Fund (ESF).

